

**Quantitative and Mechanistic Studies on the Spindle Assembly Checkpoint in
Human Cells Reveal the Origin of Its Sensitivity**

by

Chu Chen

A dissertation submitted in partial fulfillment
of the requirements for the degree of
Doctor of Philosophy
(Biophysics)
in the University of Michigan
2022

Doctoral Committee:

Professor Ajit P. Joglekar, Chair
Professor Julie S. Biteen
Assistant Professor Aaron T. Frank
Professor David K. Lubensky
Professor Yukiko Yamashita, Whitehead Institute
Assistant Professor Qiong Yang

Chu Chen
chenchu@umich.edu
ORCID iD: 0000-0002-5075-5722

© Chu Chen 2022

DEDICATION

I would like to dedicate this work to my grandparents. I was not able to stay by their side during their last days because I have been studying far away from my hometown since 2011. They were always caring about me and had a tremendous impact on me and the path that I chose. May they rest in peace.

ACKNOWLEDGMENTS

I would like to express my deepest gratitude to my advisor, Dr. Ajit Joglekar. Pursuing a Ph.D. degree is arduous, especially for me as an international student during a challenging time. Ajit has always been supporting me in many aspects.

I am grateful to all members of my thesis committee, who have kindly offered their time and expertise to give me guidance, suggestions, and comments on my research for nearly six years.

I would like to acknowledge all of my lab colleagues (Dr. Arti Dumbrepatil, Martin Fernandez, Frank Ferrari, Adrienne Fontan, Simon Han, Lauren Humphrey-Stark, Soubhagyalaxmi Jema, Shriya Karmarkar, Sisira Kavuri, Dr. Alex Kukreja, Andrew Livingston, Sean McGuire, Anna Olson, Juan Orozco, Rebekah Ronan, Dr. Babhrubahan Roy, Janice Sim, Dr. Vikash Verma, and Alex Vita) who have supported my work in the lab by directly participating in my research (which is credited in corresponding parts of the main text of this thesis), offering valuable suggestions, and building up a healthy work environment.

Our collaborators have taught me a lot about science and have greatly enhanced the breadth and impact of our research. They include (but are not limited to): Dr. Iain Cheeseman (Whitehead Institute); Dr. John Tyson and Dr. Anand Banerjee (Virginia Tech); Dr. Geert Kops (Hubrecht Institute, Netherlands); Dr. Song-Tao Liu and Dr. Yibo Luo (University of Toledo); Dr. Andrea Musacchio and Dr. Valentina Piano (MPI of Molecular Physiology, Germany).

Many other friends and colleagues have helped me greatly in this endeavor, either by directly solving my technical problems or offering key suggestions over the years. They include (but are not limited to): Dr. Mara Duncan (experimental techniques); Dr. J. Damon Hoff (fluorescence spectroscopy and associated data analysis); Dr. Dawei Yang (image processing and pattern recognition); Dr. Uhn-Soo Cho as well as Dr. Sojin An and Dr. Jennifer Chik (molecular cloning and protein purification); Dr. Diane Fingar and Dr. Dubek Kazyken (kinase assay); Dr. Fengrong Wang and Dr. Takamasa Inoue (immunoprecipitation); Dr. Chengxin Zhang (structure prediction); Dr. Xiangtian Tan (bioinformatics); Dr. Nigel Michki and Dr.

Kyoung Jo (fluorescence imaging); Dr. Zhejian Ji (spindle assembly checkpoint). Many others provided me with necessary reagents and instruments, whose assistance was or will be acknowledged in my published paper [1] and other manuscripts submitted to peer-reviewed journals [2, 3] or in preparation.

I would like to thank my mentors during my first-year rotations (Dr. Tom Kerppola and Dr. Wei Cheng). Although I did not join their labs, I am thankful for their close guidance at the early stage of my academic pursuit.

Last but not least, I could not have reached so far without the support and inspiration from my family and friends. They are my pole star and lighthouses in this memorable voyage.

TABLE OF CONTENTS

DEDICATION	ii
ACKNOWLEDGMENTS	iii
LIST OF FIGURES	viii
LIST OF ACRONYMS	x
ABSTRACT	xii
CHAPTER	
1 Introduction	1
1.1 Spindle, kinetochore, and kinetochore-microtubule attachment	2
1.2 The spindle assembly checkpoint (SAC) signaling pathway in human cells .	3
1.3 The sensitivity and responsiveness of the SAC	5
1.4 Cooperativity is one way to realize ultrasensitivity	6
1.5 Studying the SAC quantitatively <i>in vivo</i> : complications, challenges, and methodology	9
2 Ectopic Activation of the Spindle Assembly Checkpoint (SAC) Reveals Its Dose-Response Characteristics	11
2.1 Engineering an ectopic SAC (eSAC) activator	12
2.2 The eSAC activator can activate the SAC by hijacking the endogenous signaling pathway	14
2.3 Building a semi-automatic image analysis pipeline to enable the processing of large data sets from mitotic duration assays	16
2.4 The number of MELT motifs on the KNL1 signaling scaffold has a major impact on the SAC activity	17
2.5 The distance between MELT motifs has a minor impact on the SAC activity	22

2.6	The dose-response data suggest that cooperativity among multiple MELT motifs on a KNL1 phosphodomain boosts the SAC signaling activity	23
2.7	Discussion	25
2.8	Materials and methods	26
2.8.1	Purification of the recombinant MPS1 kinase domain	26
2.8.2	Purification of the recombinant KNL1 phosphodomain	28
2.8.3	<i>In vitro</i> kinase assay	29
2.8.4	Cell culture and Cre- <i>lox</i> recombination-mediated cassette exchange (RMCE)	29
2.8.5	Live-cell imaging on the IncuCyte® ZOOM system	30
3	Enrichment of SAC Proteins at Kinetochores Strengthens the SAC Signaling Activity	31
3.1	Using CRISPR-Cas9-mediated genome editing to tag SAC genes with mNeonGreen <i>in situ</i>	31
3.2	The recruitment of BUB1 to signaling kinetochores had a major depletion effect on the cytosolic pool of BUB1	37
3.3	The numbers of BUBR1, BUB1, and MAD1 recruited per signaling kinetochore are inversely correlated with the total number of signaling kinetochores in the cell	38
3.4	The equilibrium between the activity of MPS1 and counteracting phosphatases at signaling kinetochore is the same in nocodazole- and GSK923295-treated HeLa-A12 cells	41
3.5	Recruitment of BUBR1 by BUB1 <i>per se</i> contributes to the activity of the kinetochore-based SAC signaling	44
3.6	Discussion	46
3.7	Materials and methods	50
3.7.1	CRISPR-Cas9-mediated genome editing	50
3.7.2	Genotyping	50
3.7.3	Rapid amplification of cDNA ends (RACE)	51
3.7.4	Fluorescence correlation spectroscopy (FCS)	51
3.7.5	RNA interference (RNAi)	52
3.7.6	Live-cell imaging	53
3.7.7	Quantification of the FRET efficiency by kinetochore-localized fluorescence signals of MPS1sen-KT	54
3.7.8	Immunoblotting	56

4 The Structural Flexibility of MAD1 Facilitates the Assembly of the Mitotic Checkpoint Complex (MCC)	58
4.1 The molecular mechanism of the formation of CDC20-MAD2: the “assembly line” model <i>versus</i> the “knitting” model	59
4.2 The MAD1-MAD2 heterotetramer may adopt a fold-back conformation both <i>in vivo</i> and <i>in vitro</i>	63
4.3 MAD1’s loop region is important to the SAC signaling activity <i>in vivo</i>	68
4.4 MAD1(Lmut) can fully support the SAC signaling activity	69
4.5 The structural flexibility of MAD1 enabled by its loop region facilitates the “knitting” of the MCC	72
4.6 Discussion	75
4.7 Materials and methods	77
4.7.1 Calculating the theoretical end-to-end root-mean-square distance of a flexible unstructured peptide	77
4.7.2 Generating the <i>MAD2</i> ΔmScarlet-I genome-edited HeLa-A12 cell line .	78
4.7.3 RNAi	79
4.7.4 Fluorescence lifetime imaging microscopy (FLIM)	79
4.7.5 Immunoprecipitation using mNeonGreen-Trap	81
4.7.6 Immunoblotting	82
5 Conclusion and Perspective	83
BIBLIOGRAPHY	86

LIST OF FIGURES

FIGURE

1.1	The gradual establishment of kinetochore-spindle microtubule attachment and the role of the spindle assembly checkpoint (SAC) in ensuring equal chromosome segregation.	2
1.2	The biochemical interactions and reactions of the core SAC signaling pathway.	4
1.3	Many mechanisms may realize the sensitivity of a signaling pathway to a modest input.	7
1.4	Recruitment of BUBR1, a SAC protein, at nocodazole-induced signaling kinetochores and the release of BUBR1 from kinetochores at the deactivation of the SAC before the anaphase onset.	8
2.1	The design of an ectopic SAC (eSAC) activator and its stable integration into a defined genomic locus in HeLa-A12 cells.	13
2.2	The purified recombinant MPS1 kinase domain can phosphorylate the purified recombinant KNL1 phosphodomain in an <i>in vitro</i> kinase assay.	15
2.3	The semi-automatic data analysis pipeline for mitotic duration assays.	18
2.4	The observer bias in the data analysis of the mitotic duration assay can be eliminated by extending the duration of the time-lapse imaging and setting a cut-off line to filter out cells whose NEBD timing is too late.	19
2.5	A summary of the dose-response curves for the five eSAC activators with recombinant phosphodomains containing one to six MELT motifs.	20
2.6	Pairwise distances between (+1, +2, +3)-neighboring MELT motifs in human KNL1 and the M6 (M3-M3) eSAC construct.	22
2.7	The distance between MELT motifs has a minor impact on the SAC activity. .	24
3.1	Utilizing CRISPR-Cas9-mediated genome editing to fuse mNeonGreen to <i>BUBR1</i> , <i>BUB1</i> , and <i>MAD1</i> <i>in situ</i>	33
3.2	Genotyping PCR products (using the genome of the heterozygous mNG- <i>BUBR1</i> HeLa-A12 cell line as the template) feature hybrid double-stranded DNAs that are thermodynamically unfavorable.	35

3.3	5'-RACE identifies the 5'-UTR sequences of different <i>BUB1</i> alleles in the genome-edited mNG- <i>BUB1</i> cell line.	36
3.4	The numbers of BUBR1, BUB1, and MAD1 recruited per signaling kinetochore are inversely correlated with the total number of signalling kinetochores in the cell.	39
3.5	No difference in the MPS1-phosphatases equilibrium at signalling kinetochores was detected in HeLa A12 when cells were treated with different drugs at various concentrations.	42
3.6	Recruitment of BUBR1 by BUB1 to signalling kinetochores <i>per se</i> contributes to the SAC signalling activity.	47
4.1	The structure of the MAD1-MAD2 heterotetramer and the two models of the molecular mechanism of the formation of CDC20-MAD2.	61
4.2	The secondary structure of MAD1's loop region is well conserved.	62
4.3	Representative structures of the C-terminus of the MAD1 homodimer, the MAD1 Δ L homodimer, and the MAD1-MAD1 Δ L heterodimer were predicted by ColabFold.	65
4.4	The observation of FRET between MAD1-mNG and MAD2 \wedge mScarlet-I at the interphase/prophase NPC suggested that MAD1-MAD2 heterotetramers may assume a fold-back conformation <i>in vivo</i>	66
4.5	The loop region of MAD1 is critical to the SAC signalling activity in its own right.	70
4.6	MAD1(AL11)-mNG cannot fully rescue the SAC signalling activity but MAD1(Lmut)-mNG can.	73
4.7	"Knitting" model: MAD1's structural flexibility may facilitate the spatio-temporal coupling of MAD2's conformational switch and the assembly of the CDC20-MAD2 heterodimer.	74

LIST OF ACRONYMS

a.a. amino acid(s) (number)

ABBA A-type cyclins, BUBR1, BUB1, and Acm1

ANOVA analysis of variance

AU arbitrary unit

CD1 conserved domain 1 of BUB1, which is also named “conserved motif 1 (CM1)”

DMEM Dulbecco’s modified Eagle’s medium

eSAC activator ectopic spindle assembly checkpoint activator

FCS fluorescence correlation spectroscopy

FLIM fluorescence lifetime imaging microscopy

FRB* FRB with a T2098L point mutation

FRET Förster resonance energy transfer

gRNA guide RNA

HD heterodimerization domain (a.a. 432-484) of BUBR1

HD^{short} heterodimerization domain (a.a. 440-460) of BUBR1

HORMA Hop1p, Rev7p, and Mad2p

KARD kinetochore attachment regulatory domain of BUBR1

LUT lookup table

MCC mitotic checkpoint complex (consisting of CDC20, MAD2, BUBR1, and BUB3)

MELTⁿ the *n*-th consensus MELT motif among the 19 putative MELT motifs in human KNL1

MIM MAD2-interacting motif, which is also named “MAD2-binding motif (MBM)” or “closure motif”

mNG mNeonGreen

NEBD nuclear envelope breakdown

NPC nuclear pore complex

PBS phosphate-buffered saline

RACE rapid amplification of cDNA ends

RMCE recombination-mediated cassette exchange

RNAi RNA interference

RNP ribonucleoprotein

RT reverse transcription

RWD RING finger-containing proteins, WD repeat-containing proteins, and DEAD-like helicases

RZZS ROD-Zwilch-ZW10-Spindly

SAC spindle assembly checkpoint

SEM standard error of the mean

sgRNA single guide RNA

siRNA small interfering RNA duplex

TRE tetracycline-responsive promoter element

TSS transcription start site

UTR untranslated region

WT wildtype

ABSTRACT

Equal distribution of replicated genetic materials packed in chromosomes from a dividing parent cell to two daughter cells is the hallmark of mitosis. This task is carried out by the spindle, whose microtubules attach to chromosomes through adaptors named kinetochores. Failure to achieve faithful chromosome segregation is often associated with cancers and many pathological syndromes.

My thesis investigates a surveillance mechanism named the spindle assembly checkpoint (SAC) that safeguards faithful chromosome segregation. The SAC is activated at kinetochores lacking end-on spindle microtubule attachment to stall the progression of mitosis. The SAC can robustly arrest a mammalian cell in mitosis in the presence of either many unattached kinetochores or merely one. Although the biochemical events associated with the SAC have been mostly elucidated, how the SAC reaches such “sensitivity” to effectively arrest a cell in mitosis in the presence of a single unattached kinetochore remains unclear. Here, I will describe how multiple proteins and reactions cooperate at various layers to enable this sensitivity.

First, to study the origin of the sensitivity of the SAC, we need a quantitative readout of the input (the phosphorylation of the scaffold protein KNL1 which recruits SAC proteins and activates the SAC at signaling kinetochores) and the output (the duration of the mitotic arrest caused by the SAC). In Chapter 2, we engineer a cytosolic probe that ectopically activates the SAC, which solves the technical challenge to gauge the phosphorylation of KNL1 in live cells. Dose-response analyses using the probe reveal that under certain conditions, the SAC signaling activity is stronger with a smaller number of phosphorylated KNL1 proteins. This striking observation strongly indicates positive cooperativity in the SAC, which may underlie the sensitivity of the SAC.

Next, I validate some of the preconditions of this cooperativity model above in the context of the endogenous kinetochore-based SAC in Chapter 3. We demonstrate that the numbers of SAC proteins recruited per signaling kinetochore are inversely correlated with the total number of signaling kinetochores in the cell. Additionally, I show that the localization at signaling kinetochores of BUBR1, an important constituent of the mitotic checkpoint com-

plex (MCC, the effector molecule that stalls the progression of mitosis made up of BUBR1, BUB3, CDC20, and MAD2), strengthens the SAC activity. These observations reinforce the idea that cooperative signaling contributes to the sensitivity of the SAC.

Finally, in Chapter 4, I explore the catalytic mechanism of the rate-limiting step in the assembly of the MCC – the formation of CDC20-MAD2. Unveiling this catalytic mechanism is fundamental to understanding how an unattached kinetochore can produce an adequate signal to stall mitosis. Given that both CDC20 and MAD2 bind to the catalyst MAD1, I hypothesize that the structural flexibility of MAD1 helps to position CDC20 and MAD2 closely, thereby coordinating the formation of CDC20-MAD2. Our data show that disrupting the structural flexibility of MAD1 impairs the SAC signaling activity, based on which I propose a model for the catalytic mechanism of the formation of CDC20-MAD2 scaffolded by MAD1.

My thesis research reveals the role of cooperative synergy in shaping the sensitivity of the SAC. It also establishes the foundation for future studies aiming for a complete understanding of the origin of its sensitivity.

CHAPTER 1

Introduction

Somatic cell division generates two genetically identical daughter cells from a single parent cell. Among different stages of the cell cycle, my thesis focus on mitosis. Mitosis follows the conclusion of interphase (during which nuclear DNAs are duplicated) and can be further divided into prophase, prometaphase (after the nuclear envelop breakdown and before all chromosomes are aligned at the metaphase plate, which is the main stage which my thesis revolves around), metaphase, anaphase, and telophase [4].

To generate two genetically identical daughter cells, duplicated nuclear DNAs packed within chromosomes need to be distributed into the two daughter cells equally. This requires that each duplicated chromosome is stably attached to spindle microtubules emanating from the two opposite poles of the parent cell before the parent cell divides. The spindle assembly checkpoint (SAC) serves as a surveillance mechanism that monitors the completion of this process and prevents the premature onset of the anaphase, thereby avoiding chromosome missegregation [4].

The SAC can robustly delay the onset of the anaphase in the presence of a single chromosome with monopolar attachment [5]. The question I want to address through my thesis research is how the SAC achieves such sensitivity. Through my extensive studies, I discovered that the SAC exploits cooperative synergy at multiple layers of the signaling cascade to achieve such sensitivity. This chapter introduces some of the basic facts, important concepts, and motivations of my thesis research to prepare my dear readers for later chapters. In later chapters, necessary information related to the experiments, reasoning, and discussion will be mentioned again or cross-referenced to the corresponding sections here.

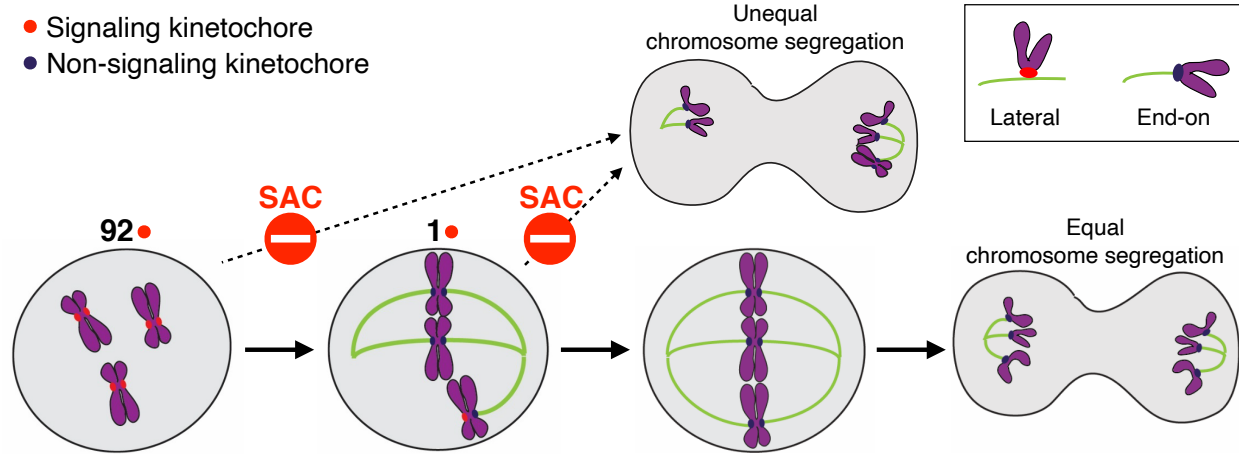


Figure 1.1: The gradual establishment of kinetochore-spindle microtubule attachment and the role of the spindle assembly checkpoint (SAC) in ensuring equal chromosome segregation.

In a canonical human somatic cell during mitosis, 46 chromosomes (with a total number of 92 chromatids and 92 kinetochores) gradually attach to the spindle during the prometaphase. Right after the nuclear envelop breakdown (NEBD) at the beginning of the prometaphase, all 92 kinetochores are not attached to microtubules. This number gradually decreases over the course of chromosome congression. Kinetochores without end-on microtubule attachment activate the SAC to prevent premature anaphase onset, ensuring equal distribution of chromosomes into daughter cells. Diagrams of the two modes of kinetochore-microtubule attachment (lateral vs end-on) are shown on the top right. It should be noted that lateral attachment is usually observed in the early stage of the establishment of kinetochore-microtubule attachment in the prometaphase, before sister chromatids separate from each other at the onset of the anaphase normally. The cartoon shows only one chromatid with one kinetochore in each case to simply demonstrate the concept.

1.1 Spindle, kinetochore, and kinetochore-microtubule attachment

To prepare for the equal distribution of duplicated nuclear DNAs packed within chromosomes, a mitotic cell forms the spindle (the green structure in Figure 1.1) whose microtubules attach to chromosomes from opposite poles of the cell. The adaptor structures on chromosomes which mediate such attachment are named kinetochores. After all chromosomes are bipolarly attached to the spindle and aligned at the metaphase plate (through a process named “chromosome congression” [6]), the cell will enter the anaphase when sister chromatids separate from each other. The spindle will then pull the two sets of chromosomes towards opposite poles of the cell, which later become parts of the two daughter cells [4].

In most vertebrates, kinetochores range between 0.1–0.5 µm in diameter [7]. The architecture

of human kinetochores is proposed to resemble a Velcro-like interface, forming adaptable attachment sites for an average number of about 17 microtubules in the metaphase [8, 9, 10, 11, 12]. There are two different modes of kinetochore-microtubule attachment in human cells: lateral attachment and end-on attachment (see Figure 1.1). The establishment of the kinetochore-microtubule attachment is a gradual and stochastic process [13].

Around a kinetochore in human cells, a crescent-shaped fibrous meshwork named the corona is assembled [14]. It is formed through the polymerization of the ROD-Zwilch-ZW10-Spindly (RZZS) complex [15, 16] and is stripped off the kinetochore by dynein at the establishment of microtubule attachment [17]. The corona expands the microtubule-attachment interface of a kinetochore and thereby facilitates the initial microtubule capture. The corona recruits the centromere-associated kinesin CENP-E, which promotes the conversion of lateral attachment into the desired end-on attachment [18, 19, 20]. The corona also recruits CENP-F which may contribute to the stability of the kinetochore-microtubule attachment and limits the dynein-mediated stripping of the corona [21].

1.2 The spindle assembly checkpoint (SAC) signaling pathway in human cells

Cells deploy the spindle assembly checkpoint (SAC) to monitor the progress of the establishment of the kinetochore-microtubule attachment during the prometaphase. The SAC is activated at kinetochores without end-on microtubule attachment to block premature anaphase onset [19, 22, 23]. This block allows time for the establishment of the end-on kinetochore-microtubule attachment. Once all attachment is secured, the SAC is silenced and the block is lifted [24]. Mitosis is then resumed, heading toward equal segregation of chromosomes into daughter cells (see Figure 1.1).

After the NEBD, the SAC in mammalian cells relies on the kinetochore-localized signaling scaffold KNL1 as well as the corona during the prometaphase [22, 23, 25]. We refer to them as the core pathway (which will be the main focus of my thesis; see Figure 1.2) and the corona pathway, respectively [1, 26].

The core SAC signaling pathway is scaffolded by KNL1 localized at all kinetochores. The human KNL1 possesses 19 consensus MELT motifs in its mostly disordered N-terminus and middle region [42], some of which are phosphorylated by the kinase MPS1 localized at signaling kinetochores [29, 30, 43, 44, 45]. These phosphorylated MELT motifs initiate the core SAC signaling pathway by recruiting SAC proteins like BUB3, BUB1, BUBR1,

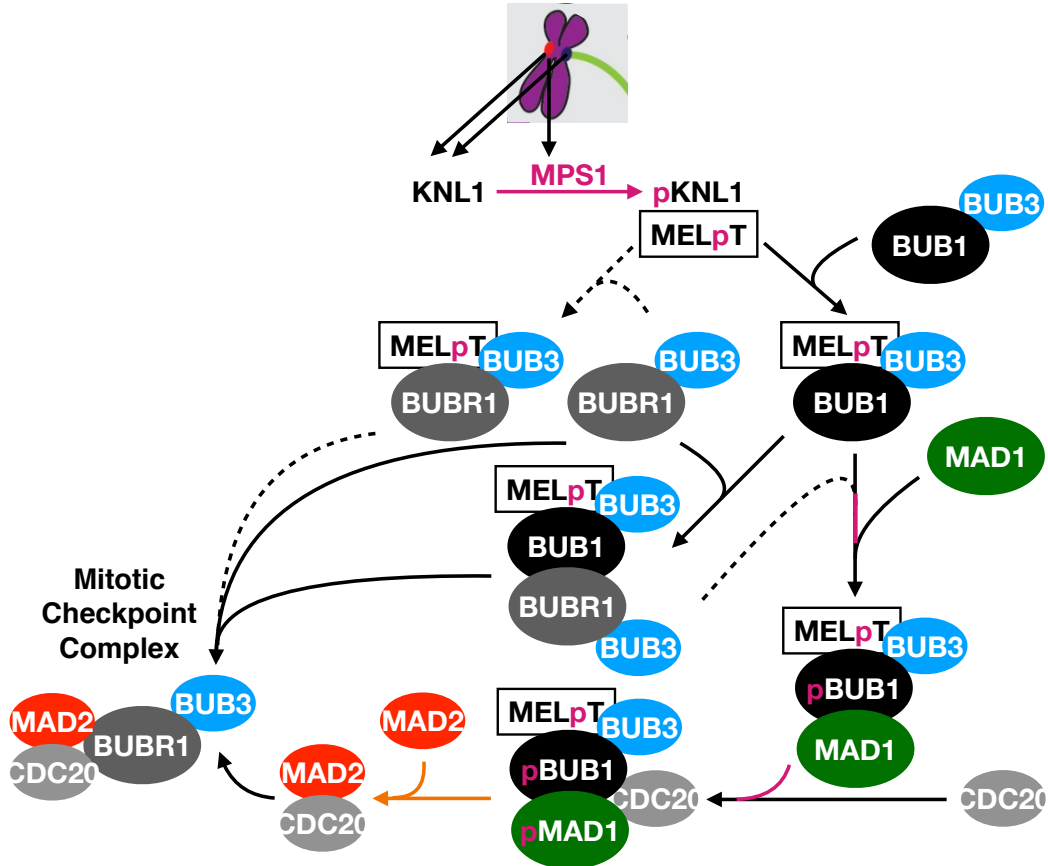


Figure 1.2: The biochemical interactions and reactions of the core SAC signaling pathway.

In the core SAC signaling pathway, signaling kinetochores recruit the kinase MPS1 which phosphorylates the consensus MELT motifs on the scaffold protein KNL1. Phosphorylated MELT motifs (the “MELpT” rectangle in the figure) will then recruit a series of SAC proteins and eventually generate the effector molecule known as the Mitotic Checkpoint Complex (MCC), which blocks the progression of mitosis. CDC20 binds to signaling kinetochores cooperatively via its interactions with BUB1 and MAD1 [27, 28]. Black solid arrows indicate direct binding or participation, which is either the consensus understanding in the field [27, 28, 29, 30, 31, 32, 33, 34, 35, 36] or experimentally proved in my thesis research (see Section 3.5). Black dashed arrows indicate arguable [33, 34] or hypothetical direct binding or participation (note that as to our knowledge, there has been no study which investigated whether a BUB1 protein can bind to both BUBR1 and MAD1 simultaneously or not and therefore, a dashed arrow connects MELpT-BUB1-BUBR1 and MELpT-BUB1-MAD1 here). Magenta arrows and texts indicate MPS1 or involvement of MPS1-mediated phosphorylation [37]. The orange arrow indicates catalytic reactions leading to the formation of the CDC20-MAD2 dimer, which will be the focus of Chapter 4. The green MAD1 oval indicates the MAD1-MAD2 heterotetramer (see Chapter 4). This heterotetramer is extremely stable in the budding yeast [38]. The molecular weight of MAD1 (an extended protein mainly composed of α -helices according to the prediction of AlphaFold 2 [39, 40]) is also much greater than the molecular weight of MAD2 (a globular protein [41]). Therefore, the MAD1-MAD2 heterotetramer is also sometimes simply referred to as “MAD1” in the following context.

CDC20, and the MAD1-MAD2 heterotetramer, thereby promoting the assembly of the mitotic checkpoint complex (MCC) consisting of BUBR1/BUBR1-BUB3 and CDC20-MAD2 [27, 28, 31, 32, 33, 34, 35, 36, 46] (see Figure 1.4). The mitotic checkpoint complex inhibits the E3 ubiquitin ligase anaphase-promoting complex/cyclosome (APC/C) [47, 48]. APC/C ubiquitinates Cyclin B1, a key mitosis regulator, thereby targeting it for proteasome-mediated degradation [49, 50, 51]. Through the inhibition of the APC/C, the degradation of Cyclin B1 is suppressed and the onset of anaphase is delayed.

In the corona pathway of the SAC, the corona recruits the MAD1-MAD2 heterotetramer to signaling kinetochores and promotes the SAC signaling activity [25]. It should be noted that the core pathway and the corona pathway are not independent in human cells. Corona constituents CENP-E and CENP-F interact with core SAC pathway components BUBR1 and BUB1, respectively [21, 52]. It has also been suggested that the recruitment of MAD1 to signaling kinetochores may be cooperative, facilitated by both the corona and BUB1 [53, 54]. We conceptually separate the two pathways because the corona does not exist in the budding yeast, while the core pathway is conserved from yeast to human [55].

The MCC is also assembled at the nuclear pore complex (NPC) during the interphase and prophase, where the MAD1-MAD2 heterotetramer is recruited by the nuclear basket protein TPR [56, 57]. Little is known about the regulations and mechanisms of the MCC assembly at the NPC, but it has been suggested to provide cells that newly enter the prometaphase with a starting pool of MCC and contribute to the robustness of the SAC.

1.3 The sensitivity and responsiveness of the SAC

The SAC signaling activity is positively correlated with the total number of signaling kinetochores [58, 59, 60]. However, even a single unattached kinetochore delays anaphase onset in a mammalian somatic cell line [5]. Although the biochemical interactions and reactions of the SAC signaling pathway have been mostly elucidated, how a single unattached kinetochore can delay anaphase onset has not been studied thoroughly. Understanding how the SAC achieves such sensitivity requires a quantitative and systematic examination of the SAC signaling pathway.

Signaling pathways may boost its sensitivity to a modest input by many mechanisms. Some signaling pathways amplify the input via biochemical reactions while some attain ultrasensitivity featuring a switch-like sigmoidal dose-response relationship (see Figure 1.3A). Due to the probable lack of amplification mechanisms in the SAC signaling pathway (see the

caption of Figure 1.3B for detailed explanations), my focus is to study whether and how the SAC realizes ultrasensitivity (see Section 1.4 for details).

After all chromosomes are attached to spindle microtubules, the SAC is deactivated and SAC proteins are stripped or released from signaling kinetochores (see Figure 1.4). The block inflicted on the progression of mitosis is lifted [17, 67, 70, 71, 72, 73, 74, 75]. A previous study has found that sister chromatids separate from each other in about half an hour after all chromosomes are attached to spindle microtubules in a mammalian cell line [58], demonstrating the responsiveness of the SAC. It is important to note (for the discussions in later chapters) that during normal mitosis, the prometaphase arrest is released without all kinetochores fulfilling their maximum microtubule-binding capacity. There is also a small amount of certain SAC proteins remaining at metaphase and anaphase kinetochores [76, 77].

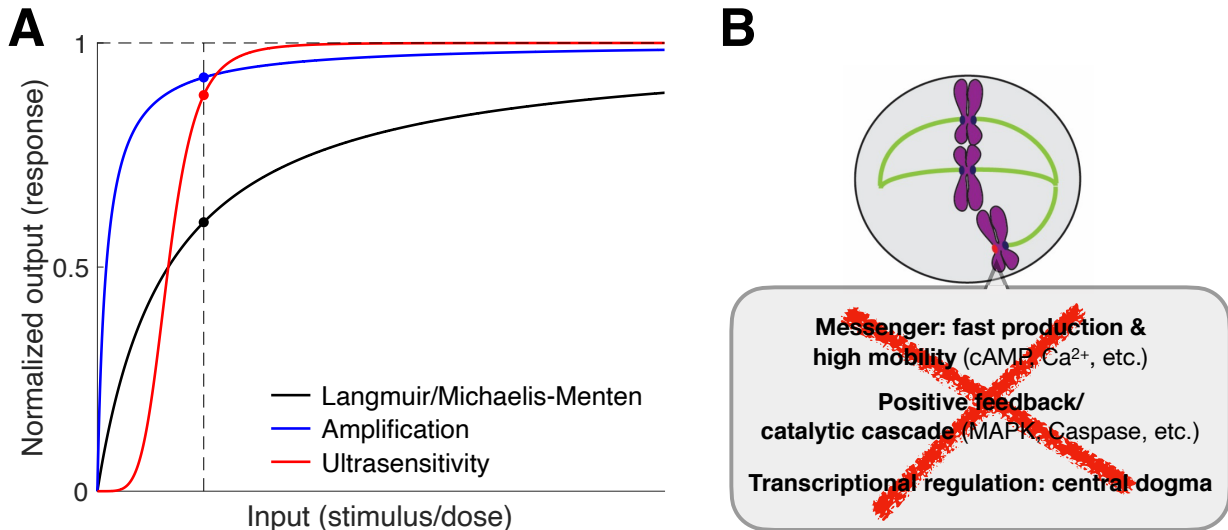
Although the responsiveness of the SAC is not the focus of my thesis, the sensitivity (that even a single unattached kinetochore can robustly delay the mitotic progression in mammalian cells) and responsiveness (that the mitotic progression is promptly resumed after all chromosomes are attached to spindle microtubules in mammalian cells) of the SAC are like two sides of the same coin [1]. Understanding the origin of the sensitivity and responsiveness of the SAC and their balancing (see Section 2.7) will help us better comprehend how the SAC activates to prevent premature anaphase onset in the presence of a decreasing number of signaling kinetochores and silences to initiate anaphase onset after all chromosomes are attached to spindle microtubules promptly during normal mitosis.

1.4 Cooperativity is one way to realize ultrasensitivity

The widely applicable Langmuir adsorption equation and Michaelis-Menten kinetics in biochemical interactions or reactions commonly inflict a dampening effect on any changes in the input [78]. To explain such dampening effect, suppose that the output $f(x) \geq 0$ is a monotonically increasing and strictly concave function of the input x for all $x \geq 0$ (like the Langmuir adsorption equation and Michaelis-Menten kinetics) and that the output is 0 if and only if the input is 0. Comparing the outputs [$f(x_2)$ and $f(x_1)$] corresponding to the inputs ($x_2 > x_1 > 0$), we have

$$1 < \frac{f(x_2)}{f(x_1)} = \frac{f(x_2)}{f[\frac{x_1}{x_2} \cdot x_2 + (1 - \frac{x_1}{x_2}) \cdot 0]} < \frac{f(x_2)}{\frac{x_1}{x_2} f(x_2) + (1 - \frac{x_1}{x_2}) f(0)} = \frac{x_2}{x_1},$$

which states that the contrast between the outputs is less than the contrast between the



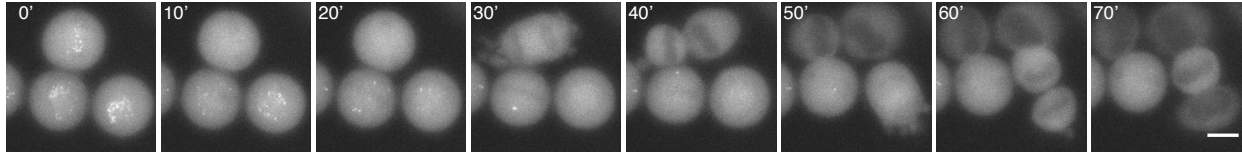


Figure 1.4: Recruitment of BUBR1, a SAC protein, at nocodazole-induced signaling kinetochores and the release of BUBR1 from kinetochores at the deactivation of the SAC before the anaphase onset.

Live genome-edited mNG-*BUBR1* cells (see Sections 3.1 and 3.7.1) were first arrested in mitosis by nocodazole (see Section 1.5), then released into drug-free FluoroBrite™ DMEM [Gibco; supplemented with 9% (by volume) of fetal bovine serum and 1× GlutaMAX] before the start of imaging (labeled as “0’”), and finally imaged on a wide-field Nikon Eclipse Ti-E/B inverted microscope equipped with a Nikon Plan Fluor 40×, 0.75 NA objective (see Section 3.7.6). The intermediate magnification selector knob was switched to 1.5×. Cells that were released from the nocodazole arrest resumed the progression of mitosis [12]. A montage of the maximum *z*-projection taken from the same field of view in the green fluorescence channel is shown here. The bright spots in the cell indicate the recruitment of mNG-BUBR1 onto signaling kinetochores. These spots disappeared over time before the anaphase onset because the SAC was silenced once the kinetochore established end-on attachment to spindle microtubules. Scale bar, 10 μm.

inputs [79].

There are many well-studied mechanisms deployed by signaling cascades to circumvent the dampening effect and sensitize the output [80, 81, 82]. For example, the multi-step/multi-site phosphorylation mechanism has been implied in the SAC by experimental evidence [37] (see the magenta arrows and texts in Figure 1.2). Such mechanism enables a sigmoidal dose-response relationship, which is named “ultrasensitivity” (red curve). The advantage of ultrasensitivity compared to simple signal amplification is that the signaling response is robust against a small noise (during the activation stage) or residue (during the deactivation stage) in the input (see Figure 1.3A). Such robustness may be exploited by the SAC to realize its responsiveness mentioned above.

Another way to realize ultrasensitivity is cooperativity. “Cooperativity” was originally used to describe the binding of oxygen molecules to the multi-subunit hemoglobin [83, 84]. Hereafter, I will use the term “positive cooperativity” (or simply “cooperativity”) to describe the cooperative synergy, which I attribute to the increased local concentration of SAC proteins due to their co-localization on the same signaling scaffold (see the descriptions of the proposed models in Sections 2.6 and 4.5). This is reminiscent of the theoretical explanation of the avidity between antibodies and antigens [85], a well-characterized example of cooperativity.

1.5 Studying the SAC quantitatively *in vivo*: complications, challenges, and methodology

Studying the SAC quantitatively *in vivo* is hindered by many intrinsic complications and technical challenges. First, as introduced in Section 1.2, the SAC signaling cascade is physically confined at kinetochores. There, the potential molecular crowding may slow down diffusion due to increased local viscosity, thereby reducing reaction rates; on the other hand, the potential increase of the effective concentration of reactants may increase reaction rates [86]. *In vitro* reconstitution of the SAC signaling cascade using purified proteins may not faithfully reflect the biophysical aspects of the kinetochore environment.

Second, the biochemical cascade of the SAC is regulated by many other kinases as well as phosphatases in human cells. Some of them are recruited by kinetochore proteins that are not an integral part of the core SAC pathway, while others directly bind to SAC proteins. For example, both PLK1 and Aurora B are important kinases that regulate mitosis. PLK1 directly binds to BUB1 and the kinetochore protein CENP-U [87], while Aurora B localizes predominantly to the inner centromere during the prometaphase [88]. Another example is that BUBR1 directly binds to PP2A-B56, a phosphatase that silences the SAC either directly [65, 66] or indirectly [67, 89, 90, 91, 92]. These interactions and regulations complicate the design of *in vivo* experiments and the interpretation of cell biology data (for example, see Section 3.5).

Third, as addressed in Section 1.2, the core pathway and the corona pathway of the SAC are not independent in human cells. Our understanding of the architecture of either the kinetochore or the corona is still far from complete. Dissecting the two pathways properly may be necessary to study the origin of the sensitivity of the SAC in human cells.

Fourth, to study the origin of the sensitivity of the SAC in human cells, we need to create the scenario wherein mitotic cells have a small number of signaling kinetochores. Very few studies have attempted it [58, 59, 60]. In some of these studies, the researchers either (1) treated cells with a low concentration of microtubule drugs and specifically looked for cells with a small number of signaling kinetochores, or (2) employed laser microsurgery to cut microtubules that attached to kinetochores. These strategies may not be robust or require specialized microscopy setups. More importantly, they do not provide enough data throughput to counter the stochastic nature of the establishment of the kinetochore-microtubule attachment [13].

Finally, over-expression of a SAC protein that is commonly observed in transgenic cells may deplete the cytosolic pool of the corresponding binding partner, thereby impairing the SAC

signaling activity [93, 94, 95, 96]. On the other hand, the SAC signaling activity maintains at a considerable level even when most BUB1 [54, 97, 98] or MAD1 (see Chapter 4) proteins are knocked down. These factors make it hard to execute a knockdown-rescue experiment.

We adopted or developed many experimental methods to circumvent the aforementioned complications and challenges. To dissect the role of the core SAC pathway without the complication of kinases recruited by kinetochore proteins or the corona pathway, we engineered an ectopic SAC (eSAC) activator consisting of a recombinant KNL1 phosphodomain and a recombinant MPS1 kinase domain (see Chapter 2 for details). The eSAC activator hijacks the endogenous SAC signaling pathway and can be easily quantified. Combined with a semi-automatic data analysis pipeline which I developed, this novel tool offers the capability to process large live-cell imaging data sets to reveal the dose-response characteristics of the core SAC signaling pathway.

To visualize and quantify the localization of SAC proteins at signaling kinetochores without disrupting the expression patterns of these SAC proteins, we utilized CRISPR-Cas9-mediated genome editing to tag SAC genes *in situ* [99]. This strategy may protect any endogenous transcriptional and translational regulations. The resulting genome-edited cell lines may also serve as a standard in filtering cells with induced expression of SAC proteins at various levels in a knockdown-rescue experiment (see Chapters 3 and 4 for details).

To study the correlations between the amount of SAC proteins localized to each signaling kinetochore and the total number of signaling kinetochores, we treated the cells with either GSK923295 or nocodazole (see Chapter 3 for details). GSK923295 inhibits the ATPase activity of CENP-E, thereby disrupting chromosome congression and yielding small numbers of chromosomes near spindle poles [100]. These polar chromosomes typically possess one kinetochore that is unattached or laterally attached to spindle microtubules and activates the SAC [19, 22, 23]. Nocodazole affects the dynamics of microtubules and distorts spindles in human cells [26, 101]. At the most commonly used concentration of 330 nM, nocodazole treatment turns on SAC signaling at almost all kinetochores. In general, the effect of nocodazole can range from creating a small number of unattached kinetochores at a low dosage (see [26, 60] or Section 3.5) to completely nullifying the formation of any microtubules at a high dosage (like 6.6 μ M used in Section 3.4).

CHAPTER 2

Ectopic Activation of the Spindle Assembly Checkpoint (SAC) Reveals Its Dose-Response Characteristics

Ideally, the SAC should be able to block the progression of mitosis in the presence of various numbers of unattached (or laterally attached) kinetochores in a dividing cell. And indeed, even a single unattached kinetochore delays anaphase onset in mitotic PtK1 cells [5]. However, previous studies have suggested that the SAC may be less stringent in the first few cleavages of mammalian zygotes, which could be one of the reasons that lead to embryonic aneuploidy [102, 103, 104]. To understand how the SAC responds to the changing number of signaling kinetochores in a cell over the course of chromosome congression (see Figure 1.1), it is necessary to define the dose-response characteristics of the SAC. Here, the input/dose is the number of signaling kinetochores in a cell and the output/response is the SAC signaling activity (usually quantified by the duration of the mitotic arrest induced by the SAC). As mentioned in Section 1.5, it is technically challenging to maintain a specific number of signaling kinetochores in the cells [60], especially when a large number of cells are required to account for the noise caused by many factors (*e.g.*, cell-to-cell variation in the expression of SAC proteins).

This chapter describes the development of a novel ectopic SAC (eSAC) activator, which activates the SAC independently of the status of kinetochore-microtubule attachment. By exploiting heterogeneous expression of the eSAC activator in a large population of cells, we defined the dependence of the eSAC activator-induced mitotic arrest on the abundance of the eSAC activator to reveal the dose-response characteristics of the core SAC signaling cascade. The revelation of the dose-response characteristics of the core SAC signaling cascade suggests that cooperative synergy may contribute to the sensitivity of the SAC. To our knowledge, this is the first piece of evidence supporting the role of cooperative synergy in the SAC.

This chapter is adapted from [1] with the addition of new references and some unpublished data. My lab colleagues (Dr. Pavithra Aravamudhan and Palak Sekhri) and my advisor Dr. Ajit Joglekar laid the foundation of this study (which is related to the US patent US10669320B2). Key experiments and data mentioned in this chapter to which I am not a contributor are referred back to the published paper and credited accordingly. Certain statements in the original discussion section have been adjusted, but the basic ideas and main conclusions stay the same as in the original paper.

2.1 Engineering an ectopic SAC (eSAC) activator

Because the core SAC signaling pathway is initiated by the phosphorylation of MELT motifs in KNL1 by MPS1 [43, 44, 45], it should be possible to bypass the involvement of kinetochores and activate SAC signaling by bringing MPS1 into close proximity with KNL1. Previous studies have shown that the SAC can be activated ectopically (independently of the status of kinetochore-microtubule attachment) by overexpressing the MPS1 homolog in the budding yeast [105], anchoring MAD1 to metaphase kinetochores in human cells [106], or dimerizing the KNL1 homolog with the MPS1 homolog in the budding yeast [107] or the fission yeast [108]. Inspired by these results, we engineered an ectopic SAC (eSAC) activator consisting of a recombinant KNL1 phosphodomain and a recombinant MPS1 kinase domain (Figure 2.1A). They are fused with the chemical-induced dimerization system, wherein FKBP and FRB bind to each other in a rapamycin-dependent manner with high specificity and affinity [109].

The kinetochore targeting of KNL1 is mainly mediated by its C-terminus [111, 112, 113, 114, 115] but may also be contributed by its N-terminus ([1], Figure S1A and S1B by Ian Whitney from Dr. Iain Cheeseman's group at Whitehead Institute). Therefore, we fused different truncations of the KNL1 phosphodomain (in the middle of KNL1) containing various numbers of MELT motifs with mNeonGreen (mNG, a bright monomeric yellow-green fluorescent protein [116]) and FKBP. The kinetochore targeting of human MPS1 is mainly mediated by its N-terminus [29, 30, 107]. Therefore, we fused the kinase domain of MPS1 with FRB* [117] and mCherry. The fluorescent protein tags in the two recombinant proteins constituting the eSAC activator enabled convenient quantification of the eSAC concentration in real time at a single-cell level using fluorescence imaging.

The expression cassettes of the eSAC activator pair were stably integrated into the genome via Cre-*lox* recombination-mediated cassette exchange (RMCE; Figure 2.1B) [106, 110], wherein the expression of the recombinant MPS1 kinase domain is under the regulation of the Tet-On system. Fluorescence imaging revealed that the KNL1 phosphodomain does

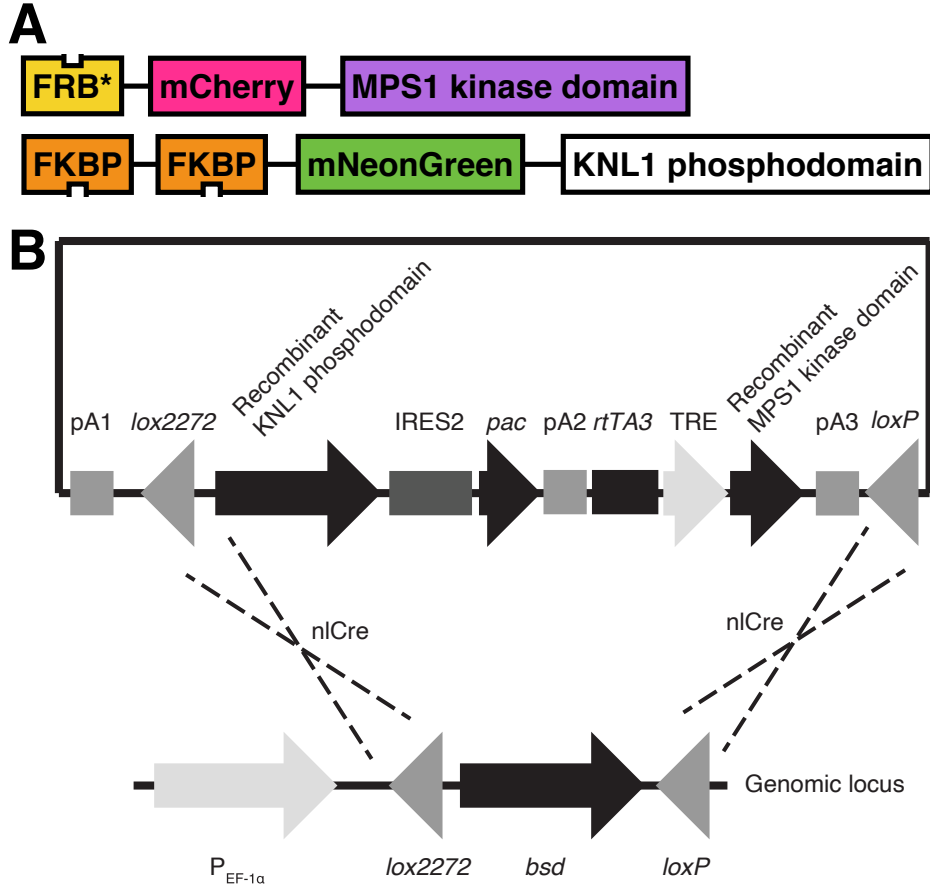


Figure 2.1: The design of an ectopic SAC (eSAC) activator and its stable integration into a defined genomic locus in HeLa-A12 cells.

(A) The eSAC activator consists of a recombinant KNL1 phosphodomain and a recombinant MPS1 kinase domain. The phosphodomain is at the N-terminus of the corresponding recombinant protein while the kinase domain is at the C-terminus of the corresponding recombinant protein. (B) A diagram demonstrating Cre-lox recombination-mediated cassette exchange (RMCE) between a transfected circular plasmid (the top part) and the genomic locus (the bottom part). This diagram is not to scale. The design was adapted from [106, 110]. pA1: the polyadenylation signal of herpes simplex virus thymidine kinase. IRES2: (encephalomyocarditis virus) internal ribosome entry site 2. *pac*: the coding sequence of puromycin *N*-acetyltransferase. pA2: the polyadenylation signal of bovine growth hormone. *rtTA3*: an expression cassette encoding the reverse tetracycline-controlled transactivator 3 (*rtTA3*), consisting of the promoter of the human ubiquitin C gene, the coding sequence of *rtTA3*, and a polyadenylation signal from simian virus 40. TRE: a tetracycline-responsive promoter element consisting of six tandem tetracycline operators followed by the minimal promoter sequence derived from the human cytomegalovirus immediate-early promoter. pA3: the polyadenylation signal of rabbit β -globin. nlCre: nucleus-localized Cre recombinase. $P_{EF-1\alpha}$: promoter of the human *EF1A* gene. *bsd*: the coding sequence of blasticidin S deaminase. After integrated into the genomic locus, the recombinant phosphodomain is under the regulation of the *EF1A* promoter while the recombinant kinase domain is under the regulation of the TRE.

not display perceptible kinetochore localization (see Figure S1A of [1]). We next set out to test whether the exogenously expressed eSAC activator can indeed hijack the endogenous SAC signaling pathway and arrest mitotic cells in the metaphase in a rapamycin-dependent, kinetochore-microtubule attachment-independent manner.

2.2 The eSAC activator can activate the SAC by hijacking the endogenous signaling pathway

As a proof of principle, we first tested (1) whether the recombinant MPS1 kinase domain can phosphorylate the recombinant KNL1 phosphodomain in the eSAC activator and (2) whether the phosphorylation reaction depends on rapamycin.

Using purified proteins, we showed that the purified recombinant MPS1 kinase domain can phosphorylate the purified recombinant KNL1 phosphodomain in an *in vitro* kinase assay (Figure 2.2). This reaction was strongly inhibited by reversine, an MPS1 inhibitor. The phosphorylation efficiency was higher when there was 500 nM rapamycin in the reaction, but even without rapamycin, phosphorylation was still detectable by a phospho-specific antibody [32]. However, phosphorylation of the recombinant phosphodomain was undetectable in eSAC-expressing HeLa-A12 cells without the addition of 500 nM rapamycin ([1], Figure 2B by Adrienne Fontan), maybe because the concentrations of the purified recombinant MPS1 kinase domain and the purified recombinant KNL1 phosphodomain in the *in vitro* assay were higher than their concentrations in the cells. The addition of 330 nM nocodazole also does not induce the phosphorylation of the recombinant KNL1 phosphodomain. Reciprocally, the MELT motifs in endogenous KNL1 were minimally phosphorylated when cells were treated with rapamycin. However, they were strongly phosphorylated in nocodazole-treated cells. Therefore, we concluded (1) that the recombinant MPS1 kinase domain phosphorylates the recombinant KNL1 phosphodomain in the presence of rapamycin and (2) that there is minimal crosstalk in the phosphorylation of the eSAC phosphodomain (by the recombinant MPS1 kinase domain) and the endogenous KNL1 (by the endogenous MPS1 localized at signaling kinetochores).

Rapamycin (but not the vehicle DMSO) treatment resulted in metaphase arrest in eSAC-expressing HeLa-A12 cells (Figure 2.5E; the duration of the mitosis from the NEBD to the anaphase onset or mitotic slippage is commonly used as an indicator of the SAC signaling activity [58, 59, 60]). Mutating MELT motifs (by mutating auxiliary TΩ sequences [31, 32] and rendering the consensus MELT sequences non-phosphorylatable) of the recombinant phos-

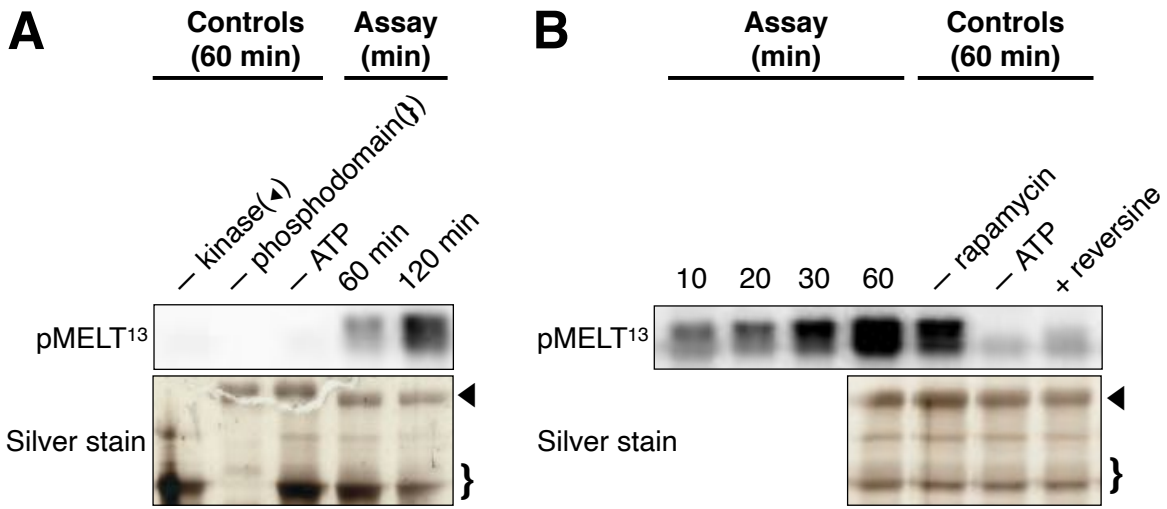


Figure 2.2: The purified recombinant MPS1 kinase domain can phosphorylate the purified recombinant KNL1 phosphodomain in an *in vitro* kinase assay.

(A) Phosphorylation of MELT¹³ was only detected when the kinase, the phosphodomain, and ATP co-existed in the reaction. (B) The phosphorylation reaction still happened even without the addition of 500 nM rapamycin, probably because the concentrations of the purified recombinant MPS1 kinase domain and the purified recombinant KNL1 phosphodomain in this *in vitro* assay were higher than their concentrations in eSAC-expressing HeLa-A12 cells induced by 2 µg/mL of doxycycline. The reaction was strongly inhibited by 1 µM reversine, an MPS1 inhibitor.

phodomain prevented the rapamycin-induced metaphase arrest ([1], Figure S2A by Dr. Ajit Joglekar). A mass spectrometry analysis on the recombinant phosphodomain pulled down from lysates of eSAC-expressing rapamycin-treated cells identified peptides from MPS1, BUB3, and BUB1, while the control group using eSAC-expressing cells arrested in mitosis by nocodazole could not ([1], Figure 2F by Ian Whitney).

Together, these results supported that the recombinant MPS1 kinase domain phosphorylated MELT motifs of the recombinant KNL1 phosphodomain in the presence of rapamycin, which then recruits SAC proteins (like BUB3 and BUB1) and delays anaphase onset in cells.

2.3 Building a semi-automatic image analysis pipeline to enable the processing of large data sets from mitotic duration assays

For mitotic duration assays requiring live-cell time-lapse imaging, I developed a semi-automatic pipeline [implemented in MATLAB (MathWorks)] to facilitate data analysis (Figure 2.3). Images of fluorescence channel(s) were first pre-processed to remove backgrounds and corrected for shading (due to spherical aberration of the objective, non-homogenous reflection of light at various interfaces or by the wall of the well, *etc.*). The background was obtained from a blank well containing only the imaging media. The shading pattern was calculated from a blank well containing the imaging media supplied with a purified fluorescence protein corresponding to the fluorescence channel (see Sections 2.8.1 and 2.8.2). We currently use the following equation to correct for the background and shading (on a pixel-by-pixel basis):

$$\text{Corrected fluorescence} = \frac{\text{Raw fluorescence} - \text{Background}}{\text{Normalized shading factor}},$$

wherein the normalized shading factor $\in (0, 1]$. Due to the lack of precise mechanical control of stage positioning on the IncuCyte® ZOOM system [but not so much on the ImageXpress® Nano Automated Imaging System (Molecular Devices) used in later chapters], there is non-negligible jittering over time. Images of the phase-contrast transmitted light channel were registered (aligned) with the preceding image in the stack recursively. The computed translations were then propagated to the calibrated fluorescence image stack(s).

Adherent mammalian cells typically (though not always [118]) assume a spherical shape

during the prometaphase, while interphase and prophase cells usually assume a flattened shape on a plate. In slightly defocused phase-contrast transmitted light images, these cells appear as circles defined by the halo artifact [119]. Our semi-automatic pipeline utilized this to detect mitotic cells by convolving each image with kernels representing “average” mitotic cells (constructed by 2-D averaging of micrographs of manually picked mitotic cells of the same cell line). A threshold is then applied to the correlation matrix to convert it into a binary matrix. Connected components of high-correlation pixels (above a certain threshold of the pixel size) are recognized as mitotic cells. Centroids of these connected components were linked across successive frames to connect all frames of the same cell across the entire history from the NEBD to the anaphase onset (hereby defined as an “event”). These events were then presented to the user in a graphical user interface, where the user can manually examine the field of view across all time points carefully to either abandon a false event or to correct the frame index of the NEBD/anaphase onset if necessary. The duration of mitosis is then calculated and corresponding (t, x, y) coordinates are propagated to the fluorescence channel(s) to measure the fluorescence signal(s) of the cell.

Depending on how long cells arrest in mitosis and how long the time-lapse imaging lasts, there will be an intrinsic observer bias of various degrees of severeness towards cells that only arrest in mitosis for a short duration (see Figure 2.4). In later chapters, this bias has mostly been eliminated because only cells that entered the prometaphase within 17 h after the start of the imaging session were analyzed (a time-lapse imaging session typically lasted for 36 h in experiments in later chapters on the ImageXpress® Nano Automated Imaging System and 23 h in this study on the IncuCyte® ZOOM system [1]).

2.4 The number of MELT motifs on the KNL1 signaling scaffold has a major impact on the SAC activity

The ability of the eSAC activator to hijack the endogenous SAC signaling pathway offered a novel tool to study the SAC quantitatively by correlating the cytosolic abundance of the eSAC activator with the mitotic duration from NEBD to anaphase onset (mitotic slippage) in a large population of cells. With this new molecular tool, we first explored how the number of MELT motifs in the phosphodomain of KNL1 affects the signaling activity of the SAC (Figure 2.5F). The idea has been explored in previous studies and came up naturally because there are 19 putative MELT motifs with various affinities to bind BUB1-BUB3 in human KNL1 [31, 32].

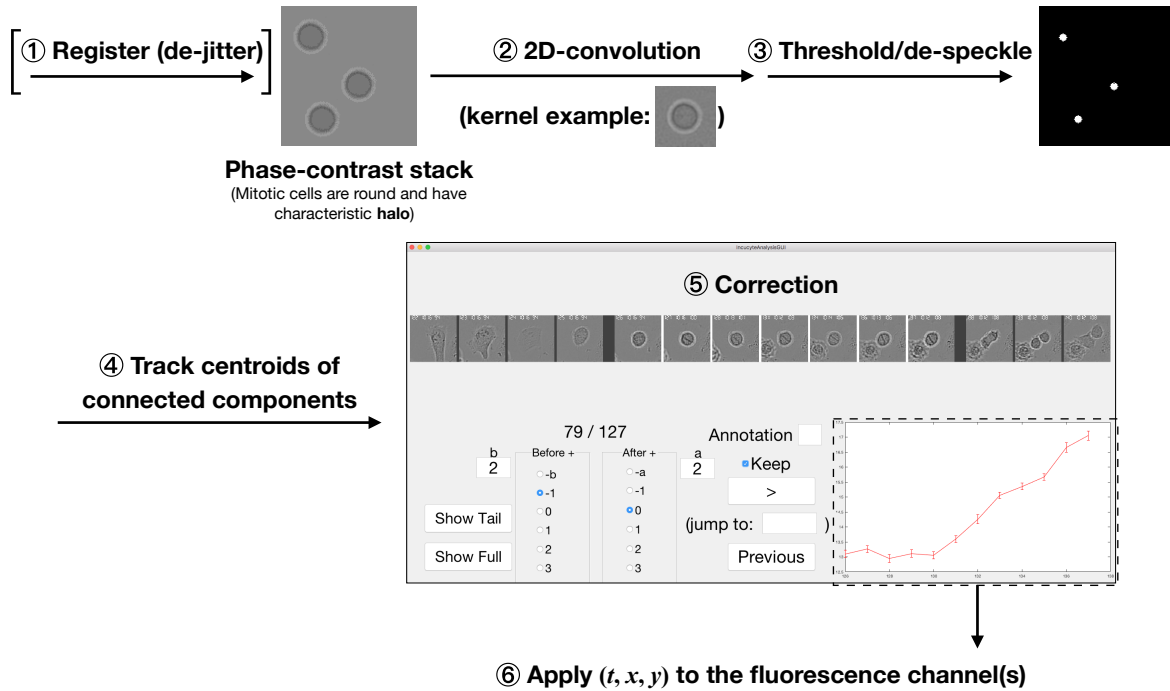


Figure 2.3: The semi-automatic data analysis pipeline for mitotic duration assays.

The phase-contrast image shown here is not a real image (but the exemplary kernel is one of the kernels that were used in this study). Real phase-contrast images are complicated by nearby or underlying interphase/prophase cells, dead cells that might also have a similar halo, and irregularity in the shape and size of the mitotic cells. Large displacement of a mitotic cell and local crowdedness may also be problematic to automatic tracking. Therefore, manual examination and correction of all identified mitotic events are necessary.

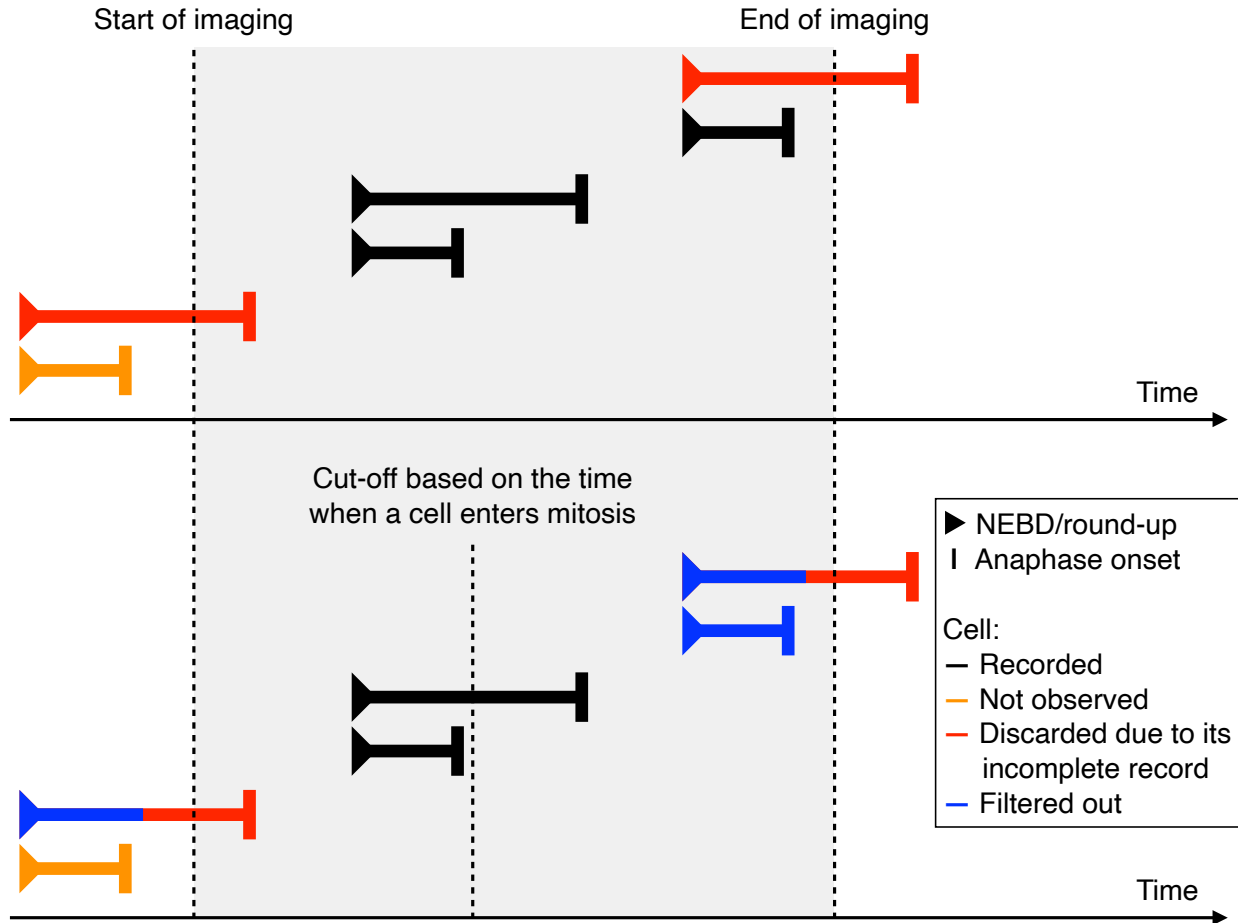


Figure 2.4: The observer bias in the data analysis of the mitotic duration assay can be eliminated by extending the duration of the time-lapse imaging and setting a cut-off line to filter out cells whose NEBD timing is too late.

In this simple example, we have two types of cells. One of them arrests in mitosis for a short duration while the other arrests in mitosis for longer. The ratio between the total numbers of the two types of cells is 1 : 1 and the NEBD timing is independent of the duration from the NEBD to the onset of anaphase. If no anti-bias measure is taken (as illustrated in the top panel), the observed ratio between the two will be distorted (2 : 1). However, if we set a cut-off line to filter out cells whose NEBD timing is too late (as illustrated in the bottom panel), the observed ratio will be restored to 1 : 1, faithful to the true ratio. As long as the margin from the cut-off line to the end of imaging is longer than the mitotic duration of most cells, this bias should be mostly eliminated.

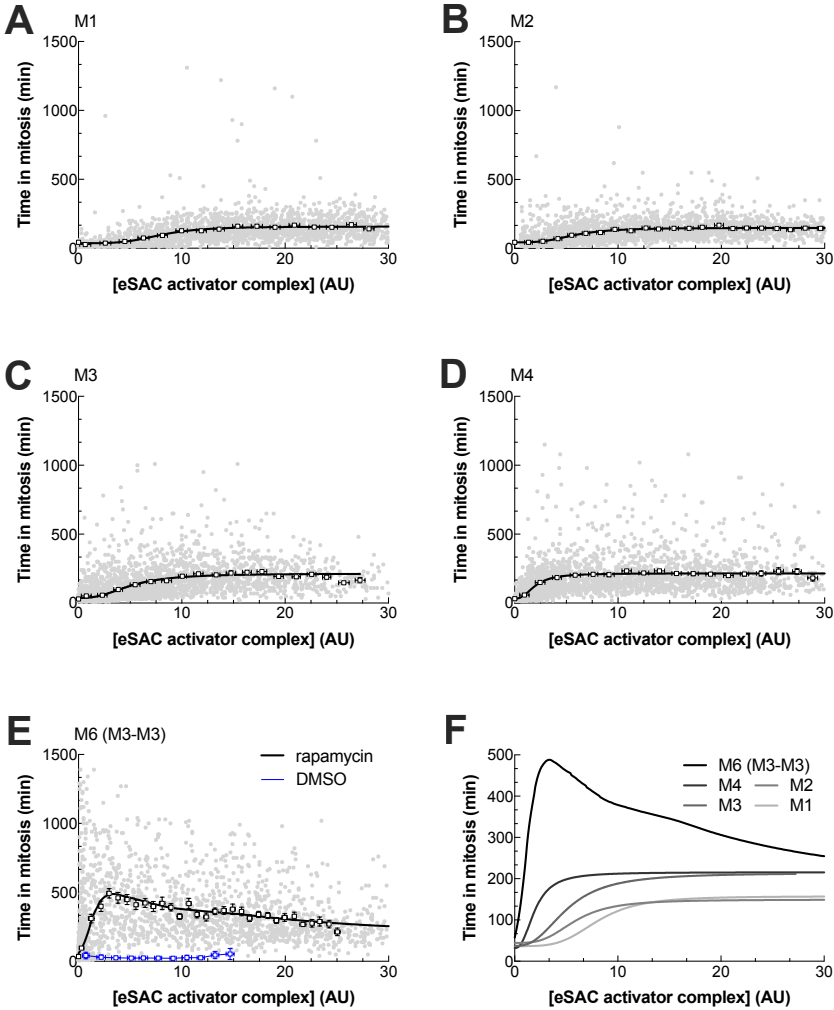


Figure 2.5: A summary of the dose-response curves for the five eSAC activators with recombinant phosphodomains containing one to six MELT motifs.

The dose (red fluorescence readout of the recombinant MPS1 kinase domain at the beginning of prometaphase in the cytosol of each cell) versus response (time in mitosis from the NEBD to the onset of the anaphase, which is simply referred to as “time in mitosis” in the following context) relationship for different eSAC activators [(A) M1, (B) M2, (C) M3, (D) M4, and (E) M6 (M3-M3)]. Each gray dot represents a cell. Data from at least two independent experiments were compiled with more than 2500 cells analyzed in each group. There may be some outliers beyond the range of the x - or y -axis (but they are included in the fitting). Bins of raw data (open squares, representing means \pm SEMs) are overlaid. (F) shows a summary of the fitted dose-response curves for the five eSAC activators with recombinant phosphodomains containing one to six MELT motifs. Data from M1, M2, M3, and M4 are fitted to a Hill equation (see the main text) while LOESS (locally estimated scatterplot smoothing) was applied to show the trend of M6 (M3-M3). This figure is compiled and adapted from Figures 3C, 3E, 3F, 3G, 4B, and 4C of [1]. Dr. Ajit Joglekar, Adrienne Fontan, and Lauren Humphrey-Stark also contributed to setting up the experiments and/or performing data analysis. AU: arbitrary unit.

We started out by incorporating a single MELT motif (MELT¹², which is henceforth referred to as “M1”, representing the minimal signaling unit of the core SAC signaling cascade) into the recombinant phosphodomain of the eSAC activator. We found that the duration of mitosis in the presence of 500 nM rapamycin depended on the cytosolic abundance of the eSAC activator (Figure 2.5A). We used a Hill equation to fit these data, which displayed a sigmoidal trend:

$$\text{Time in mitosis} = m + \frac{M}{1 + \left(\frac{K}{[\text{eSAC activator}]}\right)^n},$$

wherein n is the Hill coefficient and K is the level of the eSAC activator at which the time in mitosis reaches the middle between the baseline level (m) and the plateau level ($m + M$).

Similar sigmoidal trends were also observed in the dose-response relationship of eSAC activators with recombinant phosphodomains containing two (MELT¹²-MELT¹³, henceforth referred to as “M2”; Figure 2.5B), three (MELT¹²-MELT¹⁴, henceforth referred to as “M3” [31]; Figure 2.5C), or four (MELT¹¹-MELT¹⁴, henceforth referred to as “M4”; Figure 2.5D) MELT motifs. The maximal mitotic duration for eSAC activators with recombinant phosphodomains containing one or two MELT motifs was the same, but it was higher for eSAC activators with recombinant phosphodomains containing three or four MELT motifs. Given that the eSAC activator recruits SAC proteins to arrest cells in metaphase, limited cytosolic abundance of one (or some) of the SAC proteins likely restricts the maximal mitotic duration (a metric of the signaling activity of the SAC), leading to a plateau at high abundance of the eSAC activator. This layer of restriction is coupled with diverse rates of MCC assembly, leading to various plateau levels for different recombinant phosphodomains (see Sections 2.6 and 2.7). These results were consistent with a previous kinetochore-based study demonstrating that the KNL1 phosphodomain requires multiple MELT motifs to enable robust SAC signaling [31].

Surprisingly, the dose-response relationship of an eSAC activator with a recombinant phosphodomain containing six MELT motifs, which is made up of two tandem M3’s and henceforth referred to as “M6 (M3-M3)” [31], featured a non-monotonic curve (Figure 2.5E). This eSAC activator induced a strong mitotic arrest at a low concentration. As the abundance of the eSAC activator complex increased, the signaling activity of the SAC gradually decreased.

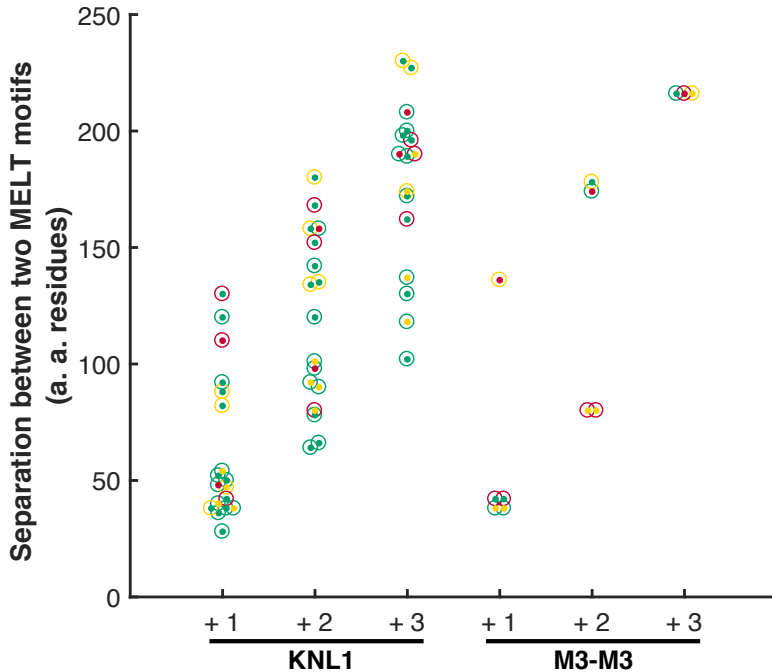


Figure 2.6: Pairwise distances between $(+1, +2, +3)$ -neighboring MELT motifs in human KNL1 and the M6 (M3-M3) eSAC construct.

Each “circle & center” symbol represents a pair of neighboring MELT motifs (with the circle representing one MELT motif and the center representing the other). There are a total number of 19 putative MELT motifs in human KNL1 and 6 MELT motifs in the signaling scaffold of the M6 (M3-M3) eSAC construct. Therefore, we have a total number of (18, 17, 16) pairs and (5, 4, 3) pairs of $(+1, +2, +3)$ -neighboring MELT motifs in human KNL1 and the signaling scaffold of the M6 (M3-M3) eSAC construct, respectively. The coloring scheme follows the one in Figure 1D of [32], which estimated the signaling activity of corresponding MELT motifs based on their capability to recruit BUB1 (green: “high”, yellow: “intermediate”, red: “low”). Distances in this chapter are measured between the threonine/serine residues of the consensus “MELT” sequences.

2.5 The distance between MELT motifs has a minor impact on the SAC activity

There are two major differences among the eSAC constructs in the previous section: (1) that the total numbers of MELT motifs in the signaling scaffold are different and (2) that the lengths of these signaling scaffolds are different. Even though the phosphodomain of KNL1 is largely unstructured and flexible [120], it remains to be seen whether the distance between MELT motifs affects the SAC activity. As a reference, the pair-wise distances between neighboring MELT motifs in the endogenous KNL1 are illustrated in Figure 2.6.

To study the effect of the distance between adjacent MELT motifs in the signaling scaffold on the SAC activity, we performed a series of experiments using eSAC activators with artificially designed signaling scaffolds [MELT¹²-1×linker-MELT¹², MELT¹²-2×linker-MELT¹², and MELT¹²-3×linker-MELT¹²]. The total number of MELT motifs is fixed at two and the sequence of MELT motifs adopts that of MELT¹². Various copies of the endogenous linker between MELT¹¹ and MELT¹² are inserted between the two MELT¹²'s. The resulting distance between the two MELT¹²'s varies from 135 to 311 amino acids (Figure 2.7), compared to a distance of 296 amino acids between the first motif and the last MELT motif in the M6 (M3-M3) construct in the previous section. We observed that MELT¹²-3×linker-MELT¹² has a slightly lower SAC activity compared to the other two, but the difference is small and negative (about -15 min to -10 min) compared to the differences in the SAC activities between M1 and M6 (M3-M3) [as well as between M3 and M6 (M3-M3)]. Therefore, we inferred that the difference in the number of MELT motifs in the eSAC constructs is the major factor that determines its SAC activity.

2.6 The dose-response data suggest that cooperativity among multiple MELT motifs on a KNL1 phospho-domain boosts the SAC signaling activity

We hypothesized that the increase in the maximum SAC signaling activity of the recombinant KNL1 phosphodomain with multiple MELT motifs was caused by cooperative signaling among them. This model enables eSAC activator to assemble MCC at a higher rate than what independent signaling of the MELT motifs may sum up to. In fact, if each individual MELT motif on a recombinant KNL1 phosphodomain generates the MCC independently, the dose-response relationship of an eSAC activator with a recombinant phosphodomain containing a larger number of MELT motifs will simply approach the same plateau level of SAC activity at a lower concentration of the eSAC activator. This reasoning is especially evident when we compare the dose-response relationship of M3 (Figure 2.5C) eSAC versus the dose-response relationship of M6 (M3-M3, Figure 2.5E) eSAC.

As the concentration of the eSAC activator increases, they compete with each other to recruit SAC proteins from their limited pools in the cytosol. Individual eSAC activators, even with multiple phosphorylated MELT motifs, may not be able to bind multiple SAC proteins concurrently. Thus, the synergistic SAC signaling dwindles. This model explains the decline in the dose-response relationship of the M6 (M3-M3) eSAC activator at high

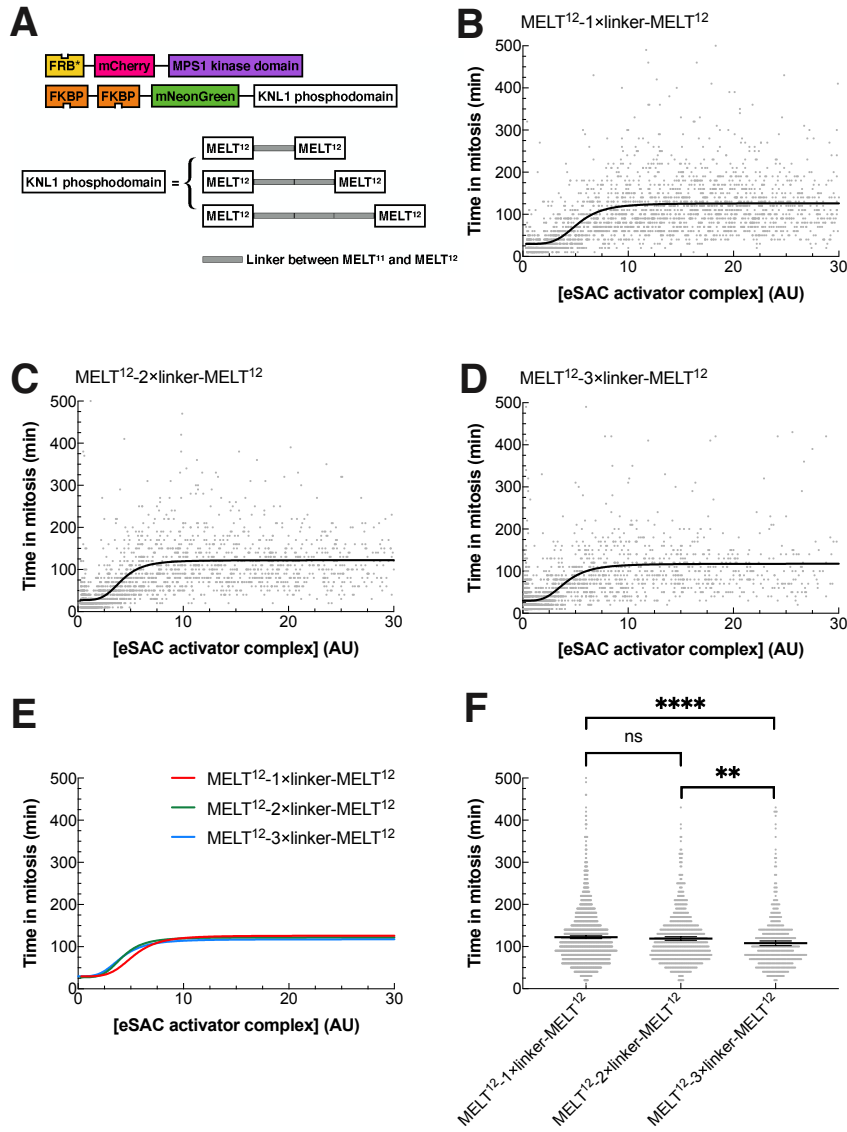


Figure 2.7: The distance between MELT motifs has a minor impact on the SAC activity.

(A) The distance between the two MELT¹² motifs in the three constructs are 135, 223, and 311 amino acids, respectively. The distance between the first motif and the last MELT motif in the M6 (M3-M3) construct in the previous section is 296 amino acids. (B-E) A summary (E) of eSAC activities of MELT¹²-1×linker-MELT¹² (B), MELT¹²-2×linker-MELT¹² (C), and MELT¹²-3×linker-MELT¹² (D) as the signaling scaffold. Each gray dot represents a cell. There may be some outliers beyond the range of the *x*- or *y*-axis (but they are included in the fitting). (F) Comparison of the plateau levels of SAC response curves of the three eSAC constructs. Only cells with [eSAC activator] > 10 AU are included. Data of more than 500 cells from two independent experiments were pooled for each group. The mean value \pm the 95% confidence interval of each group is overlaid. Unpaired *t*-tests with Welch's correction are performed in Prism 9 (GraphPad Software). Throughout my thesis, the following symbols for *p*-values are used: ns (not significant, $p \geq 0.05$), * ($0.01 \leq p < 0.05$), ** ($0.001 \leq p < 0.01$), *** ($0.0001 \leq p < 0.001$), and **** ($p < 0.0001$).

concentrations (Figure 2.5E), which is reminiscent of the hook effect in an agglutination test [121].

2.7 Discussion

As an analogous system, the cytosolic eSAC activator provides a convenient approach to study the design of the core SAC signaling cascade quantitatively in mammalian cells. Critical insights provided by dose-response data for eSAC activators with various recombinant phosphodomains shed light on how the core signaling cascade of the SAC may adapt the signaling activity of each kinetochore based on the total number of signaling kinetochores in the cell.

Although the maximal response from the SAC signaling cascade saturates, its magnitude is not the same for all eSAC systems. This magnitude may be partially influenced by the rate of MCC assembly of various MELT motifs (the actual sequence and ability to recruit BUB1-BUB3 of MELT¹¹, MELT¹², MELT¹³, and MELT¹⁴ deviate from each other). A study published more recently from our lab on the sequence specificity of MELT motifs in Spc105p (the homolog of human KNL1 in *Saccharomyces cerevisiae*) showed that replacing MELT motifs in Spc105p with those that bind to Bub1p-Bub3p with a higher affinity reduces the possibility of chromosome missegregation but also slows down the progression of the cell cycle in the budding yeast [122]. The evolution of MELT motif sequences may reflect a process of adjusting the balance between the accuracy of chromosome segregation and the propagation rate [42] (see previous discussion on the sensitivity and responsiveness of the SAC in Section 1.3).

Based on our dose-response data and mathematical modeling by our collaborators (Dr. Anand Banerjee from Dr. John Tyson's group at Virginia Tech), we proposed a model for the biochemical design of the SAC signaling cascade. When there are a large number of signaling kinetochores in the cell (for example, right after NEBD), they compete with each other in recruiting SAC proteins from their limited pools in the cytosol. This competition masks cooperativity and the SAC activity per signaling kinetochore is weak. However, because the number of signaling kinetochores is large, the SAC signaling activity is high. When there are a few or even a single signaling kinetochore in the cell (for example, at a later stage of the prometaphase), each signaling kinetochore or even each KNL1 at signaling kinetochores can now recruit a large number of SAC proteins at the same time and cooperativity enables remaining signaling kinetochores to assemble MCC at a high rate.

KNL1 from human and nematodes [113, 123] oligomerize, although the N-terminal hydrophobic region of KNL1 that mediates its oligomerization in *Caenorhabditis elegans* is not essential to the viability of embryos under normal conditions. It remains to be seen whether this further facilitates cooperative signaling and boosts the SAC signaling activity.

Alternative splicing is commonly observed in intrinsically disordered regions that mediate protein-protein interactions [124]. Strikingly, in many mammals, all MELT motifs are within a single exon, which is one of the longest internal exons (see Table 2.1). No alternatively splicing or insertion of an intron has been recorded for this region. The splicing machinery has to deploy specific mechanisms to correctly splice long exons [125]. However, the total number and the sequences of MELT motifs in KNL1 have undergone rapid diversification over the course of evolution [42]. Therefore, it may be worthwhile to employ mutational study using genome editing to investigate whether human cells are sensitive to the changes in the total number of MELT motifs, the sequences of MELT motifs, and the distances between MELT motifs in the endogenous KNL1.

We utilized the rapamycin-induced dimerization system to engineer our eSAC activator. However, endogenous MPS1 competes with microtubules to bind to the NDC80 complex, thereby gaining spatial proximity to KNL1 at kinetochores [29, 30]. The difference in the dynamics of MPS1 (in the eSAC activator with the addition of rapamycin *versus* at the kinetochores) may potentially lead to artifacts in the dose-response characteristics that are not physiologically relevant. Therefore, the model proposed here should be rigorously examined on the endogenous, kinetochore-based SAC. This is the motivation of the study in Chapter 3.

2.8 Materials and methods

2.8.1 Purification of the recombinant MPS1 kinase domain

The recombinant bacmid encoding $6 \times$ His-MBP-TEV-FRB*-mCherry-MPS1^{kinase domain} (124.8 kDa) was generated via Bac-to-Bac[®] (Thermo Fisher Scientific). Baculovirus-transfected Sf9 cells (from 1 L of culture) were pelleted down and stored at -80°C until protein purification. Cells were resuspended in buffer IA [50 mM Tris-HCl (pH 7.5), 300 mM NaCl, 0.2% Triton X-100, 20 mM imidazole, 0.1% β -mercaptoethanol, and supplemented with PMSF and cOmplete[™] EDTA-free Protease Inhibitor Cocktail (Roche) before usage] to a total volume of 60 mL. Cells were lysed by a Dounce homogenizer (20 strokes using the loose pestle followed by 1 stroke using the tight pestle) supplied with Benzonase[®] Nuclease (Sigma-Aldrich). Cell lysates were then centrifuged at 18,000 rpm, 4°C for 45 min in a

Table 2.1: The exon encoding all MELT motifs in KNL1 ranks among the top 0.03% by length among all curated internal exons in humans and mice.

All putative MELT motifs identified in [42] reside within a single exon and all recorded alternative splice variants of KNL1 contain this exon in listed mammals. Coordinates of exons (of mouse and human) in the CCDS database [126] were accessed on May 21, 2020. Exons from coding sequences with either a “Public” or a “Reviewed, update pending” status were pooled. Redundant entries were removed (because various coding sequences may share a common exon) and the ranking of the MELT motif-encompassing exon was calculated. Due to the lack of data for untranslated regions, only internal exons were included in the analysis. It should be noted that the maximum length of an exon is restricted by the length of the respective protein, and KNL1 is a long protein of 2342 amino acids (the canonical isoform). In a non-canonical isoform of human KNL1, this MELT motif-encompassing exon is 166 bases shorter but still includes all 19 putative MELT motifs.

Species	Exon length (bases)	Ranking among all curated internal exons
Human	5001	99.973%
Mouse	4497	99.975%
Rat	3439	N/A
Cattle	4020	N/A
Elephant	4023	N/A
Giant panda	4017	N/A
Dog	3837	N/A
Bonobo	3927	N/A

F21S-8x50y rotor. The supernatant was transferred and the pellet was discarded. 5 mL of Ni-NTA agarose (equilibrated with buffer IA; Thermo Fisher Scientific) was added into the supernatant and the mixture was rotated at 4 °C for 3.5 h. The slurry was then washed with 5 mL of buffer IA for 4 times. Bound proteins were eluted with buffer IB [50 mM Tris-HCl (pH 7.5), 300 mM NaCl, 0.2% Triton X-100, 200 mM imidazole, 0.1% β-mercaptoethanol].

2 mL of amylose resin was added (equilibrated with buffer IB; New England Biolabs) into eluted proteins from the Ni-NTA agarose column and the mixture was rotated at 4 °C for 2.5 h. The protein-bound amylose resin was then washed with 5 mL of buffer IC [50 mM Tris-HCl (pH 7.5), 300 mM NaCl, 0.2% Triton X-100] for 4 times. 2.5 mL of buffer IC followed by 40 µL of 1 M D-(+)-maltose stock solution was then added into the slurry. The mixture was rotated at 4 °C for 30 min and then eluted proteins were collected. The elution was loaded onto a Superdex 200 pg column (Cytiva) for size-exclusion chromatography. Fractions corresponding to the monomeric full-length 6×His-MBP-TEV-FRB*-mCherry-MPS1^{kinase domain} (determined by molecular weight estimation and SDS-PAGE analysis) were subject to a subsequent Bradford protein assay (Bio-Rad Laboratories) and later used in the *in vitro* kinase assay.

2.8.2 Purification of the recombinant KNL1 phosphodomain

Transformed Rosetta™ 2(DE3) cells were induced to express 6×His-3×FLAG-TEV-MELT¹²⁻¹⁴-mNeonGreen-2×FKBP (73.1 kDa) by 1 mM IPTG at 25 °C for 20 h. Cells from 2 L of Luria-Bertani liquid media were harvested, resuspended in deionized water into a total volume of 40 mL, and then stored at –80 °C until protein purification.

The cell slurry was thawed on ice and an equal volume of 2× buffer A [the 1× buffer A has the following composition: 50 mM Tris-HCl (pH 7.4), 500 mM NaCl, 0.1 mM EDTA, 0.1 mM EGTA, and 20 mM imidazole] supplemented with PMSF, 0.1 mg/mL chicken egg white lysozyme (Sigma-Aldrich), 2 mM DTT, and cOmplete™ EDTA-free Protease Inhibitor Cocktail was added into the slurry. Cells were lysed by sonication for a total amount of on time of 150 s at 62% amplitude (Model 500 sonic dismembrator, Thermo Fisher Scientific) in a water-ice bath at 0 °C. Triton X-100 was added to a final concentration of 0.5%. Lysates were rotated for 15 min and then centrifuged at 18,000 rpm, 4 °C for 45 min in a F21S-8x50y rotor. The supernatant was filtered through 0.45-µm syringe filter units (MilliporeSigma) and the pellet was discarded. 1.5 mL of Ni-NTA agarose (equilibrated with buffer A supplemented with 0.1% Triton X-100) was added into the filtered supernatant and the mixture was rotated at 4 °C for 3 h. The slurry was then washed with 10 mL of buffer A supplemented with 0.1%

Triton X-100 for 4 times. Bound proteins were eluted with 6 mL of buffer B [50 mM Tris-HCl (pH 7.4), 500 mM NaCl, 0.1 mM EDTA, 0.1 mM EGTA, 0.1% Triton X-100, and 200 mM imidazole] for 1 h at 4 °C. The elution was filtered through a 0.45-μm syringe filter unit and dialyzed in a Slide-A-Lyzer™ dialysis cassette (10K MWCO; Thermo Fisher Scientific) overnight against an imidazole-free buffer [50 mM Tris-HCl (pH 7.45 at 4 °C) and 300 mM NaCl] and then loaded onto a Superdex 200 pg column for size-exclusion chromatography. Fractions corresponding to the 6×His-3×FLAG-TEV-MELT¹²⁻¹⁴-mNeonGreen-2×FKBP (determined by molecular weight estimation and SDS-PAGE analysis) were later used in the *in vitro* kinase assay.

2.8.3 *In vitro* kinase assay

The substrate 6×His-3×FLAG-TEV-MELT¹²⁻¹⁴-mNeonGreen-2×FKBP was incubated with 6×His-MBP-TEV-FRB*-mCherry-MPS1^{kinase domain} at 30 °C for 5 min – 2 h in the kinase buffer [10 mM Tris-HCl (pH 7.5), 100 mM NaCl, 10 mM MgCl₂, and 1 mM DTT] supplemented with 500 nM rapamycin and 0.25 mM ATP. The reactions were stopped with the Laemmli Sample Buffer (supplemented with β-mercaptoethanol, Bio-Rad Laboratories). Phosphorylation of the substrate was detected by our custom-made anti-MEIPTRSHTTALEC phospho-specific rabbit polyclonal antibody (GenScript). Equal inputs of the substrate and the recombinant kinase across different groups were validated by silver staining (Bio-Rad Laboratories).

2.8.4 Cell culture and Cre-*lox* recombination-mediated cassette exchange (RMCE)

All HeLa-A12 cells were cultured in Dulbecco's Modified Eagle's Medium (DMEM, with high glucose and phenol red, without glutamine, sodium pyruvate, or HEPES; Gibco) supplemented with 22 mM of HEPES (Corning), 9% (by volume) of fetal bovine serum (Corning), and 1× GlutaMAX (Gibco). This medium is henceforth referred to as the complete DMEM.

For Cre-*lox* RMCE, Lipofectamine 3000 (Invitrogen) is used to co-transfect 1.5 μg of a circular plasmid carrying the transgene cassette and 50 ng of the circular pCAGGS-nlCre plasmid. 0.5–2 μg/mL of puromycin was added 1.5 d later for 3 d to select for stably-transfected HeLa-A12 cells. Puromycin-resistant colonies were then pooled together and subject to further validation by genotyping and/or immunoblotting.

2.8.5 Live-cell imaging on the IncuCyte® ZOOM system

Long-term fluorescence imaging of eSAC cell lines was conducted using the IncuCyte® ZOOM Live Cell Analysis System (Sartorius) equipped with a 20 \times objective. Cells were seeded in 12-well BioLite cell culture-treated plates (Thermo Fisher Scientific) 2 days before imaging in complete DMEM supplemented 2 μ g/mL doxycycline. 30 – 60 minutes prior to imaging, cells were washed once and FluoroBrite™ DMEM [supplemented with 9% (by volume) of fetal bovine serum (Corning) and 2 μ g/mL doxycycline] with or without 500 nM rapamycin were added. Phase-contrast and fluorescence images were acquired every 10 min at fixed positions.

CHAPTER 3

Enrichment of SAC Proteins at Kinetochores Strengthens the SAC Signaling Activity

The model which we proposed in Section 2.6 relies on certain basic preconditions. First, the competition among a large but physiologically relevant number of phosphorylated MELT motifs in the cell for the limited pool of SAC proteins can effectively diminish freely diffusive SAC proteins in the cytosol. Second, the co-localization of multiple SAC proteins on the same KNL1 scaffold boosts the SAC signaling activity. Our follow-up studies described in this chapter corroborate these preconditions in a kinetochore-based setting, reinforcing the idea that cooperative synergy plays a critical role in the sensitivity of the SAC.

This chapter is tailored from two of my submitted first-(co)author manuscripts [2, 3] with the inclusion of unpublished supplementary data (see Figures 3.2 and 3.3). Most figures are reproduced from the two manuscripts. I am the main contributor to all experiments except those in Figures 3.4 and 3.6C, which are credited accordingly in the corresponding caption.

3.1 Using CRISPR-Cas9-mediated genome editing to tag SAC genes with mNeonGreen *in situ*

A common practice to study the functions of a protein is to knock down the endogenous protein by RNAi and then rescue the cells with a mutated or truncated protein ectopically expressed in the cells. This is henceforth referred to as a knockdown-rescue experiment. This strategy may cause undesirable over-expression of SAC proteins, which affects the progression of mitosis [127] (see also Section 3.5), depletes the cytosolic pool of the corresponding binding partner and impairs the SAC signaling activity [93, 94, 95, 96], or even induces cell death (our unpublished imaging data of HeLa-A12 cells).

To prevent over-expression and facilitate live-cell imaging of SAC proteins, we utilized CRISPR-Cas9-mediated genome editing to tag SAC genes with a fluorescent protein *in situ* [99, 128], which may better protect any endogenous transcriptional and translational regulations by preserving the introns and 5'/3'-untranslated regions (UTRs; see Figure 3.3). This chapter focuses on three proteins from different layers of the SAC recruitment cascade: BUB1, BUBR1, and MAD1. We fused mNeonGreen to the N-terminus (upstream of the first exon) of *BUBR1* and *BUB1* as well as the C-terminus (downstream of the last exon and before the stop codon) of *MAD1* to enable live-cell fluorescence imaging. We chose to tag *MAD1* at its C-terminus based on a previous report that large N-terminal tags may disrupt the localization of MAD1 to the corona [25]. mNeonGreen is separated from the tagged protein by a short flexible linker (see Section 3.7.1) so that the binding dynamics, functions, and turnover of the protein may be minimally affected. mNeonGreen has fast maturation kinetics (shorter than 10 min at 37 °C [116]) compared to the turnover rates of BUBR1 and BUB1 in nocodazole-arrested mitotic cells [70, 129]. These CRISPR-Cas9-edited cell lines can also serve as a reference for the endogenous expression of these SAC proteins for knockdown-rescue experiments (Figure 3.6D and the next chapter).

Band intensities from immunoblotting (Figure 3.1A) and genotyping PCR (Figure 3.1B) suggested that a half of BUBR1 proteins in mitotic mNG-*BUBR1* cells and slightly over a half of MAD1 proteins in mitotic *MAD1*-mNG cells were tagged with mNeonGreen. Our genotyping PCR revealed only one band corresponding to the edited mNG-*BUB1* allele (Figure 3.1B). However, immunoblotting using three different antibodies consistently revealed the coexistence of both mNG-tagged and wildtype BUB1 proteins in mitotic mNG-*BUB1* cells (Figures 3.1C and 3.1D). We suspected that the double-strand break induced by Cas9 may have induced unexpected chromosomal rearrangement at the *BUB1* locus, rendering the “wildtype” allele unable to be amplified by the genotyping primers but still able to express the wildtype BUB1 protein.

To validate this, we conducted 5'-rapid amplification of cDNA ends (RACE) to sequence the 5' region of all *BUB1* mRNAs in the mNG-*BUB1* cells. As a control, We only detected wildtype *BUB1* mRNAs from the host HeLa-A12 cell line. However, from the mNG-*BUB1* cells, we identified both the mRNA translating into mNG-BUB1 as well as an mRNA that has an unexpected 5'-UTR (Figure 3.3). The open reading frame of this unexpected mRNA still encodes the wild-type BUB1 protein. The exact configuration of the probable chromosomal rearrangement is unknown because 5'-RACE can only reveal the sequence of the 5'-UTR but not where the genotyping primers are supposed to bind. Nonetheless, this likely explains why the genotyping primers could not amplify the “wildtype” allele.

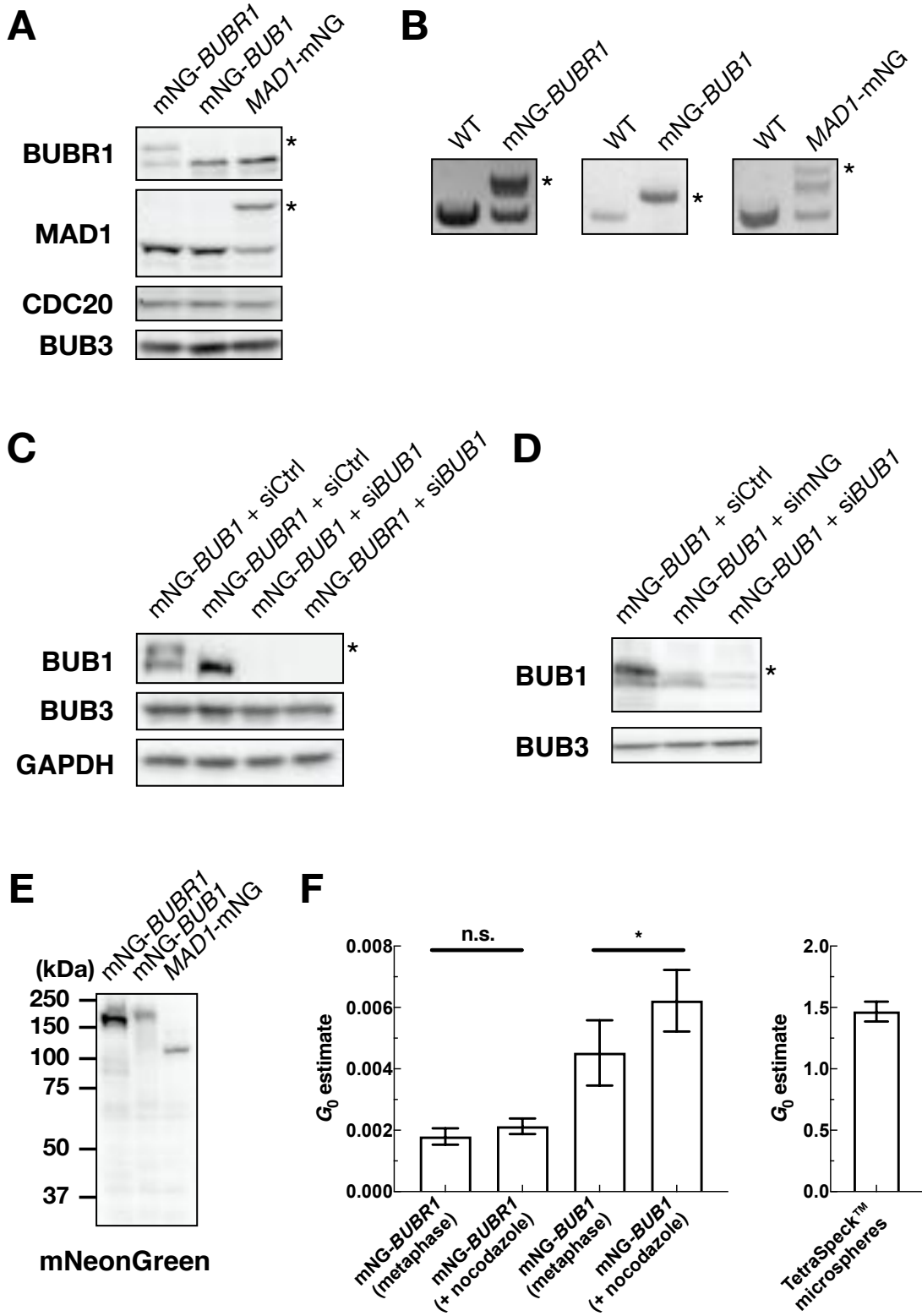


Figure 3.1: Utilizing CRISPR-Cas9-mediated genome editing to fuse mNeonGreen to *BUBR1*, *BUB1*, and *MAD1* *in situ*.

(Caption of Figure 3.1 continued from a previous page) (A) Immunoblots of mitotic mNG-*BUBR1*, mNG-*BUB1*, and *MAD1*-mNG HeLa-A12 cells. Bands marked by asterisks correspond to proteins tagged by mNeonGreen. These blots are representative of three independent experiments. BUBR1 bands were detected by horseradish peroxidase-catalyzed chemiluminescence. MAD1, CDC20, and BUB3 bands were detected by fluorescent dye-conjugated secondary antibodies. CDC20 and BUB3 levels in HeLa-A12 cells were not affected by the *in situ* tagging of *BUBR1*, *BUB1*, or *MAD1*. The weak bands below the strong wildtype bands in the MAD1 blot likely correspond to the alternatively-spliced MAD1 β [130]. (B) The genotyping (and subsequent sequencing) results verified the expected in-frame fusion of mNeonGreen. Bands marked by asterisks correspond to the mNeonGreen-tagged alleles. The middle bands from mNG-*BUBR1* and *MAD1*-mNG cells were hybrid DNAs composed of one strand of the PCR product from the edited allele and one strand of the PCR product from the wildtype allele. These hybrid DNAs were thermodynamically less stable (Figure 3.2). Adrienne Fontan also contributed here. (C) Immunoblots using lysates of the mNG-*BUB1* HeLa-A12 cell line and another control genome-edited HeLa-A12 cell line revealed that BUB1 proteins in the mNG-*BUB1* HeLa-A12 cell line were only partially tagged with mNeonGreen. Cells were treated with thymidine and then nocodazole overnight. The left two lanes were mitotic lysates harvested by mitotic shake-off while the right two lanes were pools of all cells (the fraction of cells in mitosis was significantly lower due to the knock-down of *BUB1*). The immunoblot against BUB1 here was using a commercial rabbit antibody (see Section 3.7.8). (D) Knocking down *BUB1* using a siRNA against mNeonGreen (simNG) or a siRNA against *BUB1* (si*BUB1*) confirmed that the lower band in the immunoblot against BUB1 is BUB1 (rather than due to cross-reactivity). The immunoblot against BUB1 here was using a commercial mouse antibody (see Section 3.7.8). We also tested another custom antibody from a previous study [131] and saw similar band patterns, further confirming that the lower band in the immunoblot against BUB1 corresponded to the wildtype BUB1. (E) The majority of mNeonGreen-tagged proteins in mitotic mNG-*BUBR1*, mNG-*BUB1*, and *MAD1*-mNG HeLa-A12 cells were full length. The contribution of partial degradation or cleavage products to the fluorescence signal in Figure 3.1F is minor. (F) According to the FCS data, the metaphase concentration of mNG-BUBR1 and mNG-BUB1 in the corresponding genome-edited HeLa-A12 cell line is $(2.4 \pm 0.4) \times 10^2$ nM and $(1.0 \pm 0.25) \times 10^2$ nM, respectively. Concentration measurements were calibrated by 0.1- μ m TetraSpeckTM microspheres with a nominal concentration of about 0.30 nM. G_0 , the auto-correlation at the 0-time lag, is inversely proportional to the average number of freely diffusive fluorescent proteins/particles in the excitation volume (see Section 3.7.4). Each error bar represents the mean value \pm the 95% confidence interval of each group. Results were pooled from two independent experiments.

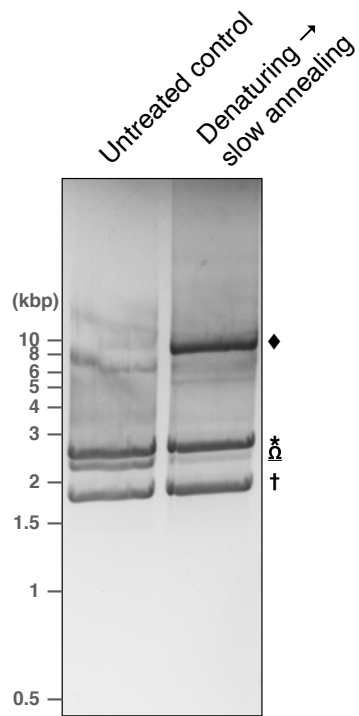


Figure 3.2: Genotyping PCR products (using the genome of the heterozygous mNG-*BUBR1* HeLa-A12 cell line as the template) feature hybrid double-stranded DNAs that are thermodynamically unfavorable.

Genotyping PCR products were purified using the GeneJET PCR Purification Kit (Thermo Fisher Scientific) and then equally split into 2 tubes. One of the tubes (right lane) was then placed in a boiling water bath for 5 min and slowly cooled to room temperature, while the other tube (left lane) sit at room temperature. Diamond: likely to be a certain higher-order origami complex. Asterisk: the PCR product of the edited mNG-*BUBR1* allele (2519 bp, confirmed by sequencing). Cruciform: the PCR product of the wildtype *BUBR1* allele (1793 bp, confirmed by sequencing). Ω : hybrid DNAs made up of one strand from the PCR product of the edited mNG-*BUBR1* allele and a complementary strand from the PCR product of the wildtype *BUBR1* allele. The identity of this band was also confirmed by sequencing (data not shown). Similar hybrid DNAs likely also existed in the purified *MAD1*-mNG genotyping PCR products Figure 3.1B.

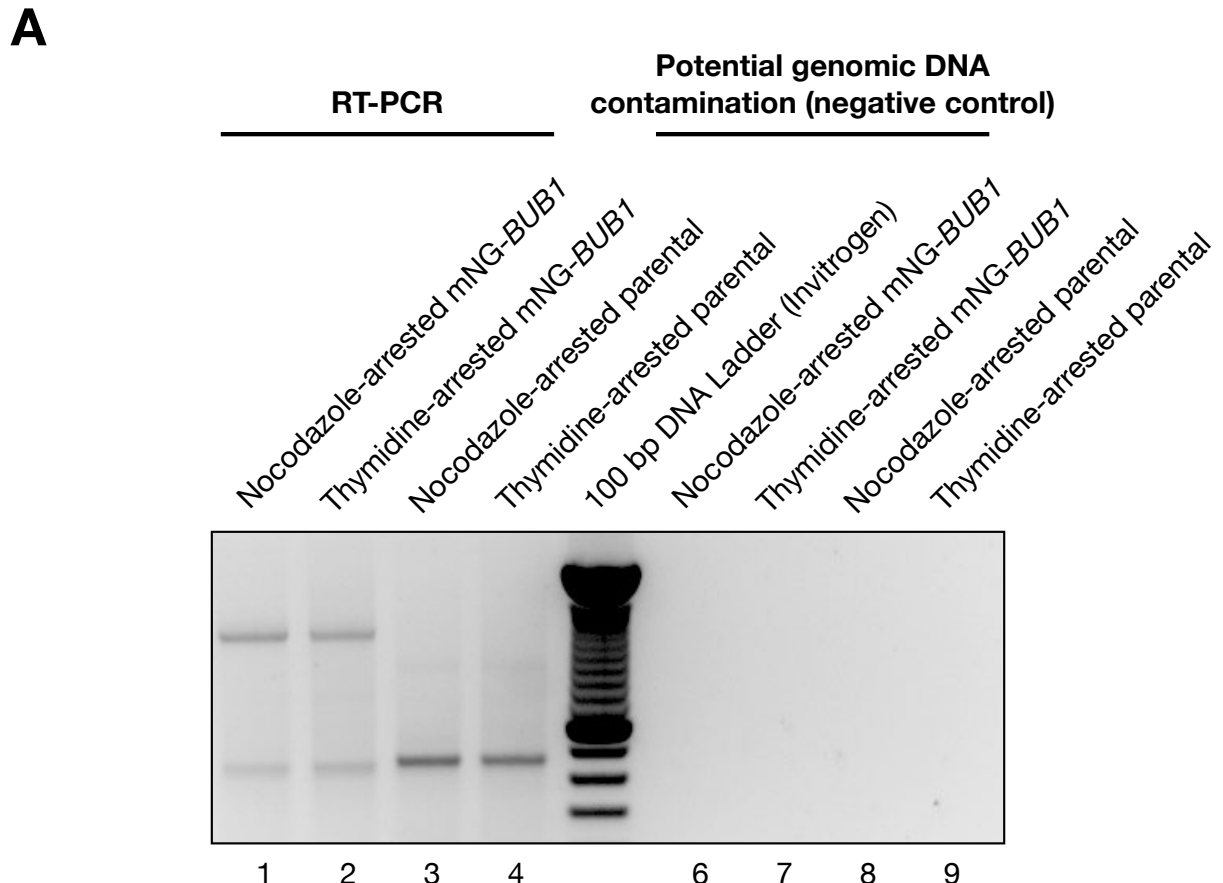


Figure 3.3: 5'-RACE identifies the 5'-UTR sequences of different *BUB1* alleles in the genome-edited *w⁻NC BUB1* cell line.

(Caption of Figure 3.3 continued from a previous page) (A) 5'-RACE RT-PCR products using mitotic or G₁ total RNA extracts from the mNG-*BUB1* genome-edited HeLa-A12 cell line (labeled as “mNG-*BUB1*”) or the host HeLa-A12 cell line (labeled as “parental”). The right four lanes used purified total RNAs directly as the PCR templates without the reverse transcription reaction, which served as negative controls for any remaining genomic DNA that could affect the interpretation of these results. (B) The 5'-UTR of wild-type *BUB1* mRNA (highlighted in yellow) identified from the host HeLa-A12 cell line and the 5'-UTR of the novel *BUB1* mRNA identified from the mNG-*BUB1* cells that still translates into the wildtype BUB1 protein (the two-part gray arrows). The 5'-UTR of the wildtype *BUB1* mRNA is composed of -68 to -1 of the sense strand. The 5'-UTR of the novel *BUB1* mRNA is composed of -206 to -260 of the anti-sense strand followed by -13 to -1 of the sense strand, which indicates a possible chromosomal rearrangement event. The 5'-UTR of the mRNA transcribed from the mNG-*BUB1* allele (corresponding to the upper bands of the first 2 lanes on the left) is the same as the 5'-UTR of the mRNA transcribed from the wildtype *BUB1* allele in the host HeLa-A12 cell line, confirming that our *in situ* tagging does not affect the transcription start site (TSS) of *BUB1*. Different clones may have slightly varied TSSs (data not shown). For reference, the PAM sequence used in the initial CRISPR-Cas9-mediated genome editing spans from -19 to -17 of the sense strand. The nucleotide coordinates are based on the reference sequence (NC_000002.12, chromosome 2 of the GRCh38.p13 primary assembly).

3.2 The recruitment of BUB1 to signaling kinetochores had a major depletion effect on the cytosolic pool of BUB1

To test whether the cytosolic pools of SAC proteins were depleted due to their recruitment to signaling kinetochores, we quantified the abundance of BUB1 and BUBR1 in cells treated with either 10 µM MG132 (a proteasome inhibitor which arrests mitotic cells in the metaphase independently of the SAC) or 330 nM nocodazole. In MG132-treated cells, SAC proteins are mostly in the cytosol rather than recruited to the kinetochores [90, 132]. By comparing the cytosolic concentration of SAC proteins between cells treated with two different drugs, we can assess the depletion effect.

Using fluorescence correlation spectroscopy (FCS), we estimated the cytosolic concentration of mNG-BUBR1 and mNG-BUB1 in the corresponding MG132-treated HeLa-A12 cell line to be $(2.4 \pm 0.4) \times 10^2$ and $(1.0 \pm 0.25) \times 10^2$ nM, respectively (see Figures 3.1E and 3.1F). Importantly, we confirmed that the cytosolic concentration of BUB1 in nocodazole-treated cells was significantly lower than that in MG132-treated cells, indicating that the recruitment of BUB1 to signaling kinetochores diminished the cytosolic pool of BUB1. This effect was not statistically significant for BUBR1. One explanation could be that the cellular concen-

tration of BUBR1 is higher than BUB1. Given that BUBR1 is mainly recruited to signaling kinetochores by heterodimerizing with BUB1 and that the stoichiometry is 1 : 1 *in vitro* [33], the depletion effect is naturally less prominent.

3.3 The numbers of BUBR1, BUB1, and MAD1 recruited per signaling kinetochore are inversely correlated with the total number of signaling kinetochores in the cell

A natural outcome of the depletion effect partially demonstrated in the previous section is that the number of SAC proteins recruited per signaling kinetochore will be inversely correlated with the total number of signaling kinetochores in the cell. Indeed, our previous measurement in the budding yeast [133] proved this to be the case. To validate this in our genome-edited HeLa-A12 cells, we first need to obtain mitotic cells containing distinctly different numbers of signaling kinetochores.

To obtain mitotic cells with nearly all kinetochores activating the SAC, we treated mitotic cells with 330 nM nocodazole, a drug that destabilizes microtubules. These nocodazole-treated cells resemble normal mitotic cells at the start of the prometaphase.

To obtain mitotic cells with a much smaller number of signaling kinetochores, we treated mitotic cells with GSK923295, a CENP-E inhibitor that impairs chromosome alignment [100]. In these cells, usually a variable but smaller number of chromosomes are stranded near the spindle poles (Figure 3.4A). We analyzed only those cells that contained ten or less than ten polar chromosomes. Kinetochores on these polar chromosomes are either unattached or laterally attached, which activate the SAC [19, 22]. These GSK923295-treated cells arguably (see Section 3.6) resemble normal mitotic cells near the end of the prometaphase.

In nocodazole-treated cells, the number of mNG-BUBR1 and MAD1-mNG proteins recruited per signaling kinetochore in nocodazole-treated cells was lower than that of mNG-BUB1 recruitment (Figure 3.4B). Importantly, BUBR1, BUB1, and MAD1 recruitment per signaling kinetochore were all significantly increased when cells were treated with GSK923295 compared to nocodazole (Figure 3.4B). This confirms that the number of SAC proteins recruited per kinetochore is indeed inversely correlated with the number of signaling kinetochores in the cell.

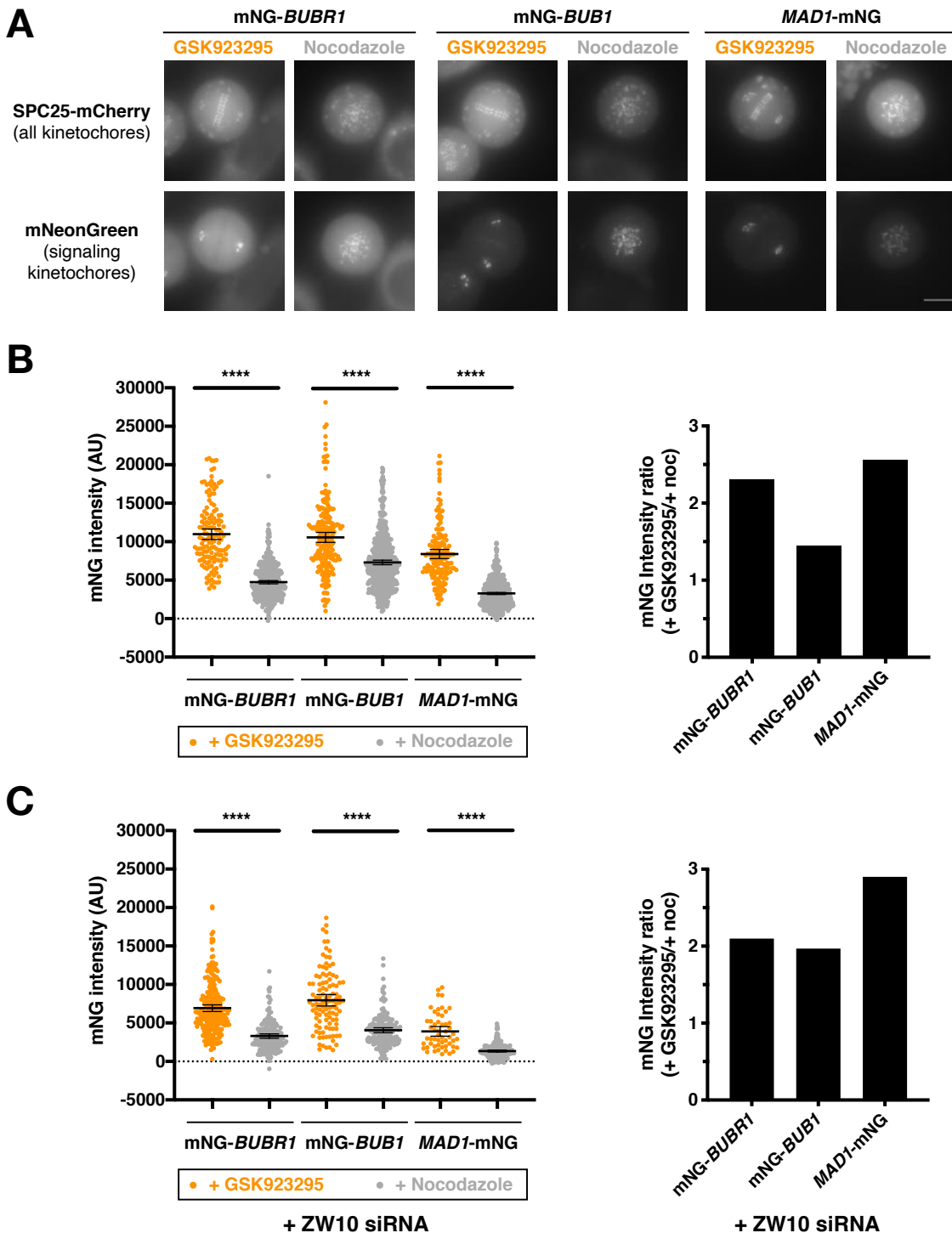


Figure 3.4: The numbers of BUBR1, BUB1, and MAD1 recruited per signaling kinetochore are inversely correlated with the total number of signaling kinetochores in the cell.

(Caption of Figure 3.4 continued from a previous page) Lauren Humphrey-Stark performed all imaging experiments and data analysis involved in this figure. (A) Representative micrographs showing cells from the three genome-edited HeLa-A12 cell lines treated with nocodazole or GSK923295. SPC25-mCherry labeled all kinetochores [12]. The coding sequence of SPC25-mCherry was integrated into the genome of these HeLa-A12 cell lines immediately downstream of the constitutive *EF1A* promoter (see Figure 2.1B). Brightness and contrast have been adjusted but the LUT for each channel (row) is universal for different groups (column). Scale bar, 10 μ m. (B) Left panel: quantification of mNeonGreen signals at individual signaling kinetochores from experiments illustrated in (A). Each dot represents the measurement from one signaling kinetochore. Error bars represent 95% confidence intervals of the mean. Results from at least two independent experiments are shown. Right panel: Pairwise ratios between the average mNeonGreen signals at individual signaling kinetochores of GSK923295-treated cells and nocodazole-treated cells in the left panel. (C) Similar to (B), except that all cells were additionally treated with a siRNA against *ZW10*.

In human cells, MAD1 is also recruited to the fibrous corona around a signaling kinetochore [26, 98], which may contribute to the measurement in Figure 3.4B through widefield fluorescence microscopy. The corona is mainly composed of the ROD-Zwilch-ZW10-Spindly (RZZS) complex [15, 16]. A previous study found conflicting dependency of the kinetochore localization of BUBR1 on the RZZS complex in *Xenopus* extracts versus HeLa cells [134]. Another study observed that the kinetochore localization of BUBR1 and BUB1 in the presence of 660 nM nocodazole even increased when cells were treated with a siRNA against *ROD* (see Figure 1E of [54]).

To dissect how much the core SAC pathway contributes to the recruitment of these SAC proteins at signaling kinetochores, we knocked down *ZW10*, a subunit of the RZZS complex, by a siRNA against *ZW10*. We then quantified the recruitment of the mNG-labeled SAC proteins to signaling kinetochores as before. Consistent with previous studies [52, 54], MAD1 recruitment was significantly lower in both GSK923295 and nocodazole-treated cells when the RZZS complex was knocked down (Figure 3.4C). The number of BUBR1 and BUB1 molecules recruited per signaling kinetochore was also reduced, which deviates from previous studies. We hypothesized that unlike our *in situ* tagging, the immunofluorescence labeling used in the quantification of the kinetochore localization of BUBR1 and BUB1 [54, 134] may be additionally affected by the accessibility of the antigen (BUBR1 and BUB1) to the corresponding antibody. Such accessibility could be increased by the removal of the fibrous corona on the periphery of kinetochores.

Importantly, our data showed that the number of SAC proteins recruited per signaling kinetochore was still inversely correlated with the total number of signaling kinetochores in a cell when *ZW10* was knocked down. This indicated that the competition between signaling

kinetochores for the limited pool of SAC proteins in a cell persisted even when only the core SAC signaling pathway was functional.

3.4 The equilibrium between the activity of MPS1 and counteracting phosphatases at signaling kinetochore is the same in nocodazole- and GSK923295-treated HeLa-A12 cells

The observed difference in the recruitment of SAC proteins on a per kinetochore basis in nocodazole- and GSK923295-treated cells may be alternatively attributed to different degrees of phosphorylation of MELT motifs. This could be an indirect result of the various effect of different drugs on the kinetochore-microtubule attachment (see Figure 3f of [59]). It may also be due to previously uncharacterized regulations of different drugs imposed on the activity of kinases and counteracting phosphatases at the kinetochore directly.

To test this alternative hypothesis in the HeLa-A12 cell line, we probed the equilibrium between the activity of kinases (mainly MPS1) and counteracting phosphatases at the kinetochore (henceforth referred to as “MPS1’s activity” for simplicity) using a similar phosphorylation sensor (MPS1sen-KT; see Figure 3.5A) to the one developed in a previous study [135]. The original idea of this Förster resonance energy transfer (FRET) sensor design was first proposed in [136]. The equilibrium between the activity of kinases and counteracting phosphatases determines the phosphorylation level of the substrate. If the substrate has a higher level of phosphorylation, FHA2 (the phospho-threonine binding domain from the yeast protein Rad53p) will have a higher affinity to bind to the substrate, thereby distancing the donor and the acceptor better and resulting in lower FRET efficiency. The expression cassette of the recombinant sensor is under the regulation of TRE and stably integrated into the genome of HeLa-A12 cells via Cre-*lox* RMCE. The acceptor and the donor have a fixed 1 : 1 stoichiometry by design and the recombinant sensor was mostly intact in the cell (with no major partial degradation species like mScarlet-I-SPC24 alone; see the immunoblot in Figure 3.5B). Therefore, the ratio between the green channel readout and the raw FRET channel readout (even without corrections for the cross-excitation of the acceptor and the bleed-through of donor fluorescence) can be employed as a normalized measurement of the FRET efficiency (see Section 3.7.7) and serve as an indicator of MPS1’s activity.

We confirmed that MPS1sen-KT recruited to unaligned signaling kinetochores in both

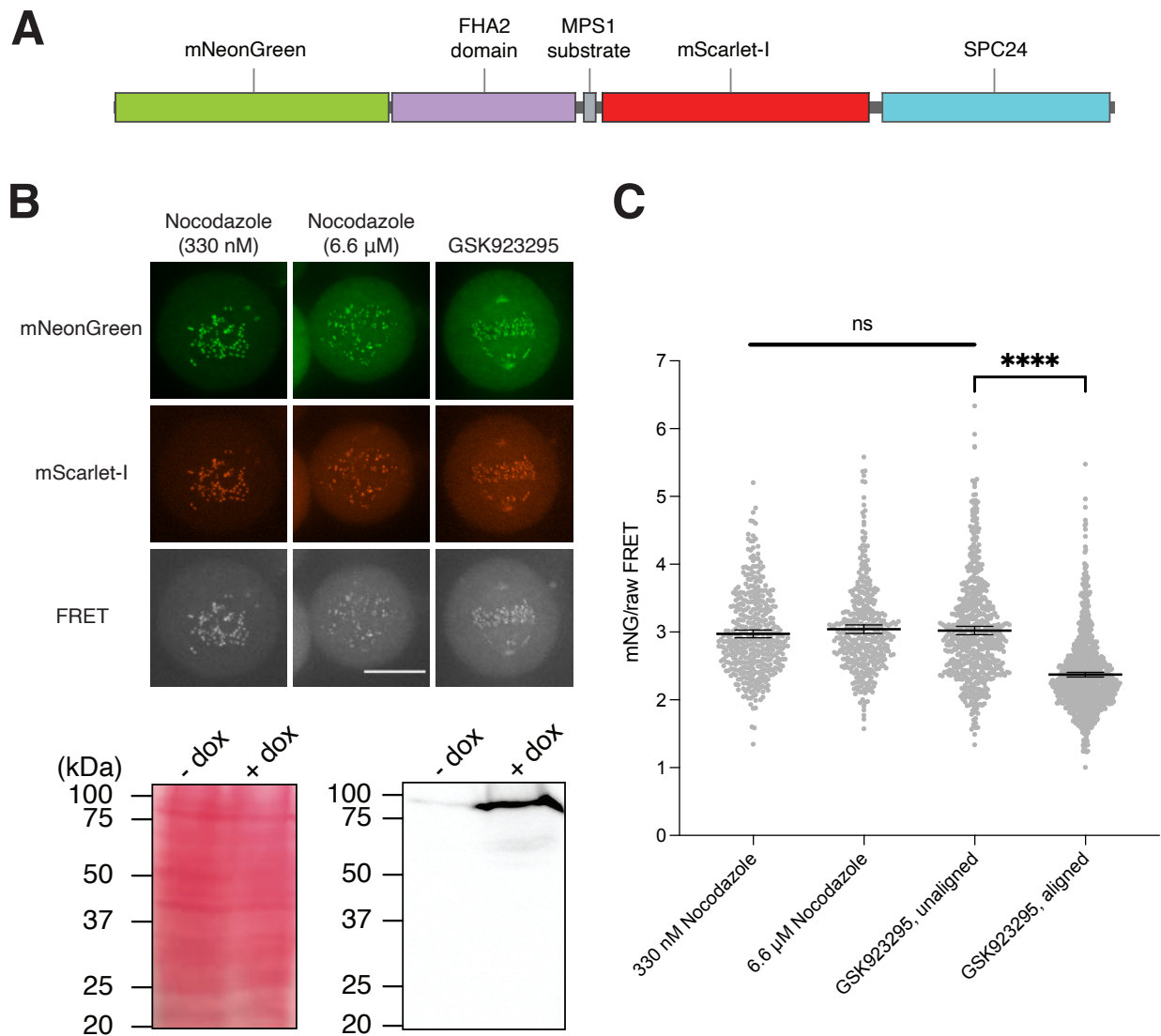


Figure 3.5: No difference in the MPS1-phosphatases equilibrium at signaling kinetochores was detected in HeLa A12 when cells were treated with different drugs at various concentrations.

(Caption of Figure 3.5 continued from a previous page) (A) The design scheme of MPS1sen-KT. The MPS1 substrate sequence is LLEDGTLAINW. The only difference between our version of the MPS1sen-KT and the original design [135] is that we used mNeonGreen/mScarlet-I as the acceptor/donor combination, which suits our confocal microscopy setup. (B) Top panel: representative confocal images of cells expressing MPS1sen-KT. MPS1sen-KT was recruited to both unaligned signaling kinetochores (in nocodazole- and GSK923295-treated cells) and non-signaling kinetochores aligned at metaphase plates (in GSK923295-treated cells) via its C-terminal SPC24 module. Brightness and contrast have been adjusted but the LUT for each channel (row) is universal for different groups (column). Scale bar, 10 μ m. Bottom panel: using an antibody against DsRed2 (which can detect many RFPs including mScarlet-I), we confirmed that MPS1sen-KT (with a theoretical molecular weight of 97.2 kDa) can be induced by doxycycline to express as a full-length protein with negligible partial degradation or cleavage products in the RMCE HeLa-A12 cells (right blot). The Ponceau S staining of the same blot before blocking (left blot) served as the loading and transfer control. (C) A summary of a normalized FRET metric (mNeonGreen signal/FRET signal) in HeLa A12 cells treated with different drugs at various concentrations in (B). Each gray dot represents a single kinetochore measurement. Data were compiled from at least two independent experiments (with more than 40 cells and 400 kinetochores in each group). Mean values \pm 95% confidence intervals are overlaid. Data from cells treated with 45 nM, 90 nM, and 200 nM GSK923295 were pooled together (they have no significant difference from one another) to simplify the presentation. Welch's analysis of variance (ANOVA) test [$W(DFn, DFd) = 1.339(2.000, 917.0)$, $p = 0.2626$] was performed for the three columns on the left. The unpaired *t*-test with Welch's correction was performed to compare non-signaling kinetochores aligned at metaphase plates with unaligned signaling kinetochores in GSK923295-treated cells. Statistical tests are performed in Prism 9.

nocodazole- and GSK923295-treated cells had lower FRET efficiencies (higher MPS1's activity) compared to MPS1sen-KT recruited to non-signaling kinetochores aligned at metaphase plates in GSK923295-treated cells (Figure 3.5C), consistent with the previous study [135]. However, in contrast to [135], we did not observe any difference in MPS1's activity at unaligned signaling kinetochores in nocodazole- versus GSK923295-treated cells. This was irrespective of the concentrations of respective drugs and the reason for the conflicting observations may be cell line-specific. As far as the HeLa-A12 cell line is concerned, the difference in the numbers of SAC proteins recruited per signaling kinetochore in nocodazole- and GSK923295-treated cells should be mainly attributed to the difference in the total number of signaling kinetochores, which all compete for the limited pools of SAC proteins in the cell based on the law of mass action.

3.5 Recruitment of BUBR1 by BUB1 *per se* contributes to the activity of the kinetochore-based SAC signaling

Lastly, we sought to prove that the co-localization of multiple SAC proteins on the same KNL1 scaffold cooperatively boosts the kinetochore-based SAC signaling activity. Testing this non-linearity *in vivo* is currently beyond our capability considering the technical challenge to quantify the real-time signaling activity for each signaling kinetochore. As a compromise, we set out to examine whether enrichment of SAC proteins at kinetochores strengthens the SAC signaling activity.

Previous studies showed that BUBR1 is mainly recruited to signaling kinetochores by heterodimerizing with BUB1 [33, 34]. BUB1 is an important hub protein that binds to other SAC proteins (like CDC20 and MAD1 which coordinately promote the formation of the CDC20-MAD2 heterodimer *in vitro* and in *Caenorhabditis elegans* [27, 28]). We reasoned that BUBR1's recruitment to signaling kinetochores by BUB1 may cause the local enrichment of BUBR1 near where the CDC20-MAD2 dimer is formed and thereby facilitate the assembly of the MCC better than cytosolic free BUBR1 does. Our eSAC activator-based mitotic duration assays (using truncations of BUB1 as the scaffold protein instead of the recombinant KNL1 phosphodomain in Chapter 2) showed that the recombinant BUB1 which can bind BUBR1 promotes the SAC signaling activity better than the recombinant BUB1 which is unable to bind BUBR1 does (manuscript in preparation). However, a previous study showed that abolishing the heterodimerization between BUBR1 and a recombinant,

kinetochore-tethered BUB1 did not affect the SAC signaling activity [137]. Moreover, two previous BUBR1 knockdown-rescue experiments in nocodazole-treated cells published by different research groups demonstrated that BUBR1's recruitment to signaling kinetochores by BUB1 counter-intuitively shortens the duration of the mitotic arrest [33, 34]. Even though the two studies deleted different segments of BUBR1's heterodimerization domain which mediates BUBR1's interaction with BUB1 (a.a 440-460 [34], henceforth referred to as "HD^{short}", versus a.a. Δ432-484 [33], henceforth referred to as "HD") and used different concentrations (~100 nM in [34] versus 50 nM in [33]) of nocodazole to induce signaling kinetochores, their basic observations were nonetheless consistent. We also did a similar knockdown-rescue experiment in GSK923295-treated cells comparing the SAC signaling activity of wildtype BUBR1 and BUBR1(ΔHD^{short}), whose results were also consistent with these two studies (Figure 3.6B). These conflicting pieces of evidence inspired us to examine the matter more carefully.

We noted that first, there lacked rigorous control over the expression level of the ectopic recombinant BUBR1 to match the physiological expression of endogenous BUBR1 in the knockdown-rescue experiments in [33, 34].

Second, the concentrations of nocodazole used in these two studies allowed the existence of some spindle microtubules [26]. However, PP2A's recruitment by BUBR1's kinetochore attachment regulatory domain (KARD) to signaling kinetochores is known to contribute to the silencing of the SAC either directly (by dephosphorylating the MELT motif [66] or BUB1 [65]) or indirectly (by stabilizing the kinetochore-microtubule attachment [89, 90, 91, 92] or promoting PP1's recruitment [67]). PP2A's recruitment to signaling kinetochores might not be completely canceled by BUBR1(ΔHD)'s defective interaction with B56 [33], knockdown of B56's (due to probable incomplete knock-down), or KARD mutations ([34], which eliminated the binding of the B56α isoform [91]). The dual functions of BUBR1 (participating in the assembly of the MCC as well as promoting the recruitment of PP2A) converge on promoting accurate chromosome segregation during normal mitosis, but their entanglement complicates the validation of the role of BUBR1's localization to signaling kinetochores in the SAC signaling activity.

Third, although the depletion of BUBR1 does not affect the localization of CENP-E at signaling kinetochores in HeLa cells [52], the activity of kinetochore-localized CENP-E (to facilitate the transition of the kinetochore-microtubule attachment from lateral to end-on) is arguably affected by the loss of interaction with BUBR1 [20] when cells are rescued by heterodimerization domain-truncated BUBR1, which may thereby affect chromosome congression.

Therefore, we designed and performed a new BUBR1 knockdown-rescue experiment. Here, the SAC signaling activity of BUBR1(Δ KARD) and BUBR1(Δ KARD, Δ HD) was compared (Figure 3.6A). The truncation of KARD (a.a. 665-682) abolishes the binding of B56 α [90] and likely other isoforms of B56 onto BUBR1 as well [138, 139], which allow us to dissect whether the recruitment of BUBR1 to the signaling kinetochore *per se* contributes to the SAC activity. Additionally, mNG-BUBR1(Δ HD, Δ KARD) lacks the heterodimerization domain (HD). We imaged our genome-edited mNG-*BUBR1* HeLa-A12 cell line (treated with the AllStars negative control siRNA) at the same time to serve as a reference for the endogenous expression of BUBR1 (first column, Figure 3.6D). Only mitotic cells having $0.5\times - 2\times$ the average mNeonGreen intensity of mNG-*BUBR1* HeLa-A12 cells during mitosis were included in the analysis (noted that only about half of endogenous BUBR1 proteins are tagged in the CRISPR-Cas9-edited cell line).

Just like what was shown in [33], mNG-BUBR1(Δ HD, Δ KARD) had minimal localization at signaling kinetochores (Figure 3.6C). The mitotic arrest was induced by treatment with 25 nM of nocodazole [140] after thymidine release, where unattached kinetochores can be observed while metaphase plates remain largely intact (Figure 3.6C).

Our knockdown of *BUBR1* was sufficient to almost completely abolish the SAC signaling activity (first two columns, Figure 3.6D). mNG-BUBR1(Δ KARD)-rescued cells take longer in mitosis than the control group (the third column versus the first column, Figure 3.6D), which is consistent with previous studies [67, 91]. Most importantly, our new data showed that mNG-BUBR1(Δ KARD)-rescued cells had a higher SAC signaling activity than mNG-BUBR1(Δ HD, Δ KARD)-rescued cells did (Figure 3.6D), directly supporting that the recruitment of BUBR1 *per se* contributes to the activity of the kinetochore-based SAC signaling.

3.6 Discussion

In this chapter, we demonstrated that the competition among a large number of signaling kinetochores can effectively diminish freely diffusive SAC proteins in the cytosol. This, instead of a potential shift in the degree of phosphorylation of MELT motifs, presumably explains why the numbers of SAC proteins recruited per signaling kinetochore are inversely correlated with the total number of signaling kinetochores in the cell. Using the recruitment of BUBR1 by BUB1 as an example, we showed that the co-localization of multiple SAC proteins on the same KNL1 scaffold likely strengthens the SAC signaling activity. Even though we did not rigorously prove that the cooperative signaling among multiple SAC proteins on

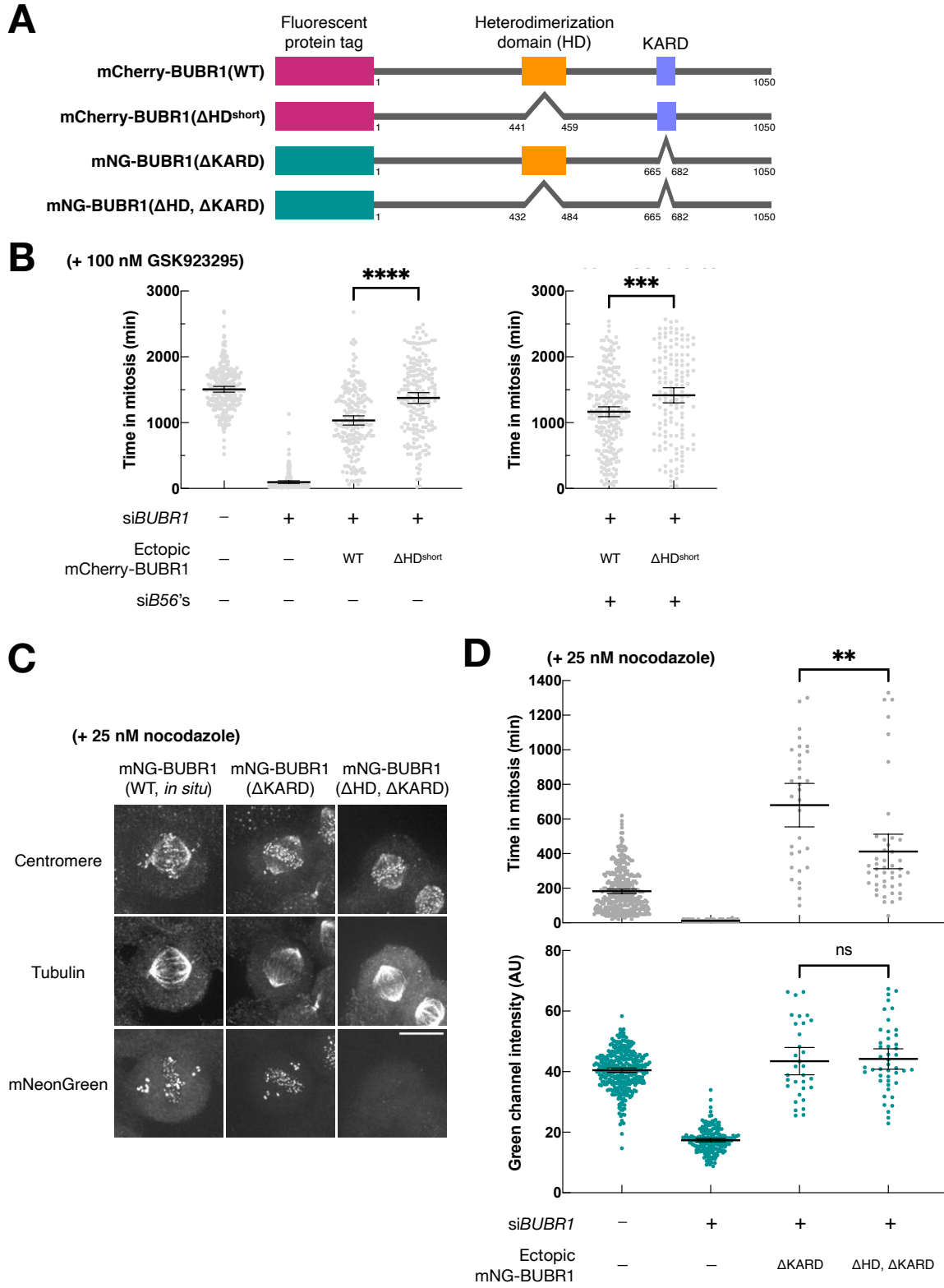


Figure 3.6: Recruitment of BUBR1 by BUB1 to signaling kinetochores *per se* contributes to the SAC signaling activity.

(Caption of Figure 3.6 continued from a previous page) (A) Diagrams (not to scale) of all ectopic recombinant BUBR1's used in experiments associated with Figures 3.6B to 3.6D. (B) A *BUBR1* knockdown-rescue experiment with mCherry-BUBR1 or mCherry-BUBR1(Δ HD^{short}) (with an HD truncation from [34]). [34] uses a shorter HD truncation compared to [33]. Therefore, it is denoted as Δ HD^{short} here. We used 100 nM GSK923295 to activate the SAC, which is different from both [34] (100 nM nocodazole) and [33] (50 nM nocodazole). Cells rescued with mCherry-BUBR1 consistently have a lower SAC signaling activity than cells rescued with mCherry-BUBR1(Δ HD^{short}), no matter whether B56's were knocked down. Cells treated with si*BUBR1* and rescued with mCherry-BUBR1 had a lower SAC signaling activity than the host cell line treated with the AllStars negative control siRNA, probably due to the lack of control over the expression of the ectopic mCherry-BUBR1. Each dot represents a cell, with more than 140 cells in each group. The mean value \pm the 95% confidence interval of each group is overlaid. Unpaired *t*-tests with Welch's correction are performed in Prism 9. Frank Ferrari also contributed to the data analysis here. (C) Confocal immunofluorescence micrographs (by Dr. Ajit Joglekar) showed that 25 nM nocodazole impaired the congression of a few chromosomes (which activated the SAC) in both genome-edited mNG-*BUBR1* HeLa-A12 cells (the first column) and the RMCE HeLa-A12 cells (the second and the third columns). In the second and the third columns, the RMCE HeLa-A12 cells were treated with si*BUBR1* and 0.5 μ g/mL of doxycycline to induce the ectopic expression of indicated mN-BUBR1 variants. Ectopically expressed mNG-BUBR1(Δ HD, Δ KARD) could not be detected at kinetochores (the third columns). Maximum *z*-projections of representative cells were shown for each condition (column) and channel (row). The LUTs for the mNeonGreen channel are the same across different conditions. Scale bar, 10 μ m. (D) A *BUBR1* knockdown-rescue experiment with mNG-BUBR1(Δ KARD) or mNG-BUBR1(Δ HD, Δ KARD) (with an HD truncation from [33]). Top panel: the duration of mitosis of individual cells treated with 25 nM nocodazole. Bottom panel: the average cytosolic mNeonGreen signal from the same cells right after the NEBD. In the heterozygous, genome-edited mNG-*BUBR1* HeLa-A12 cells (first two columns), both the wildtype allele and the edited mNG-*BUBR1* allele are susceptible to si*BUBR1*. In the RMCE HeLa-A12 cells (last two columns), ectopically expressed mN-BUBR1 variants are resistant to si*BUBR1*. Each dot represents a cell, with more than 30 cells in each group. Results are representative of two independent experiments. The mean value \pm the 95% confidence interval of each group is overlaid. Unpaired *t*-tests with Welch's correction are performed in Prism 9.

the same KNL1 scaffold boosts the kinetochore-based SAC signaling activity non-linearly, all data presented in this chapter supported the model in Section 2.6.

By knocking down *ZW10*, we dissected the contribution of the core SAC pathway to the kinetochore localization of SAC proteins. However, it should be noted that MAD1 may also be recruited to signaling kinetochores by the kinetochore protein CEP57 [53]. Further studies are needed to clarify whether the CEP57 pathway, the corona pathway, and the KNL1-BUB1 (core SAC) pathway of MAD1 recruitment work cooperatively.

The dynamic and stochastic establishment of kinetochore-microtubule attachment influences the localization of SAC protein and the dynein-dependent stripping of the corona [21, 76, 77]. We envision that right after the NEBD, all signaling kinetochores in a human cell are fully unattached. As the cell progress normally through the prometaphase, kinetochores gradually and independently establish end-on attachment to spindle microtubules. When we take a snapshot of a human cell near the end of the prometaphase, instead of one completely unattached kinetochores and 91 fully attached kinetochores that have already completely silenced their local SAC signaling activity, there may be three minimally attached kinetochores and 89 mostly attached kinetochores that are still in the process of stripping the corona and silencing the local SAC signaling activity. It remains to be seen whether (or how) the idea of dynamic regulation of the SAC signaling activity per kinetochore based on the total number of signaling kinetochores applies to this physiological scenario.

BUBR1 interacts with the kinase PLK1, a key regulator throughout mitosis [141]. mNG-BUBR1(Δ KARD) may still recruit PLK1 to signaling kinetochores, while mNG-BUBR1(Δ HD, Δ KARD) (which itself minimally localized to signaling kinetochores) can not. Although depletion of BUBR1 only results in a marginal reduction of PLK1 at signaling kinetochores [87], it remains to be examined how much the discrepancy in the localization of PLK1 contributes to the SAC signaling activity in the knockdown-rescue experiment of BUBR1.

In our manuscript, Soubhagyalaxmi Jema further showed that an increased expression of BUB1 enhanced the recruitment of BUBR1 to signaling kinetochores and the SAC signaling activity. These observations demonstrated that the SAC signaling activity is partially limited by the low expression level of BUB1 in HeLa-A12 cells. We hypothesized that this could be the result of a compromise among various sources of selection pressure. Like BUBR1, whose recruitment to signaling kinetochores improves the SAC signaling activity and promotes chromosome congression, BUB1 also has multiple functions (for example, in telomere replication [142], PLK1's localization [87], and the correction of erroneous kinetochore-microtubule attachment [88]). The MCC is even involved in the clathrin-mediated endocytosis of insulin

receptors [143, 144]. How these functions of SAC proteins interact and integrate is a fascinating topic that may lead to exciting discoveries.

3.7 Materials and methods

For methods of cell culture and Cre-*lox* RMCE, see Section 2.8.4.

3.7.1 CRISPR-Cas9-mediated genome editing

The guide RNAs (gRNAs) for *in situ* *BUBR1* and *BUB1* N-terminal mNeonGreen-tagging were 5'-CAGGAUGGCGGCGGUGAAGA-3' and 5'-GGUUCAGGUUUGGCCGCUGC-3', respectively. The gRNA for *in situ* *MAD1* C-terminal mNeonGreen-tagging was 5'-CAGACCGUGGCCUAGCCUG C-3'. Single guide RNAs (sgRNAs) were synthesized using the EnGen sgRNA Synthesis Kit (for the *Streptococcus pyogenes*-originated Cas9, New England Biolabs). The *SpCas9*-sgRNA ribonucleoprotein (RNP) complex was assembled at room temperature in a buffer consisting of 20 mM of HEPES-KOH (pH 7.5), 150 mM of KCl, 1 mM of MgCl₂, 10% (by volume) of glycerol, and 1 mM of DTT using 100 pmol of *SpCas9*-2×NLS (the QB3 MacroLab) and 120 pmol of sgRNA. The RNP complex and 1.5 µg of the corresponding linearized homology-directed repair template plasmid were co-transfected into 2 × 10⁵ – 5 × 10⁵ nocodazole-arrested mitotic HeLa-A12 cells [99] (harvested by the mitotic shake-off method) using the Cell Line Nucleofector™ Kit R (Lonza) following the manufacturer's instructions. After one week, green fluorescence-positive mitotic cells (arrested by 330 nM nocodazole for 16 h) were sorted directly into 96-well plates at one cell per well. Healthy colonies were subject to further validation by fluorescence imaging, genotyping (and subsequent sequencing), as well as immunoblotting.

Successfully edited alleles encode mNeonGreen-tagged SAC proteins wherein the corresponding wildtype protein and mNeonGreen are separated by a short flexible linker (mNG-BUBR1 and mNG-BUB1: GSGGSG; MAD1-mNG: GGAGGS GG).

3.7.2 Genotyping

HeLa-A12 genomic DNAs were purified using the Wizard® SV Genomic DNA Purification System (Promega). Genotyping primers (*BUBR1* forward primer 5'-CCTGGTCACATCTGAGCT AT-3', *BUBR1* reverse primer 5'-CTCAGTGAGACTCCAGTGTT-3', *BUB1* forward primer 5'-C

CCTCTACATGAAGGCGCTA-3', *BUB1* reverse primer *5'-GCTGCCCAAGGTAAACATT-3'*, *MAD1* forward primer *5'-GGACTTTCAGGGACGTGGT-3'*, and *MAD1* reverse primer *5'-GAGTTGGAGGAGGGGACTC-3'*) were designed to bind outside of homology arms to avoid false-positive colonies from integration of the homology-directed repair template plasmid to an off-target genomic locus. Genotyping PCR products were qualitatively analyzed by 1% agarose-TAE gel stained by ethidium bromide and individual bands were subsequently submitted for Sanger sequencing.

3.7.3 Rapid amplification of cDNA ends (RACE)

Interphase samples were arrested in 2.5 mM of thymidine for one day and then harvested by trypsinization. Mitotic samples were arrested in 2.5 mM of thymidine for one day, released into 100 ng/mL of nocodazole for 19 h, and finally harvested by mitotic shake-off. Harvested cells were snap-frozen by liquid nitrogen and stored at -80 °C until total RNA extraction.

Total RNA extraction was done using the Monarch Total RNA Miniprep Kit (New England Biolabs) following the manufacturer's instructions. The reverse transcription (RT) was done using the Template Switching RT Enzyme Mix (New England Biolabs) following the manufacturer's instructions. The sequence of the template-switching oligo is *5'-GCTAATCATTGC AAGCAGTGGTATCAACGCAGACTACTrGrGrG-3'*. The sequence of the *BUB1*-specific RT reverse primer (which binds to the fourth exon of *BUB1*) is *5'-CTCTGAAGGACAGCACTGGCAT-3'*.

The reverse transcription products were subsequently amplified by nested PCR. The template-switching oligo-specific forward primer (incorporating a *SpeI* restriction site at the 5' end) is *5'-GGACTAGTTGCAAGCAGTGGTATCAAC-3'*. The *BUB1*-specific reverse primer (incorporating an *XhoI* restriction site at the 3' end) is *5'-TATACTCGAGCTCTCCTTGGGCTTCC AGAT-3'*, which binds to the fourth exon of *BUB1* as well but upstream of the RT reverse primer.

RT-PCR products were visualized on an agarose gel. Individual bands were cut off and purified from the gel, and finally cloned into pBlueScript-KS(+) between the *SpeI* site and the *XhoI* site. For each band, multiple clones were randomly picked for sequencing.

3.7.4 Fluorescence correlation spectroscopy (FCS)

The total number of fluorophores in a homogeneous solution is $N_{\text{total}} := N_A c V_{\text{total}}$, where N_A is the Avogadro constant, c is the molar concentration of the fluorophore, and V_{total} is the total volume of the solution. The probability that a specific fluorophore molecule is

within the excitation volume V_0 ($\ll V_{\text{total}}$) at any given time is $p_0 := V_0/V_{\text{total}} \ll 1$. For freely diffusive fluorophores in a diluted solution, whether or not a specific fluorophore is within the excitation volume is independent of each other. Thus, the number of fluorophores inside the excitation volume at any given time N_0 has a binomial distribution $B(N_{\text{total}}, p_0)$. Therefore, the auto-correlation at 0-time lag

$$G_0 := \frac{\sigma_{N_0}^2}{\langle N_0 \rangle^2} = \frac{1 - p_0}{N_{\text{total}} p_0} \approx \frac{1}{N_A c V_0}.$$

Under a fixed live-cell imaging setup [which includes the microscope (its alignment and the objective), the wavelength of the excitation light, the thickness of the coverslip (affecting the actual working distance), and the refractive index of the cytosol], V_0 is fixed. Therefore, G_0 is inversely proportional to the molar concentration of the fluorophore. The average number (or the variance of the number) of fluorophores inside the excitation volume observed over a long period should be close to the theoretical mean $\langle N_0 \rangle$ (or the theoretical variance $\sigma_{N_0}^2$).

All FCS data were collected on an Alba v5 Laser Scanning Microscope (ISS), connected to an Olympus IX81 inverted microscope main body [equipped with a UPLSAPO60XW objective (1.2 NA, Olympus)]. A Fianium WL-SC-400-8 laser (NKT Photonics) with an acousto-optic tunable filter was used to generate excitation pulses at a wavelength of 488 nm and a frequency of about 20 MHz. Excitation light was further filtered by a Z405/488/561/635rpc quadband dichroic mirror (Chroma). Emission went through a 655DCSPXR short-pass dichroic mirror (Chroma) and an FF01-531/40-25 filter (Semrock) and was finally detected by an SPCM-AQRH-15 avalanche photodiode (Perkin Elmer). The time-correlated single photon counting module to register detected photon events to excitation pulses was SPC-830 (Becker & Hickl). Data acquisition was facilitated by VistaVision (ISS). The excitation volume (V_0) was calibrated by taking FCS data from TetraSpeck™ microspheres (0.1 μm , Invitrogen) of known concentrations (vary across different batches).

3.7.5 RNA interference (RNAi)

Cells were transfected with siRNA in the morning. 2.5 mM of thymidine was added 8 h later and cells were incubated overnight. The next morning, cells were released from the thymidine block into fresh media. This sequence was then repeated once again and cells were released into FluoroBrite™ DMEM supplemented with 9% (by volume) of fetal bovine serum and 1× GlutaMAX and incubated for 6 h before the addition of mitotic drugs. Imaging was started at least 1 h after drug treatment.

Sense-strand sequences and working concentrations of small interfering RNA duplexes (siRNAs) used in this study include the *BUBR1* siRNA (5'-GAUGGUGAAUUGUGGAAUA-3', 40 nM [70]), *BUB1* siRNA (5'-CGAAGAGUGAUCACGAUUU-3', 40 nM [145]), and the *ZW10* siRNA (5'-UGAUCAAUGUGCUGUCAA-3', 100 nM [134]). The siRNAs against all five B56 isoforms were taken from the second pool in [146]. Desalted siRNAs modified by double-deoxythymidine overhangs at 3'-ends of both strands were synthesized by Sigma. The AllStars Negative Control siRNA (QIAGEN) was used as the control. All siRNAs were transfected into the cells via Lipofectamine RNAiMAX (Invitrogen) following the manufacturer's instructions.

3.7.6 Live-cell imaging

Cells were plated in a Nunc Lab-Tek II chambered coverglass (Thermo Scientific) or a 35-mm coverglass-bottomed dish (MatTek) and treated with drugs and/or siRNAs accordingly. For imaging, the chambered coverglass or the coverglass-bottomed dish was loaded into a CU-501 temperature and gas control system (Live Cell Instrument). The sample holder was maintained at 37 °C and ventilated by humidified 5% of CO₂ and the objective was maintained at 37 °C by a heating band.

Most wide-field, *z*-stack fluorescence imaging (except the measurement of FRET efficiency of MPS1sen-KT) was performed on a Nikon Eclipse Ti-E/B inverted microscope, with a CFI Plan Apochromat Lambda 100×, 1.45 NA oil objective (Nikon). The intermediate magnification selector knob was switched to 1× unless specified otherwise. The microscope was equipped with an H117E1 motorized stage (Prior Scientific) and a NanoScanZ 100 piezo stage (Prior Scientific). A SPECTRA 5-LCR-XA Light Engine (Lumencor) served as the excitation light source. The 475 nm-centered band of excitation light was used for the green channel and the 575/30-nm-filtered band of excitation light was used for the red channel. An ET-EGFP/mCherry filter cube (Chroma Technology) was used as the dichroic mirror, where the built-in emission filter on the cube has been removed. Emission light in the red channel was filtered by an ET632/60m (Chroma Technology). Emission light in the green channel was filtered by an ET525/50m (Chroma Technology). Emission filters were mounted on a high-speed filter wheel (Prior Scientific) positioned in the light path before the iXon3 EMCCD camera (Andor Technology) operating in the conventional CCD mode. Signaling kinetochores in GSK923295-treated cells were identified by their polar positioning and the enrichment of localized SAC proteins on them. Custom MATLAB programs [147] were used to quantify kinetochore-localized fluorescence signals.

The FRET measurement with MPS1sen-KT was also performed on a Nikon Eclipse Ti-

E/B inverted microscope, with a CFI Plan Apochromat VC 100 \times , 1.40 NA oil objective (Nikon). The intermediate magnification selector knob was switched to 1 \times . The microscope was equipped with an H117E1 motorized stage, a NanoScanZ 100 piezo stage, and an X-Light V2 L-FOV confocal unit with 60 μm pinholes (CrestOptics). A CELESTA Light Engine (Lumencor) served as the excitation laser source. The 477-nm line (at 25% power with an exposure time of 400 ms for each frame) was used for both the green and the FRET channels and the 546-nm line (at 50% power with an exposure time of 400 ms for each frame) was used for the red channel. A ZT488/543rpc (Chroma Technology) was used as the dichroic mirror. Emission through both the red and the FRET channels was filtered by an ET605/52m (Chroma Technology) while emission through the green channel was filtered by an ET525/36m (Chroma Technology). Images were acquired by a Prime 95B 25mm sCMOS camera (Teledyne Photometrics). Custom MATLAB programs [147] were used to quantify kinetochore-localized fluorescence signals.

Time-lapse live-cell imaging related to the knockdown-rescue experiments was performed on an ImageXpress Nano Automated Imaging System (Molecular Devices). A SOLA Light Engine (Lumencor) served as the excitation light source. Cells were plated on 24-well cell imaging plates (black plate with treated glass bottom, Eppendorf) and treated with drugs and/or siRNAs accordingly. Input humidified 5% CO₂ flow was maintained at around 19 psi and the environment chamber was maintained at 37 °C.

All SAC proteins tagged by mNeonGreen in this chapter (BUBR1, BUB1, and MAD1) feature inhomogeneous distributions between the cytosol and the nucleus/nuclear envelope in the prophase (data not shown). In principle, they can indicate the accurate timing of the nuclear envelope breakdown (NEBD) in each cell during the time-lapse imaging. However, due to the resolution limit and for consistency, we determined mitotic duration mainly based on cell morphology (from rounding-up at the NEBD to elongation at the anaphase onset) from transmitted-light images. This was facilitated by the semi-automatic image analysis pipeline described in Section 2.3.

3.7.7 Quantification of the FRET efficiency by kinetochore-localized fluorescence signals of MPS1sen-KT

Under fixed fluorescence microscopy settings of a given channel [the excitation line and its power, exposure time, optical components (including the objective, filters, dichroic mirrors, the confocal spinning disk, and the detector) in the light path and their alignment, etc.], the kinetochore-localized fluorescence signal (digital readout) should be proportional to the

number of localized mature fluorescence proteins. The coefficients are designated as g and r_x for mNeonGreen and mScarlet-I using the excitation light for mNeonGreen, respectively (the subscript “x” stands for cross-excitation as mScarlet-I is excited by the excitation light for mNeonGreen here). The number of unbleached mature mNeonGreen and mScarlet-I molecules at a given kinetochore are G and R , respectively. While measuring FRET using the excitation light for mNeonGreen and optics settings to detect the emission of mScarlet-I, the bleed-through coefficient of mNeonGreen’s fluorescence is designated as β . Under a FRET efficiency of ε ($0 \leq \varepsilon \leq 1$, which describes the quenching of mNeonGreen due to FRET), the proximity ratio Θ , a metric of FRET according to the definition in [147], can be expressed as

$$\Theta := \frac{F}{r_x R + \beta g G (1 - \varepsilon)} - 1,$$

where F is the measured raw FRET readout. F can be attributed to three sources: (1) the cross-excitation of mScarlet-I, (2) the bleed-through of mNeonGreen’s fluorescence, and (3) the actual fluorescence due to FRET (determined by the combined coefficient f for the excited fraction of mNeonGreen under the excitation condition of the FRET channel and the conversion from FRET emission photons reaching the detector to the digital readout, the FRET efficiency ε , and the effective quantum yield ϕ of mScarlet-I that reaches the detector).

$$F = r_x R + \beta g G (1 - \varepsilon) + f G \varepsilon \phi$$

In [135], the authors used the ratio between the mNeonGreen signal (measured from the green channel) and the raw FRET signal (without corrections of the cross-excitation of mScarlet-I and the bleed-through of mNeonGreen’s fluorescence) as the metric of FRET:

$$\Gamma := \frac{g G (1 - \varepsilon)}{F}.$$

Because MPS1sen-KT competes with endogenous SPC24 to get recruited to the outer kinetochore region, the number of kinetochore-localized sensors is variable for different kinetochores. However, the ratio between kinetochore-localized mNeonGreen and mScarlet-I is always 1 : 1. Ignoring photobleaching (only one z -stack is taken for each cell with a bare minimum amount of exposure) and assuming that maturation of mNeonGreen and mScarlet-I is independent of the kinases’ or phosphatases’ activity at kinetochores, $\sigma := R/G$ should also

be fixed. Hence, we have

$$\Theta = \frac{f\varepsilon\phi}{r_x\sigma + \beta g(1 - \varepsilon)},$$

$$\Gamma = \frac{g(1 - \varepsilon)}{r_x\sigma + \beta g(1 - \varepsilon) + f\varepsilon\phi}.$$

Importantly, both Θ and Γ are dimensionless metrics normalized against the variation in the kinetochore localization of MPS1sen-KT. Under a particular fluorescence microscopy setting, both Θ and Γ have a monotonic and hyperbolic relationship with the FRET efficiency and are interconvertible:

$$\Theta = \frac{g(1 - \varepsilon)}{r_x\sigma + \beta g(1 - \varepsilon)} \cdot \frac{1}{\Gamma} - 1.$$

3.7.8 Immunoblotting

To acquire unsynchronized HeLa-A12 cells, asynchronous cells were either scrapped or trypsinized off the surface of dishes. To acquire HeLa-A12 cells synchronized at G₁/S, an asynchronous population of cells were first treated with 2.5 mM thymidine overnight, washed in phosphate-buffered saline (PBS, Gibco), released into fresh complete DMEM for 8–9 h, and finally treated with 2.5 mM thymidine again overnight. Cells were then either scrapped or trypsinized off the dishes.

To acquire mitotic HeLa-A12 cells, cells were first synchronized in G1/S with 2.5 mM thymidine and then arrested in mitosis with 330 nM of nocodazole for 16 h. This procedure is henceforth referred to as the thymidine–nocodazole synchronization protocol.

Harvested cells were then washed once by PBS, pelleted down, and chilled on ice. Lysis was performed by directly adding 2× Laemmli sample buffer (Bio-Rad Laboratories, supplemented by 2-mercaptoethanol) at a ratio of 1 µL per 0.1 mg of cell pellets and pipetting up and down. Lysates were boiled immediately afterward for 10 min and then chilled on ice. 8 µL of supernatant was loaded onto each lane of a 15-well, 0.75-mm SDS-PAGE mini gel.

Primary antibodies (and their working dilution factors by volume) used included anti-BUBR1 (Bethyl Laboratories A300-995A-M, 1 : 1000), anti-MAD1 (GeneTex GTX109519, 1 : 2000), anti-CDC20 (Santa Cruz Biotechnology sc-13162, 1 : 200), anti-BUB3 (Sigma-Aldrich B7811, 1 : 500), anti-mNeonGreen (ChromoTek 32F6, 1 : 500), anti-GAPDH (Proteintech 60004-1-Ig, 1 : 5000), anti-BUB1 (three antibodies purified from different hosts were used: (1) Bethyl Laboratories A300-373A-M, 1 : 330, rabbit polyclonal antibody; (2) SB1.3 [131], 1 : 1000, sheep polyclonal antibody; (3) Abcam ab54893, 1 : 200, mouse monoclonal antibody), and

anti-DsRed2 (Santa Cruz Biotechnology sc101526, 1 : 5000). Digital images were acquired using an Azure C600 or 600 imaging system (Azure Biosystems).

CHAPTER 4

The Structural Flexibility of MAD1 Facilitates the Assembly of the Mitotic Checkpoint Complex (MCC)

In previous chapters, I present evidence of the cooperative synergy among multiple MELT motifs on the same KNL1 phosphodomain (I name it “the first layer” in the core SAC signaling pathway). This phenomenon is likely caused by SAC proteins that concurrently bind to these MELT motifs in close spatial proximity (collectively, “the second layer” in the core SAC signaling pathway). In this chapter, I will focus on the catalytic role of the MAD1-MAD2 heterotetramer (“the third layer”) in the assembly of CDC20-MAD2 [27, 28].

The formation of CDC20-MAD2, an MCC subcomplex, is considered to be the rate-limiting step in the assembly of the MCC [36]. How this reaction is catalyzed in the cell is unclear. Some studies showed that locking cytosolic MAD2 to the closed conformation inhibits the binding between CDC20 and MAD2 and compromises the SAC, even though the MAD2 protein in CDC20-MAD2 is in the closed conformation [148, 149, 150]. These findings suggest that the conformational change of MAD2 (from open to closed) and the formation of CDC20-MAD2 may be temporally coupled. In 2021, two papers published back-to-back (based on either *in vitro* reconstitution [27] or studies in *C. elegans* [28]) presented evidence supporting the spatio-temporal coupling between MAD2’s conformational change and the formation of CDC20-MAD2 (see Section 4.1), which offered critical molecular insight into the synergy in this process.

In this chapter, I approach the suggested spatio-temporal coupling from a different angle – by looking into the role of the conserved structural flexibility of MAD1 in this process. Based on the known partial structure of the MAD1-MAD2 heterotetramer and our knowledge of related protein-protein interactions, I reason that such spatio-temporal coupling between MAD2’s conformational change and the formation of CDC20-MAD2 has to rely on the structural

flexibility of MAD1 to take a predicted fold-back conformation. Indeed, our FRET data suggest that the C-terminal loop region of MAD1 enables the MAD1-MAD2 heterotetramer to take a fold-back conformation *in vivo*. Importantly, disrupting the structural flexibility of MAD1 by deleting this loop region impairs the SAC signaling activity. Mutating this loop region while keeping its flexibility maintains the SAC signaling activity, indicating that the structural flexibility (rather than the primary sequence specificity) of MAD1 is important to the SAC. Together with the biochemical data from our collaborators (Dr. Valentina Piano and Amal Alex from Dr. Andrea Musacchio's group at the Max Planck Institute of Molecular Physiology in Germany) as well as a recent structural study [151], we proposed a "knitting model" for the mechanism of the assembly of CDC20-MAD2 catalyzed by the MAD1-MAD2 heterotetramer. This model elaborates the spatio-temporal coupling between MAD2's conformational change and the formation of CDC20-MAD2, which could be key to understanding how cooperative synergy at this third layer of the core SAC signaling pathway contributes to the overall sensitivity.

We began this hypothesis-driven study independently in 2018, which has since evolved into a collaboration project. I am the sole contributor to most cell biology data here. Simon Han performed preliminary tests on the feasibility and physiological activity of internally tagged Mad2p in the budding yeast. *In vitro* reconstitution results from our collaborators will be mentioned, but those data are not included here.

4.1 The molecular mechanism of the formation of CDC20-MAD2: the "assembly line" model *versus* the "knitting" model

The formation of the CDC20-MAD2 dimer, an MCC subcomplex, is considered to be the rate-limiting step in the assembly of the MCC based on an *in vitro* study [36]. However, how the formation of CDC20-MAD2 is catalyzed in the cell was unclear for a long time. CDC20 has a flexible N-terminal region with a MAD2-interacting motif (MIM) and a C-terminal WD40 β -propeller fold [152] (in Figure 4.1B, the N- and C-terminal regions are represented by a light gray line and a light gray circle, respectively). MAD2 has three known conformations: the open conformation (denoted as O-MAD2 and illustrated as a magenta open lock with a circular body in Figure 4.1B), the intermediate conformation (denoted as I-MAD2 and illustrated as a peach open lock with a rectangular body in Figure 4.1B), and closed (denoted as C-MAD2 and illustrated as a red closed lock with a rectangular body

in Figure 4.1B) [153]. Although purified monomeric O-MAD2 spontaneously converts into C-MAD2 at 30 °C *in vitro* [154] (while the conversion of C-MAD2 back into O-MAD2 in the cell is mediated by TRIP13-p31^{comet} in an ATP-dependent manner [74]), this open-to-closed conformational switch may be further catalyzed in the cell. The popular “template model” [155] argues that the conformational switch may be facilitated by the dimerization between one C-MAD2 (bound to MAD1’s MIM in the MAD1-MAD2 heterotetramer) and another copy of MAD2 that undergoes the conformational switch. The MAD2 protein in complex with CDC20 is in the closed conformation, which buckles the MIM of CDC20 in a safety belt-like manner similar to how C-MAD2 binds to MAD1 [41, 46].

CDC20’s BOX1 (an N-terminal basic motif) binds to MAD1’s C-terminal RING finger-containing proteins, WD repeat-containing proteins, and DEAD-like helicases (RWD) domain phosphorylated by MPS1 [27, 37, 151] (illustrated in Figure 4.1B as the contact between CDC20’s light gray N-terminal region and MAD1’s dark green C-terminal domain). Given the spatial proximity between the reaction center of MAD2’s conformational switch and the MIM of CDC20, it is attractive to investigate the potential coupling between MAD2’s conformational switch (① in Figure 4.1B) and the binding between CDC20 and MAD2 (② in Figure 4.1B). Therefore, we set out to test two opposite models, which we named the “assembly line” model and the “knitting” model. As the names suggest, the “assembly line” model indicates that the two processes happen in two separate steps and newly switched MAD2 from step ① enters a free cytosolic pool and then participates in step ②, as if two steps in an assembly line mediated by a warehouse. In contrast, the “knitting” model indicates that like knitting, the two processes are closely coordinated in one step (*i.e.*, ① is coupled to ②). The two regions of the MAD1-MAD2 heterotetramer with known structures shown in the top panel of Figure 4.1A function as the two knitting needles. They are connected by a region of unknown structure, which is predicted to be a flexible loop (see Figure 4.2; this region is henceforth simply referred to as “MAD1’s loop region”). Interestingly, the primary sequence of this loop region is not well conserved from yeast to human, but the secondary structure is predicted to be conserved.

We reason that the “knitting” model is more realistic based on many pieces of evidence from previous literature. First, locking cytosolic MAD2 to its closed conformation inhibited the heterodimerization between CDC20 and MAD2 and compromised the SAC signaling activity [148, 149, 150], which can be interpreted by the “knitting” model. Second, the binding of CDC20 to MAD1’s RWD domain is suggested to be important to the SAC signaling activity [36, 37, 162, 163]. One explanation is that the binding may increase the local concentration of CDC20, which is better harnessed by the “knitting” model. The anchoring of the basic

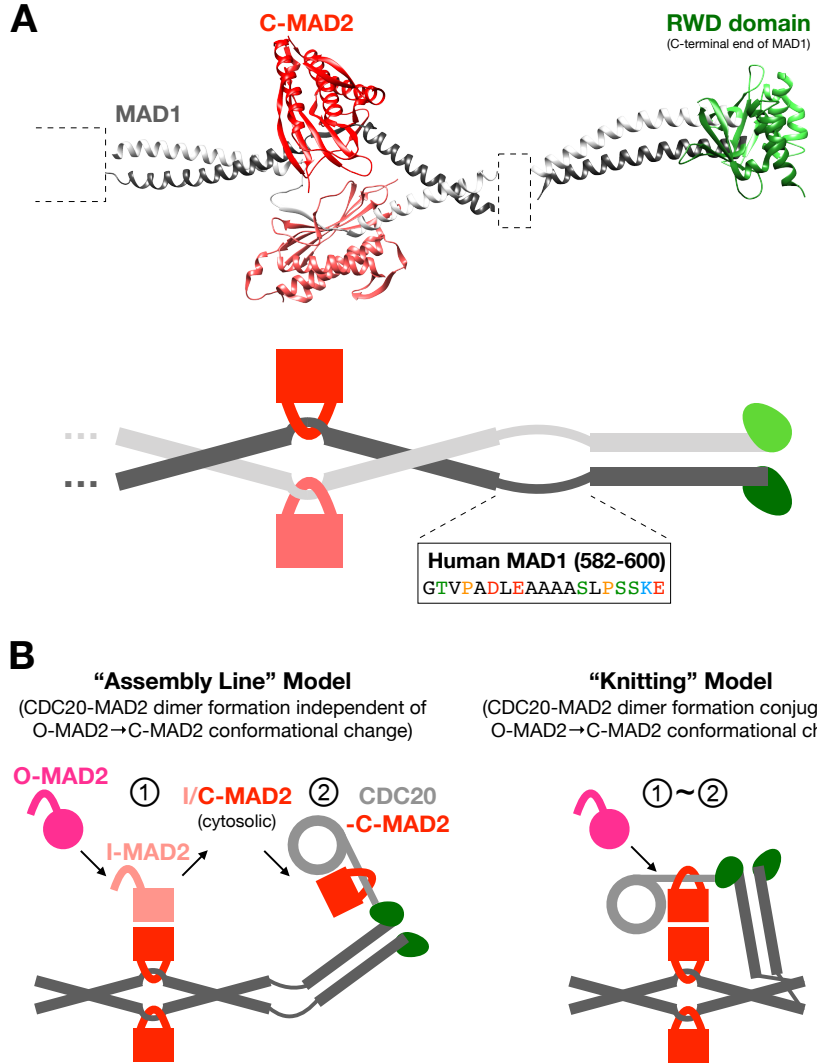


Figure 4.1: The structure of the MAD1-MAD2 heterotetramer and the two models of the molecular mechanism of the formation of CDC20-MAD2.

(A) Top panel: the known structure of the MAD1-MAD2 heterotetramer. PDB IDs: 1GO4 (left, [41]), 4DZO (right, [156]). Structures of the N-terminus and the segment spanning a.a. 580–597 are unknown. Various secondary structure prediction algorithms consistently predicted this segment to be a flexible loop (though the predicted starting and ending positions may vary among different algorithms). Bottom panel: a cartoon illustrating the known structure of the MAD1-MAD2 heterotetramer. The color scheme matches the top panel. To distinguish the two MAD1 proteins [and their C-terminal RWD domains] and the two MAD2 proteins, slightly different colors are applied. In all cartoons later, both copies will use the same color scheme. The sequence of the loop region (a.a. 582–600) predicted by Lupas' method is shown [157]. Serine/threonine residues are colored green. Proline residues are colored orange. Negatively charged residues are colored red. Lysine residues are colored blue. All cartoons in this chapter are not to scale. (B) The two models of the molecular mechanism of the formation of CDC20-MAD2: the "assembly line" model (left) and the "knitting" model (right).

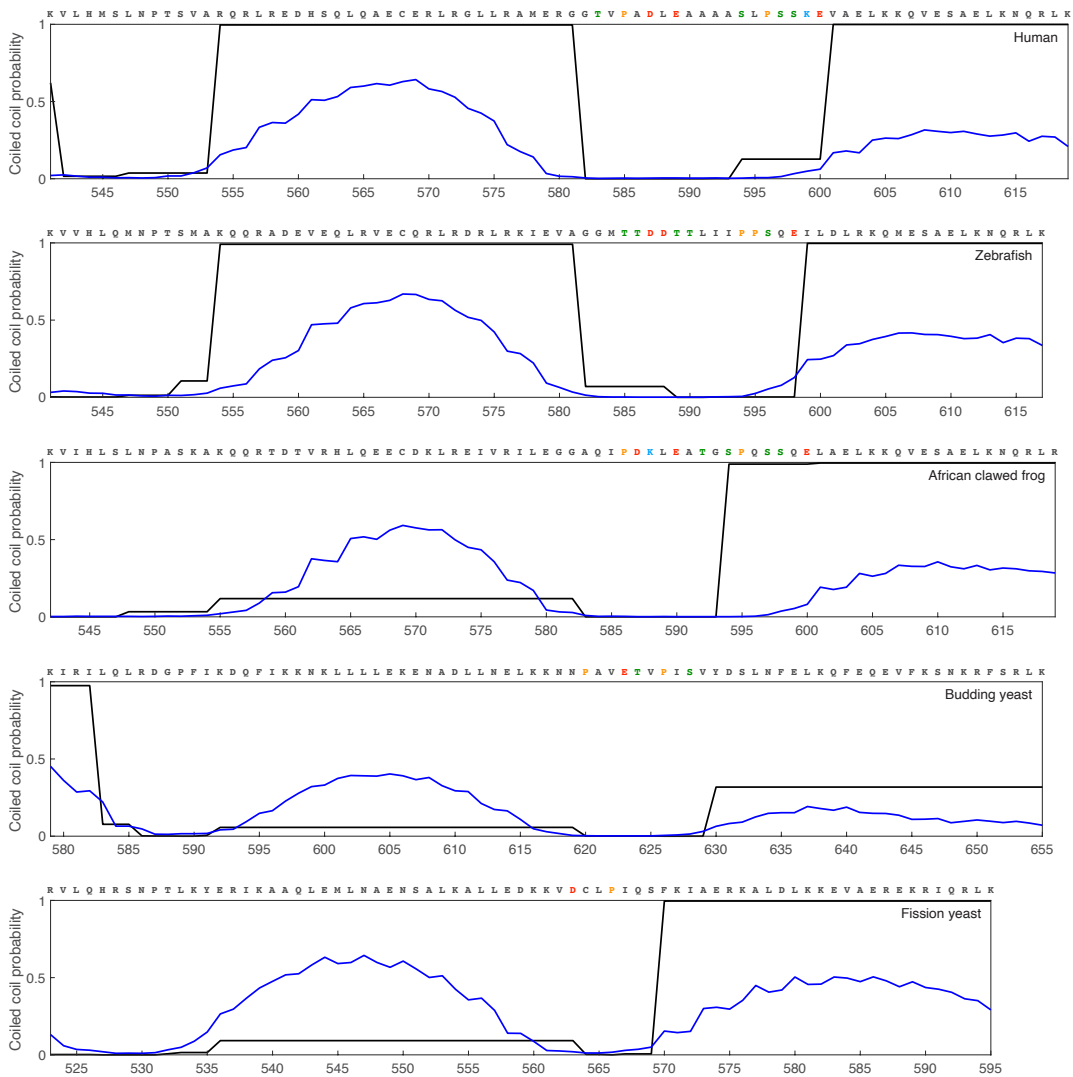


Figure 4.2: The secondary structure of MAD1’s loop region is well conserved.

Although the primary sequence of MAD1’s loop region is not conserved, proline residues are commonly (not always) found in this region. The figure shows coiled-coil predictions by two algorithms (black curves: Lupas’ method using a gliding window size of 28 residues [157]; blue curves: raw predicted probabilities by DeepCoil2 [158]) on the region spanning from MAD1’s MIM (which is also not a coiled coil [41]) to MAD1’s consensus RLK motif from *Homo sapiens* (human), *Danio rerio* (zebrafish), *Xenopus Laevis* (African clawed frog), *Saccharomyces cerevisiae* (budding yeast), and *Schizosaccharomyces pombe* (fission yeast). The x -axis represents the coordinates of residues within MAD1. The primary sequences of full-length MAD1 proteins were supplied as the input, but only probability predictions on this region are shown here. The RLK motif directly binds to BUB1 [35, 37] and is located within the coiled coil leading to the RWD domain (see the crystal structure on the right in Figure 4.1A). Residues within the putative loop region are colored as in Figure 4.1A. Similar prediction results were obtained using MARCOIL [159] and PSIPRED 4.0 [160, 161] although the exact starting and ending residues of the flexible loop may differ (data not shown).

motif of CDC20 to MAD1’s RWD domain may even topologically hinder the stringing of MAD2 that is already in the closed conformation because CDC20’s MIM is between the basic motif and the β -propeller. Third, two recent studies strongly supported the spatio-temporal coupling between MAD2’s conformational change and the formation of the CDC20-MAD2 dimer [27, 28].

In this chapter, we intend to prove the “knitting” model by introducing mutations to MAD1 that theoretically only impair the SAC signaling activity if the “knitting” model is correct. It should be noted that there is a gray area between the two models, given that I-MAD2 can exist in the solution [153], which may be the fresh MAD2 conformer coming off the template-based conformational switch, entering the cytosolic pool, and eventually binding to CDC20 (becoming C-MAD2 thereafter). We categorize this situation into the “assembly line” model (also illustrated in Figure 4.1B) because our mutational approach should not impair the SAC signaling activity in this case either (see Section 4.3).

4.2 The MAD1-MAD2 heterotetramer may adopt a fold-back conformation both *in vivo* and *in vitro*

For the “knitting” model to work, the reaction center of MAD2’s conformational switch and CDC20’s MIM have to be positioned close enough. According to the crystal structure, the axial length from the MIM to the start of the loop region is about 5–6 nm while the axial length from the end of the loop region to the anchoring point of CDC20 is about 7 nm [27, 27, 37, 41, 155, 156]. In contrast, if we model the disordered N-terminus of CDC20 as a simple 3-D random walk, we can estimate the root-mean-square distance from CDC20’s BOX1 to its MIM (about 90 residues) to be less than 4 nm. Due to steric hindrance and restrictions imposed by the Ramachandran plot, such a simple 3-D random walk model is far from realistic. However, even if we apply a more sophisticated worm-like chain model with a persistence length of 3–7 Å [164, 165], the root-mean-square distance from CDC20’s BOX1 to its MIM is still only about 4.5–7 nm. These estimations suggest that additional mechanisms may be at work to position the reaction center of MAD2’s conformational switch and CDC20’s MIM closely to facilitate the heterodimerization between MAD2 and CDC20.

One suggested possibility [27, 28] is that the cooperative binding of CDC20 to MAD1’s RWD domain and BUB1 helps to unravel the N-terminus of CDC20. Indeed, if the disordered region from CDC20’s BOX1 to its MIM is fully stretched, it will be more than enough for the MIM of the CDC20 anchored to MAD1’s RWD domain to engage the reaction center of MAD2’s

conformational switch. However, there are conflicting claims over whether and where BUB1 directly binds to MAD1 [27, 35, 37]. If BUB1’s conserved domain 1 (CD1, which is also named conserved motif 1 or CM1) directly interacts with MAD1’s consensus RLK motif located in MAD1’s C-terminal coiled coil as suggested in [35, 37] (illustrated in Figure 4.7 as the contact between BUB1 and the C-terminal coiled coil of MAD1), the cooperative binding of CDC20 to BUB1 and MAD1 may not unravel CDC20’s N-terminus because the segment of BUB1 from CD1 to ABBA-consensus KEN motifs (which bind to CDC20 [27, 152, 166]) is also largely disordered (predicted by AlphaFold 2 with low confidence; data not shown [40]).

Another possibility has been suggested in [41, 163, 167] that MAD1 may position the reaction center of MAD2’s conformational switch and CDC20’s MIM closely by assuming a fold-back conformation. As mentioned in the previous section, the secondary structure of MAD1’s C-terminal loop region is conserved. Its flexibility may enable such fold-back conformation, according to the prediction by the ColabFold advanced algorithm (see Figure 4.3A). If we truncate residues 582–600 of human MAD1, which removes the flexible loop and fuses the coiled coils upstream and downstream of the loop region (while preserving the original heptad repeat position designation as assigned by Lupas’ method [157] as well as DeepCoil2 [158]; data not shown), the resulting loop-deleted MAD1 (henceforth referred to as MAD1 Δ L) homodimer can only assume an extended conformation (see Figure 4.3B).

We noted that about 37% of purified full-length MAD1-MAD2 heterotetramers do not show distinguishable MAD1-MIM-MAD2 and MAD1-RWD domain densities as visualized by electron microscopy using metal shadowing [27]. This may be explained by that this population of MAD1-MAD2 heterotetramers assumes a fold-back conformation (but may also be attributed to certain orientations on the grid). To further support that the MAD1 may assume a fold-back conformation *in vivo*, we resorted to the distance-sensitive FRET measurement. We fused the donor fluorophore mNeonGreen to the C-terminal end of MAD1 (see Section 3.1) and inserted the acceptor fluorophore mScarlet-I into the β 5- α C loop of MAD2 [169, 170] (the recombinant protein is henceforth referred to as “MAD2 \wedge mScarlet-I”; see Figure 4.4A). If the heterotetramer always assumes an extended conformation, the distance between the donor and acceptor will be larger than 10 nm, which allows no or minimal FRET between the donor MAD1-mNG and the acceptor MAD2 \wedge mScarlet-I [12]. However, if the heterotetramer may assume a fold-back conformation, the distance between the donor and acceptor may be reduced to allow for FRET between the donor and the acceptor.

We confirmed the expression of full-length MAD2 \wedge mScarlet-I in the heterozygous *MAD2 \wedge mScarlet-I* genome-edited HeLa-A12 cell line (see Figure 4.4B), wherein the ex-

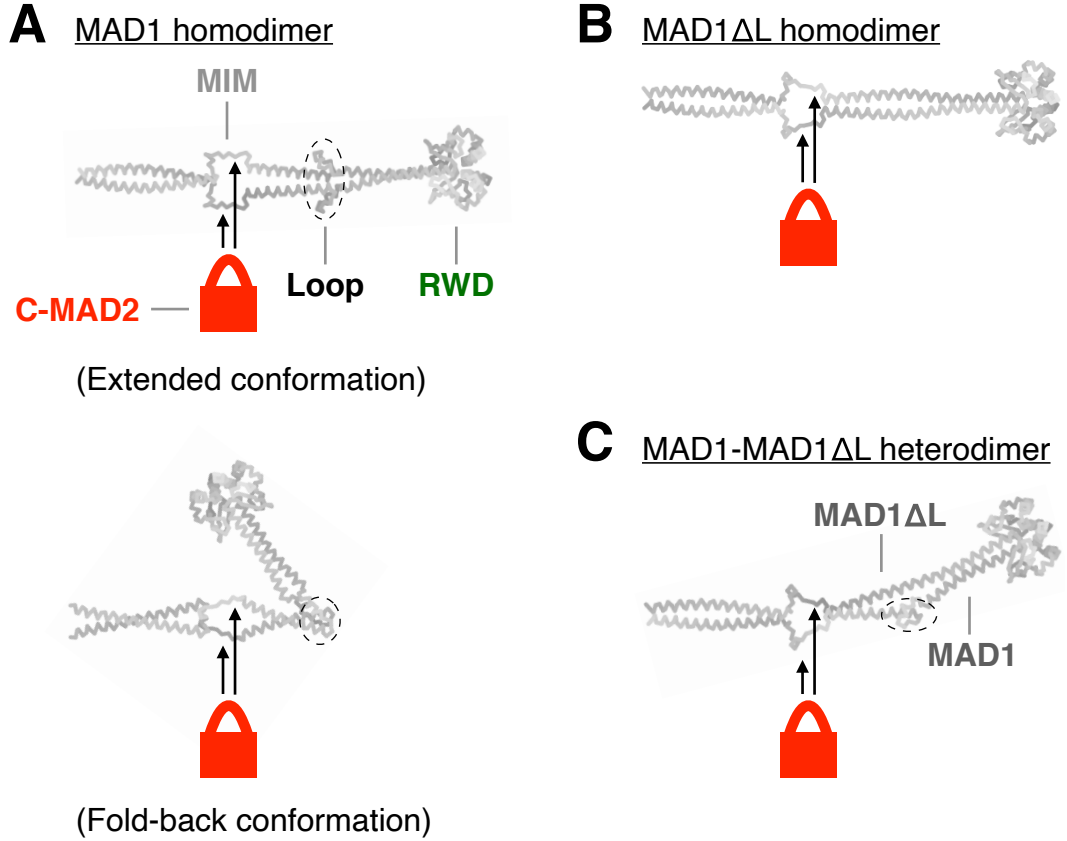


Figure 4.3: Representative structures of the C-terminus of the MAD1 homodimer, the MAD1 Δ L homodimer, and the MAD1-MAD1 Δ L heterodimer were predicted by ColabFold.

We took advantage of the free ColabFold advanced Jupyter Notebook (henceforth simply referred to as “ColabFold advanced algorithm”), which implemented the tremendously successful, recently publicized structural prediction algorithm AlphaFold 2 in Google Colaboratory [39, 168]. Representative models (out of five models in total) of the C-terminus of the MAD1 homodimer (A), the MAD1 Δ L homodimer (B), and the MAD1-MAD1 Δ L heterodimer (C) were predicted using the default parameter settings of ColabFold advanced algorithm. The loop region of wildtype MAD1 is circled out in (A) and (C). The MIM of MAD1 where C-MAD2 binds and the RWD domain at the C-terminal end of MAD1 where the N-terminal BOX1 of CDC20 is anchored are also indicated. The C-terminus of the MAD1 homodimer may assume a fold-back conformation [see the bottom panel of (A)], which is close to the scenario envisioned by [163]. In the predicted structure of the MAD1-MAD1 Δ L heterodimer, the loop region of the wildtype copy introduces a bulge but the overall conformation is extended.

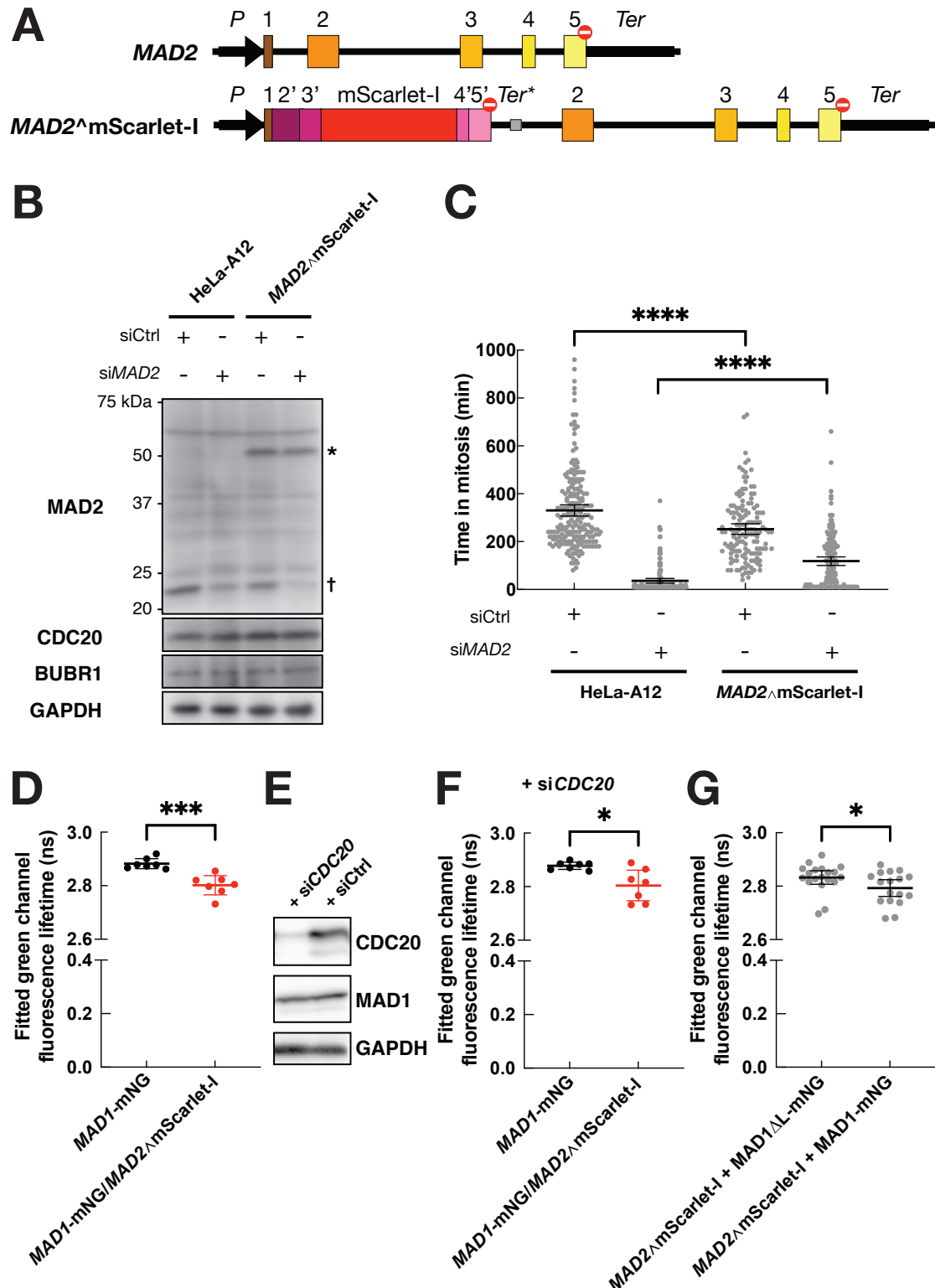


Figure 4.4: The observation of FRET between MAD1-mNG and MAD2^mScarlet-I at the interphase/prophase NPC suggested that MAD1-MAD2 heterotetramers may assume a fold-back conformation *in vivo*.

(Caption of Figure 4.4 continued from a previous page) (A) Diagram of the endogenous *MAD2* allele and the genome-edited *MAD2*ΔmScarlet-I allele. Boxes 1–5 represent the exons. The regions between these boxes represent the introns. Boxes 2'–5' encode the same peptides as boxes 2–5 respectively, with the introduction of certain silence mutations that make the recombinant *MAD2*ΔmScarlet-I resistant to si*MAD2*. The black “*P*” arrow represents the promoter and the 5'-UTR. The black “*Ter*” bar represents the 3'-UTR and the polyadenylation signal. The gray “*Ter**” bar represents the polyadenylation signal of rabbit β-globin. The red stop signs represent stop codons. The sequence of the *MAD2*ΔmScarlet-I allele was confirmed by genotyping and Sanger sequencing (data not shown). (B) Immunoblotting showed that *MAD2*ΔmScarlet-I (labeled by an asterisk, with an expected molecular weight of 51.0 kDa) was correctly expressed in the heterozygous *MAD2*ΔmScarlet-I HeLa-A12 cell line and was resistant against si*MAD2*. As a comparison, wildtype *MAD2* (labeled by a cruciform with a molecular weight of 23.5 kDa) was effectively knocked down by si*MAD2*. The immunoblot against GAPDH served as the loading control. (C) Unsynchronized cells were treated with respective siRNAs for one day, treated with 50 nM nocodazole. Each gray dot represents a cell. The total number of cells in each group $N > 140$. Mean values $\pm 95\%$ confidence intervals are overlaid. Results are representative of two independent experiments. (D) The average lifetime of MAD1-mNG in the *MAD1*-mNG genome-edited HeLa-A12 cell line or the *MAD1*-mNG/*MAD2*ΔmScarlet-I genome-edited HeLa-A12 cell line (using a two-component exponential decay to fit the raw data of FLIM). Each dot represents a single cell. Mean values $\pm 95\%$ confidence intervals are overlaid. The total number of cells in each group $N = 7$. Results are representative of two independent experiments. (E) Unsynchronized HeLa-A12 cells were treated with si*CDC20* or a control siRNA for 2 d and probed for *CDC20*, *MAD1*, and GAPDH (loading control). (F) Same as (D), except that cells were treated with si*CDC20* as in (E). (G) The average lifetime of *MAD1*ΔL-mNG and *MAD1*-mNG stably transfected into the *MAD2*ΔmScarlet-I genome-edited HeLa-A12 cell line (using a two-component exponential decay to fit the raw data of FLIM). Each dot represents a single cell. Mean values $\pm 95\%$ confidence intervals are overlaid. The total number of cells in each group $N \geq 17$. Results are pooled from four independent experiments. Unpaired *t*-tests with Welch’s correction are performed in Prism 9.

pression level of either BUBR1 or CDC20 was not affected. MAD2 \wedge mScarlet-I could support a certain degree of the SAC signaling activity when the endogenous wildtype MAD2 was knocked down (see Figure 4.4C). Using fluorescence lifetime imaging microscopy (FLIM) [171], we quantified a FRET efficiency of about 3% between MAD1-mNG and MAD2 \wedge mScarlet-I at the interphase/prophase NPC in the heterozygous *MAD1*-mNG, *MAD2* \wedge mScarlet-I genome-edited HeLa-A12 cell line (see Figure 4.4D and section 4.7.4). We chose to measure FRET at the interphase/prophase NPC to facilitate data collection by the line-scanning confocal microscope and to avoid the potential intermolecular FRET between a donor from one MAD1-MAD2 heterotetramer and an acceptor from another nearby heterotetramer at the corona of a signaling kinetochore. This FRET persisted even when *CDC20* was knocked down by RNAi (see Figures 4.4E and 4.4F), which indicates that this FRET does not depend on the formation of CDC20-MAD2 but is rather intrinsic to the structural characteristics of the MAD1-MAD2 heterotetramer. Although we cannot rule out the possibility of intermolecular FRET between two MAD1-MAD2 heterotetramers, we further verified that this FRET is reduced after the deletion of the loop region of MAD1 (see Figure 4.4G). These results support that the structural flexibility of the C-terminus of MAD1 enabled by the loop region facilitates the fold-back of the MAD1-MAD2 heterotetramer.

4.3 MAD1's loop region is important to the SAC signaling activity *in vivo*

We next sought to determine whether the loop region of MAD1 that likely enables the fold-back conformation is important to the SAC signaling activity *in vivo*. We integrated the expression cassette of either MAD1-mNG or MAD1 Δ L-mNG into the genome of HeLa-A12 cells using Cre-*lox* RMCE (see Figure 2.1B). We then knocked down endogenous MAD1 in these cells using two siRNAs that target the 3'-UTR of *MAD1* [172] (henceforth collectively referred to as si*MAD1*'s) and induced the expression of MAD1(WT/ Δ L)-mNG (si*MAD1*-resistant due to the lack of the endogenous 3'-UTR) by doxycycline. Our genome-edited *MAD1*-mNG HeLa-A12 cell line served as the reference for the endogenous level of MAD1 in live-cell fluorescence imaging.

We found out that knocking down *MAD1* crippled the SAC signaling activity (see Figure 4.5A), although cells with less than 10% of the physiological level of MAD1 on average (see Figure 4.5E) still arrested in mitosis for hours when treated with 100 nM nocodazole (only about two hours less than the control group with a physiological level of MAD1). In-

creasing the dosage of si*MAD1*'s did not further decrease the SAC activity, reinforcing that even a small pool of MAD1 could sustain a considerable level of SAC signaling activity (see Figure 4.5B).

Surprisingly, MAD1 Δ L-mNG had impaired support for the SAC in a dominant-negative manner: cells treated with si*MAD1*'s and rescued by a physiological level of MAD1 Δ L-mNG arrested in mitosis for a significantly shorter duration than cells which were not rescued. As a comparison, wildtype MAD1-mNG fully restored the SAC signaling activity (see Figure 4.5A). One possible explanation was that MAD1 Δ L-mNG might dimerize with the remaining endogenous MAD1 and restrict its structural flexibility. Structural prediction of the heterodimer between wildtype MAD1 and MAD1 Δ L showed that the loop region of the wildtype copy introduced a bulge but could not enable a fold-back conformation of the heterodimer due to stiffness of the fused α -helices of the MAD1 Δ L counterpart (see Figure 4.3C). To test this hypothesis, we pulled down doxycycline-induced MAD1(wildtype/ Δ L)-mNG from lysates of HeLa-A12 cells in which endogenous MAD1 was not knocked down. We found that endogenous MAD1 was also pulled down by both MAD1-mNG and MAD1 Δ L-mNG, but not by mNeonGreen alone (see Figure 4.5C). We further confirmed that MAD1 Δ L-mNG did not cause defects in the localization of the MAD1 Δ L-MAD2 heterotetramer (see Figure 4.5D) or the expression of BUBR1, CDC20, or BUB3 (see Figure 4.5E). *In vitro* reconstitution data from our collaborators (not shown here) also suggested that truncating the loop region of MAD1 reduced the formation rate of CDC20-MAD2. Therefore, although the results of our knockdown-rescue experiments were hindered by the incomplete knockdown of the endogenous MAD1, all evidence combined suggested that the loop region of MAD1 is critical to the SAC signaling activity in its own right.

4.4 MAD1(Lmut) can fully support the SAC signaling activity

Many possibilities could underlie the observation that the deleted segment encompassing residues 582–600 in MAD1 Δ L is important to the SAC signaling activity. It is known that S598 can be phosphorylated by MPS1 *in vitro* [167]. There could also be a certain unknown protein-protein interaction associated with the loop region of MAD1 that is important to the SAC. To examine whether it is the structural flexibility provided by the loop region that is critical to the SAC signaling activity, we tested two different artificial flexible loops to replace the original segment encompassing residues 582–600: “AL11” and “Lmut” (see

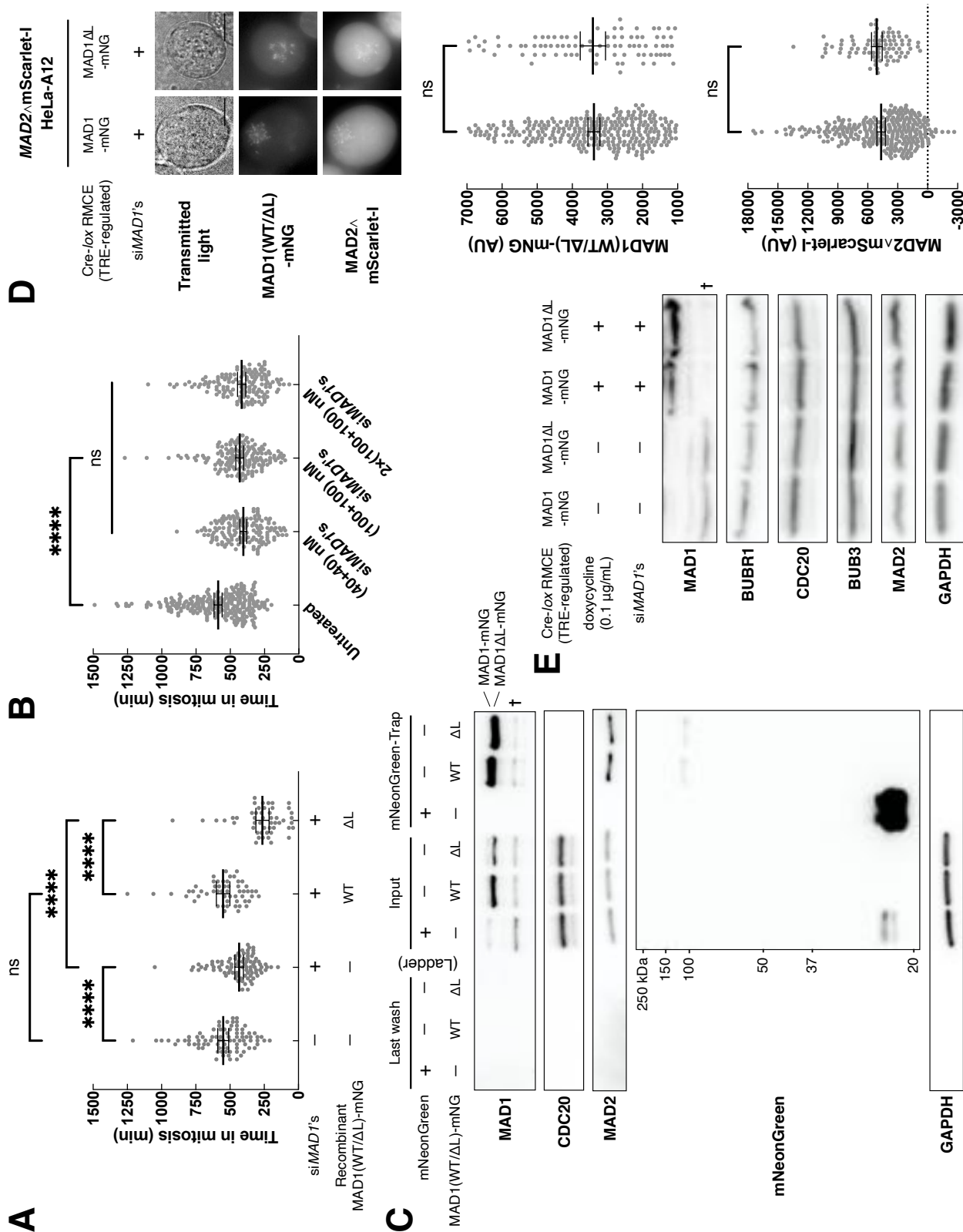


Figure 4.5: The loop region of MAD1 is critical to the SAC signaling activity in its own right.

(Caption of Figure 4.5 continued from a previous page) (A) The first two columns on the left used the *MAD1*-mNG genome-edited HeLa-A12 cell line which served as a reference of the endogenous level of *MAD1*. *In situ* tagging of *MAD1* did not affect the 3'-UTR which si*MAD1*'s target. The effectiveness of si*MAD1*'s against the *MAD1*-mNG allele was confirmed by the greatly diminished green channel fluorescence signal (data not shown). The two columns on the right used Cre-*lox* RMCE HeLa-A12 cell lines which were treated with si*MAD1*'s and induced to express either *MAD1*-mNG or *MAD1* Δ L-mNG. Each dot represents a cell ($N \geq 50$ in each group). Results were pooled from at least two technical repeats. The mean value \pm the 95% confidence interval of each group is overlaid. Unpaired *t*-tests with Welch's correction are performed in Prism 9. (B) The conditions of si*MAD1* treatment were (from left to right): untreated, 40 nM each for two days (the standard condition used throughout this study), 100 nM each for two days, 100 nM each in day one and 100 nM each again in day two. The *MAD1*-mNG genome-edited HeLa-A12 cell line was used in each group. Each dot represents a cell ($N \geq 145$ in each group). The mean value \pm the 95% confidence interval of each group is overlaid. Welch's ANOVA test [$W(DF_n, DF_d) = 0.9885(2.000, 298.9)$, $p = 0.3733$] was performed for the three columns on the right. The ANOVA test and the unpaired *t*-test with Welch's correction are performed in Prism 9. (C) Using immunoblotting to evaluate the immunoprecipitation by the mNeonGreen-Trap Agarose. The cruciform symbol represents the endogenous *MAD1* band. The expected molecular weights of the recombinant *MAD1*-mNG, *MAD1* Δ L-mNG, and mNeonGreen are 110.2 kDa, 108.4 kDa, and 26.9 kDa, respectively. The immunoblot against GAPDH served as the loading control. Blots shown here are from the same immunoprecipitation experiment representative of two independent repeats. (D) The *MAD2* \wedge mScarlet-I genome-edited HeLa-A12 treated with si*MAD1*'s and rescued by *MAD1*(WT/ Δ L)-mNG were imaged using wide-field fluorescence microscopy. Cells were arrested at mitosis using a thymidine–nocodazole synchronization protocol (see Section 3.7.8). Representative micrographs are shown in the top panel. Maximum *z*-projected green channel images shown here share the same LUT. Maximum *z*-projected red channel images shown here also share the same LUT. Scale bar, 10 μ m. Due to various expression levels of induced *MAD1*(WT/ Δ L)-mNG in different cells, signaling kinetochores were filtered by the localization of *MAD1*(WT/ Δ L)-mNG (with an arbitrary threshold of 1000–7000 AU). Each gray dot represents a single signaling kinetochore ($N \geq 85$ in each group). The mean value \pm the 95% confidence interval of each group is overlaid. Unpaired *t*-tests with Welch's correction are performed in Prism 9. (E) Knockdown of the endogenous *MAD1* by si*MAD1*'s had an efficiency of over 90% based on the intensity of the residual *MAD1* band. The cellular abundance of either BUBR1, CDC20, or BUB3 was not affected. The immunoblot against GAPDH served as the loading control. Unsynchronized Cre-*lox* RMCE HeLa-A12 cells were used.

Figure 4.6A). Both of them consist of 19 amino acid residues like the original one. AL11 is a previously characterized flexible linker composed of 11 alanine residues, 7 glycine residues, and 1 threonine residue [173]. In Lmut, serine and threonine residues of the original segment are mutated into alanine and valine residues, respectively. The amino acids between the two prolines are adjusted into mostly alanine-glycine-alanine repeats while the proline residues themselves and their N-terminal neighboring residues are preserved.

Both MAD1(AL11) and MAD1(Lmut) were predicted to have a similar coiled-coil propensity profile to that of the endogenous MAD1 (see Figure 4.6A). Surprisingly, cells treated with si*MAD1*'s and rescued by MAD1(AL11)-mNG had a lower SAC signaling activity than wildtype cells did (see Figure 4.6B). As a comparison, MAD1(Lmut)-mNG fully restored the SAC signaling activity. We hypothesized that because proline residues may assume the *cis*-conformation at a higher propensity than many other amino acid residues at equilibrium [174], they might facilitate the proper fold-back of MAD1.

The fact that Lmut can functionally replace the original segment encompassing residues 582–600 revealed that the SAC likely relies on the structural flexibility but not phosphorylation or unknown protein-protein interactions (other than those that rely solely on the prolines and their N-terminal neighboring residues; see Section 4.6 for more details) associated with the loop region.

4.5 The structural flexibility of MAD1 enabled by its loop region facilitates the “knitting” of the MCC

Based on previous literature and our data, we proposed the following mechanistic model of the catalytic role of MAD1 in the assembly of CDC20-MAD2 (see Figure 4.7). MAD1 in its fold-back conformation physically positions the MIM of CDC20 and MAD2 closely, facilitating the spatio-temporal coupling of MAD2's conformational switch and the assembly of the CDC20-MAD2 heterodimer. The avidity binding between the scaffold protein MAD1 (in its fold-back conformation) and CDC20-MAD2 energetically favors the formation of the MAD1RWD-CDC20-MAD2-MAD2-MAD1MIM complex. MAD1 may switch back to an extended conformation (probably in an ATP-dependent manner), breaking such avidity binding and promoting the release of CDC20-MAD2 into the cytosol.

However, there are many missing links towards the “knitting” model. For example, do BUB1 and MAD1 cooperate to unravel CDC20 and scaffold the assembly of CDC20-MAD2? Does MAD1 switch between an extended conformation and the fold-back conformation at a phys-

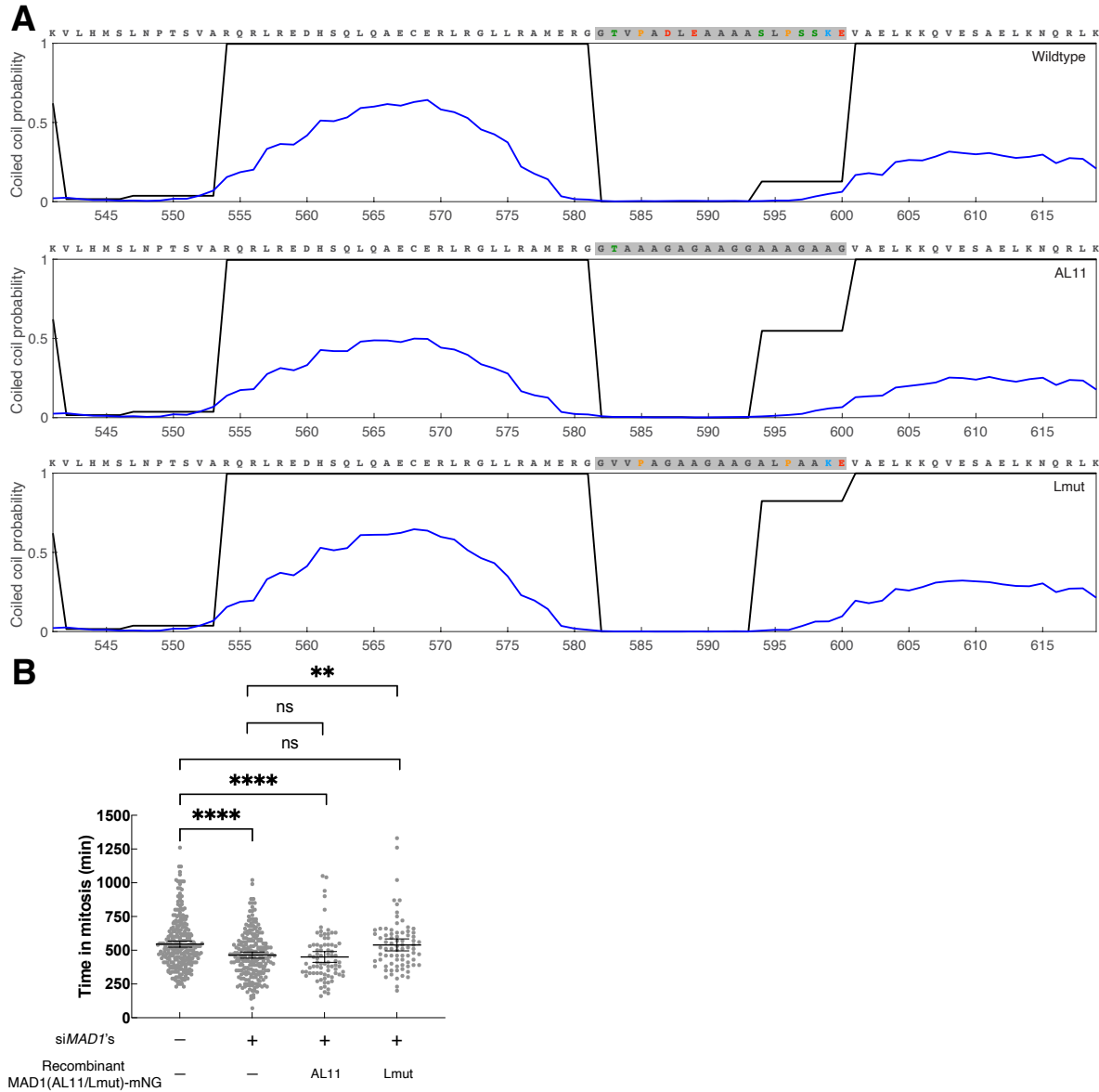


Figure 4.6: MAD1(AL11)-mNG cannot fully rescue the SAC signaling activity but MAD1(Lmut)-mNG can.

(A) The figure shows coiled-coil predictions of human wildtype MAD1 (top), MAD1(AL11) (middle), MAD1(Lmut) (bottom) by the two algorithms as in Figure 4.2. The top panel is reproduced from Figure 4.2. Segments encompassing residues 582–600 are highlighted by gray boxes. (B) The first two columns on the left used the *MAD1*-mNG genome-edited HeLa-A12 cell line which served as a reference of the endogenous level of *MAD1*. The AllStars negative control siRNA was added to the first group and si*MAD1*'s were added to the second group. The two columns on the right used the Cre-*lox* RMCE HeLa-A12 cell lines which were treated with si*MAD1*'s and induced to express either MAD1(AL11)-mNG or MAD1(Lmut)-mNG. Each dot represents a cell ($N \geq 75$ in each group). Results were pooled from at least two technical repeats. The mean value \pm the 95% confidence interval of each group is overlaid. Unpaired *t*-tests with Welch's correction are performed in Prism 9.

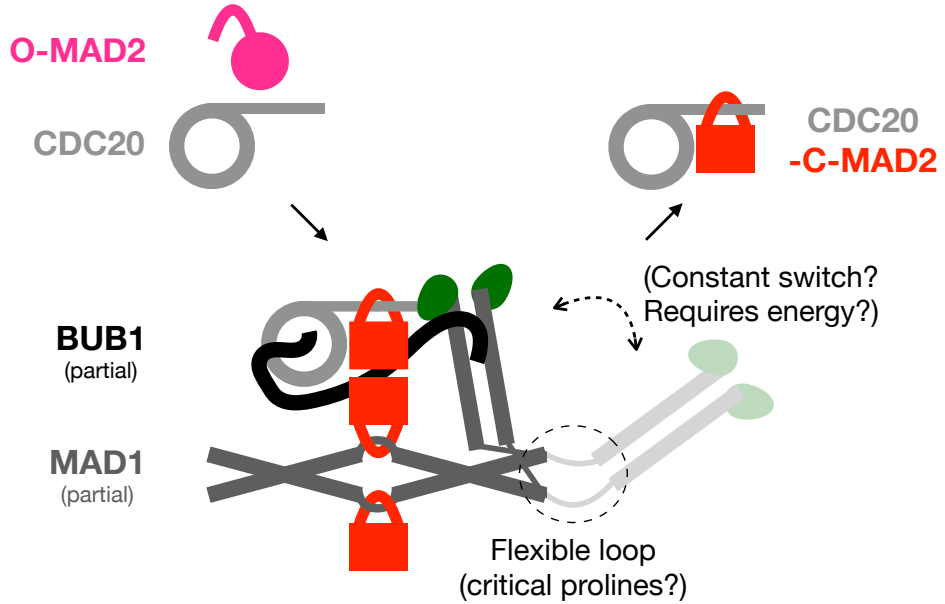


Figure 4.7: “Knitting” model: MAD1’s structural flexibility may facilitate the spatio-temporal coupling of MAD2’s conformational switch and the assembly of the CDC20-MAD2 heterodimer.

The two solid black arrows indicate the formation and release of the CDC20-MAD2 heterodimer, respectively. T461-phosphorylated CD1 of BUB1 (458–476) interacts with MAD1’s consensus RLK motif located within the coiled coil leading up to the RWD domain [35, 37]. Additionally, the C-terminus of BUB1’s CD1 contacts the RWD domain of the opposite MAD1 copy to whose consensus RLK motif the CD1 interacts with [35]. BUB1 interacts with CDC20 through multiple motifs cooperatively. For example, BUB1’s ABBA motif (527–532) binds between Blades 2 and 3 of CDC20’s seven-bladed WD40 fold and BUB1’s consensus KEN box (C-terminal to the ABBA motif) likely binds to the center of the top surface of CDC20’s WD40 [27, 152, 166]. CDC20 also binds to MAD1 and BUB1 cooperatively [27, 28]. However, whether BUB1 and MAD1 cooperate to unravel CDC20 and scaffold the assembly of CDC20-MAD2 is unclear (refer to the two possibilities in Section 4.2). The proposed avidity binding between the scaffold protein MAD1 (in its fold-back conformation) and CDC20-MAD2 involves the MAD1RWD-CDC20 interaction, the “safety belt”-like binding between CDC20 and MAD2, as well as the homodimerization of the MAD2 in the CDC20-MAD2 heterodimer and the MAD2 in the MAD1-MAD2 heterotetramer [27, 37, 41, 153, 155, 170].

iologically meaningful rate *in vivo* and does this switching cycle correlate with the knitting of a CDC20-MAD2 heterodimer? Does MAD1’s conformational switch require energy input? Do the proline residues simply serve to break the coiled coil and shape the flexible loop of MAD1, or do they play a more complex role in the proper fold-back of MAD1? Future studies are needed to fill these gaps between current experimental evidence and the “knitting” model.

4.6 Discussion

A recent structural study shows that purified MAD1-MAD2 heterotetramer may assume a fold-back conformation *in vitro* [151]. In this study, we showed for the first time that the MAD1-MAD2 heterotetramer may assume a fold-back conformation *in vivo*. Our preliminary data indicate that the structural flexibility is enabled by a flexible loop in the C-terminus of MAD1, whose secondary structure is conserved. This loop region is important to the SAC signaling activity both *in vitro* (based on the biochemical data by our collaborators) and *in vivo* (based on our cell biology data), which does not depend on any potential phospho-regulation of the serine/threonine residues within the loop region. We proposed a “knitting” model to explain how the structural flexibility of the MAD1-MAD2 heterotetramer may facilitate the spatio-temporal coupling between MAD2’s conformational change and the formation of CDC20-MAD2.

Even in the absence of CDC20, O-MAD2 can bind to the MAD1-MAD2 heterotetramer, complete the conformational switch, and dissociate as C-MAD2 *in vitro* [175]. Both a previous study [154] and a recent study [151] show that the addition of a MIM peptide promotes the conversion of purified O-MAD2 into C-MAD2 *in vitro*. Although we show that the structural flexibility of MAD1 is important to the SAC signaling activity, confirming whether the close positioning of CDC20 to the reaction center of MAD2’s conformational switch (facilitated by the fold-back of the MAD1-MAD2 heterotetramer) increases the rate of MAD2’s conformational switch *in vivo* will further consolidate the catalytic mechanism proposed here.

MAD1 has a long half-life under normal conditions [176]. And like BUB1 [54, 97, 98], even a small pool of MAD1 (at less than 10% on average of its physiological concentration in our knockdown experiments) can maintain a considerable level of SAC signaling activity in nocodazole-treated cells. Future studies should consider combining RNAi (or induced knockout of *MAD1*) with induced acute degradation of MAD1 proteins to reduce the contribution of the remaining endogenous MAD1 homodimer to the SAC signaling activity and to min-

imize the chance of heterodimerization between the remaining endogenous MAD1 and the rescuing MAD1 variants in such knockdown-rescue experiments.

Given the critical role of MAD1’s structural flexibility enabled by its loop region, it would be interesting to replace the flexible loop with a turn to lock MAD1 in the fold-back conformation and see how the SAC signaling activity is affected. Another way to advance our understanding is to investigate whether the two pools of MAD1 (adopting either the fold-back or extended conformation) inter-convert at a physiologically meaningful rate in the cell using single-molecular approaches. Even though the two proline residues (P585 and P596) in MAD1’s loop region may be important to the SAC signaling activity *in vivo*, no MAD1-interacting protein with peptidylprolyl cis-trans isomerase activity has been identified in the PrePPI database using the gene ontology enrichment analysis tool from the PANTHER Classification System as of March 2022 [177, 178]. Additionally, it might be worth finding out whether the equilibrium between the two conformations in the cell is the same as purified MAD1-MAD2 heterotetramer *in vitro*, which would tell us if the conformation distribution is under active regulation in the cell that costs energy [179].

Two missense variants (D587N and A593V) related to MAD1’s loop region were recorded in the Genomic Data Commons Data Portal as of March 2022 [180], but the impact of both point mutations is predicted to be benign. Therefore, the physiological impact of potential mutations in MAD1’s loop region at the organism level is unclear. It would be interesting to see the physiological impact of introducing point mutations (for example, the multiple proline residues) in MAD1’s loop region in various model systems.

In addition to CDC20, closed MAD2 also interacts with many other proteins (including MAD1, SGO2 [181], Cyclin B2 [63], the insulin receptor [143], and KIF20A [62]), likely by a similar “safety belt” mechanism [41]. One question that comes up naturally is whether the same catalytic mechanism (spatio-temporal coupling) similarly applies to how MAD2 binds to other proteins? Or even more generally, does the same catalytic mechanism applies to how other HORMA (Hop1p, Rev7p, and Mad2p) domain proteins [182] bind to their interaction partners? One interesting finding is that the S214A mutation in human MAD1 impairs the homodimerization of MAD1 as well as the interaction between MAD1 and MAD2 [95]. S214A is unlikely to affect the binding of MAD2 to MAD1’s MIM directly, given the structure of the MAD1-MAD2 heterotetramer [41] and the fact that S214 and MIM are over 300 amino acids apart. This suggested that the homodimerization of MAD1 might facilitate the binding of MAD2 to MAD1. One possibility is that one copy of MAD1 may trans-activate the binding of MAD2 to the other copy of MAD1 in the MAD1-MAD2 heterotetramer. Future experiments are needed to elucidate the structural and catalytic basis of how MAD2 “buckles up” its

binding partners, which may unveil how MAD2 regulates mitosis beyond the assembly of the MCC.

In vitro reconstitution data from our collaborators suggested that the critical role of the flexibility of MAD1 in scaffolding the spatio-temporal coupling relies on BUB1. In the absence of BUB1 in the reactions, the formation rates of CDC20-MAD2 were the same for both MAD1 and MAD1 Δ L (data not shown). However, it is known that the assembly of the MCC also occurs during the interphase and prophase [57]. There has been no report on BUB1’s localization at the NPC where the MAD1-MAD2 heterotetramer is predominantly localized during the interphase and prophase. Therefore, either the flexibility of MAD1 alone scaffolds the coupling at the NPC or there may be a nucleoporin that functions similarly to BUB1. Interestingly, the nuclear basket protein TPR, which directly associates with the MAD1-MAD2 heterotetramer during the interphase and prophase [56], is predicted to bind to CDC20 directly in the PrePPI database [177]. Future studies should look into how the MAD1-MAD2 heterotetramer may catalyze the formation of the CDC20-MAD2 dimer at the NPC during the interphase and prophase.

4.7 Materials and methods

For methods of cell culture and Cre-*lox* RMCE, see Section 2.8.4. Time-lapse live-cell imaging was performed on an ImageXpress Nano Automated Imaging System as described in Section 3.7.6. Wide-field, *z*-stack fluorescence imaging used in the quantification of localization of MAD1(WT/ Δ L)-mNG and MAD2 \wedge mScarlet-I at signaling kinetochores was also as described in Section 3.7.6.

4.7.1 Calculating the theoretical end-to-end root-mean-square distance of a flexible unstructured peptide

First, we model a flexible peptide with n amino acid residues using a 3-D random walk model (without considering steric hindrance and restrictions imposed by the Ramachandran plot). We denote the displacement of residue number $i + 1$ relative to residue number i as a random vector \mathbf{r}_i , $i = 1, 2, \dots, n - 1$. The end-to-end displacement, \mathbf{D} , can be expressed as

$$\mathbf{D} = \sum_{i=1}^{n-1} \mathbf{r}_i.$$

The root mean square of it is therefore

$$\sqrt{\langle |\mathbf{D}|^2 \rangle} = \sqrt{\left\langle \left(\sum_{i=1}^{n-1} \mathbf{r}_i \right) \cdot \left(\sum_{i=1}^{n-1} \mathbf{r}_i \right) \right\rangle} = \sqrt{\sum_{i=1}^{n-1} \langle |\mathbf{r}_i|^2 \rangle + \sum_{i \neq j} \langle \mathbf{r}_i \cdot \mathbf{r}_j \rangle}$$

For a 3-D random walk, the random vectors representing each step are independent of each other. Therefore, for $i \neq j$,

$$\langle \mathbf{r}_i \cdot \mathbf{r}_j \rangle = 0.$$

Suppose that the contour length of each amino acid residue is universal ($|\mathbf{r}_i| = r, i = 1, 2, \dots, n - 1$; according to [183], we take $r = 3.7 \text{ \AA}$ here), we derive

$$\sqrt{\langle |\mathbf{D}|^2 \rangle} = \sqrt{n-1} \cdot r = \frac{L}{\sqrt{n-1}},$$

wherein $L = (n - 1)r$ is the contour length of the peptide.

Second, we model the same peptide using a worm-like chain model. This model considers the peptide as a continuous worm-like chain rather than a discrete, step-by-step walk in the previous model. According to [165], the end-to-end root-mean-square distance

$$\sqrt{\langle |\mathbf{D}|^2 \rangle} = \sqrt{2pL[1 - \frac{p}{L}(1 - e^{-\frac{L}{p}})]},$$

wherein p is the persistence length, a metric for the stiffness of the chain. According to [164, 165], we take $p = 3\text{--}7 \text{ \AA}$ here.

4.7.2 Generating the *MAD2*^{ΔmScarlet-I} genome-edited HeLa-A12 cell line

The gRNA used in the integration of the coding sequence of *MAD2*^{ΔmScarlet-I} (intron-free, stop codon-containing, and si*MAD2*-resistant by the introduction of silent mutations) and the polyadenylation signal of rabbit β-globin after the first exon of the endogenous *MAD2* gene was 5'-UCGCGCAGGCCAAUUAUCG-3'. Synthesis of the sgRNA and assembly of the *SpCas9*-sgRNA RNP complex were as described in Section 3.7.1. Plain or *MAD1*-mNG genome-edited HeLa-A12 cell lines were co-transfected with the RNP complex and linearized pCC35, sorted, and validated as described in Section 3.7.1. A successfully edited *MAD2*^{ΔmScarlet-I} allele encodes an internally-tagged MAD2 protein, wherein wildtype MAD2 and mScarlet-I are separated by short flexible linkers (AGSGSGGAS between the S114

of MAD2 and the N-terminus of mScarlet-I; GTGAGSA between the C-terminus of mScarlet-I and the A115 of MAD2).

4.7.3 RNAi

The two siRNAs targeting the 3'-UTR of *MAD1* were from [172]. They were applied to unsynchronized cells at a concentration of 40 nM each for two days before imaging or collecting cells for immunoblotting unless specified otherwise. The sense-strand sequence of si*CDC20* was 5'-GGAGCUCAUCUCAGGCCAU-3' [184], which was applied at a concentration of 40 nM for two days before FLIM or immunoblotting. The sense-strand sequence of si*MAD2* was 5'-G GAAGAGUCGGGACCACAGUU-3' [70], which was applied at a concentration of 40 nM for one day before imaging or immunoblotting. Desalted siRNAs modified by double-deoxythymidine overhangs at 3'-ends of both strands were synthesized by Sigma. The AllStars Negative Control siRNA was used as the control. All siRNAs were transfected into the cells via Lipofectamine RNAiMAX following manufacturer's instructions.

4.7.4 Fluorescence lifetime imaging microscopy (FLIM)

Similar to Section 3.7.4, all FLIM data were collected on an Alba v5 Laser Scanning Microscope, connected to an Olympus IX81 inverted microscope main body [equipped with a UPLSAPO60XW objective (1.2 NA)]. A Fianium WL-SC-400-8 laser with an acousto-optic tunable filter was used to generate excitation pulses at a wavelength of 488 nm and a frequency of about 20 MHz. Excitation light was further filtered by a Z405/488/561/635rpc quadband dichroic mirror. The emission light of the green channel was redirected by a 562 longpass dichroic mirror (FF562-Di03, Semrock), filtered by an FF01-531/40-25 filter, and finally detected by an SPCM-AQRH-15 avalanche photodiode. The time-correlated single photon counting module to register detected photon events to excitation pulses was SPC-830. Data acquisition was facilitated by VistaVision.

The instrument response function of the green channel was measured using Rose Bengal (which has poor excitation efficiency at 488 nm) freshly dissolved to 1 μ M in 5.6 M KI solution [185]. The emission light was redirected by a 562 longpass dichroic mirror and filtered by an FF01-582/75-25 filter (Semrock). The data analysis pipeline (implemented in MATLAB) developed in this study is publicly available.

To demonstrate how fluorescence lifetime measurements can quantify the FRET efficiency, consider donor fluorophores with a lifetime of τ_0 . In the absence of acceptor fluorophores,

the exponential decay D_0 of donor fluorescence after the pulse excitation at $t = 0$ is

$$D_0(t) = Ce^{-\frac{t}{\tau_0}}$$

and the total fluorescence signal is

$$S_0 = \int_0^{+\infty} D_0(t)dt = C\tau_0,$$

wherein C is a constant determined by the excitation and detection condition, the total number and properties of fluorophores, and the imaging setup. Without altering any of these conditions, in the presence of acceptor fluorophores and FRET, the longer a donor fluorophore stays in the excited state, the higher the chance FRET may have occurred (note: this is not a rigorous statement because fluorescence emission and FRET quenching are independent stochastic processes and an excited fluorophore can only relax through one route). Suppose that the timing of FRET follows an exponential distribution with a probability density function of

$$f(t) := \frac{1}{\tau'} e^{-\frac{t}{\tau'}}.$$

The probability that FRET does not happen before t_0 will be

$$P(t > t_0) = \int_{t_0}^{+\infty} f(t)dt = e^{-\frac{t_0}{\tau'}}.$$

Excited fluorophores can either take the FRET quenching route or the fluorescence emission route to relax to the ground state (note: a fluorophore may also relax through other ways but the fact that these routes are independent stochastic processes means that it does not affect the following conclusion). Therefore, in the presence of acceptor fluorophores and FRET, the decay D of donor fluorescence becomes

$$D(t_0) = D_0(t_0) \cdot P(t > t_0) = Ce^{-\frac{t_0}{\tau_0}} \cdot e^{-\frac{t_0}{\tau'}} := Ce^{-\frac{t_0}{\tau}},$$

wherein the new lifetime is

$$\tau = \frac{\tau_0 \tau'}{\tau_0 + \tau'}$$

and the new total fluorescence signal is $S = C\tau$. Therefore,

$$\text{FRET efficiency} := \frac{S_0 - S}{S_0} = \frac{\tau_0 - \tau}{\tau_0}.$$

Because the fluorescence lifetime in the absence of quenching is an intrinsic property of a mature fluorescent protein (under a certain temperature) [186], the equation above greatly simplifies experiments to measure the FRET efficiency. This equation still applies even if the fluorescence decay has to be fitted by a multi-component exponential decay, as long as the fluorescence lifetime is an average weighted by the corresponding C of each component.

4.7.5 Immunoprecipitation using mNeonGreen-Trap

HeLa-A12 cells integrated with the expression cassette (under the regulation of a TRE) of either mNeonGreen, MAD1-mNG, or MAD1 Δ L-mNG were induced to express the ectopic recombinant protein by 0.1 μ g/mL doxycycline (for two days until being harvested) and arrested at mitosis using a thymidine–nocodazole synchronization protocol described in Section 3.7.8. Cells were harvested by mitotic shake-off, washed once by PBS, pelleted down by centrifugation at 200–500 g for 3 min, snap-frozen in liquid nitrogen, and stored at –80 °C before the immunoprecipitation experiment.

On the day of the immunoprecipitation experiment, cells were thawed on ice and lysed in the IP lysis buffer [75 mM HEPES-HCl (pH 7.5 at 4 °C), 150 mM KCl, 10% (by volume) glycerol, 1.5 mM MgCl₂, 1.5 mM EGTA, and 1% (by mass) CHAPS, a zwitterionic detergent] supplemented before usage with 1 mM PMSF, the cComplete™ EDTA-free Protease Inhibitor Cocktail, Phosphatase Inhibitor Cocktail IV (RPI), and a phosphatase inhibitor cocktail (1 mM Na₄P₂O₇, 0.1 mM Na₃VO₄, 5 mM NaF, and 2 mM sodium β -glycerophosphate). For 1 mg of wet cell pellet, 40 μ L of 4 °C IP lysis buffer was added, yielding a total protein concentration of about 5.6 mg/mL (if cells were lysed completely). Resuspended cells were rotated for 30 min at 4 °C and then centrifuged at 18,000 g for 20 min at 4 °C. 600 μ L of supernatant was subsequently cleared by 50 μ L of equilibrated control agarose beads (ChromoTek) to reduce non-specific bindings, rotating for 45 min at 4 °C. The mixture was centrifuged at 2000 g for 5 min at 4 °C. 580 μ L of pre-cleared supernatant was then mixed with 30 μ L of equilibrated mNeonGreen-Trap Agarose (nta-20, ChromoTek) and rotated for 1 h at 4 °C. These beads were then pelleted down at 2000 g for 5 min at 4 °C and the supernatant was removed. The beads were further washed for four times (rotated for 5 min at 4 °C and then pelleted down at 2000 g for 5 min at 4 °C) using 1 mL of the IP wash buffer [75 mM HEPES-

HCl (pH 7.5 at 4 °C), 150 mM KCl, 10% (by volume) glycerol, 1.5 mM MgCl₂, and 1.5 mM EGTA] each time. The beads were transferred to a fresh tube before the last wash to avoid the non-specific binding of proteins to the wall of the tube. Finally, 2× Laemmli buffer supplemented with β-mercaptoethanol was added to the beads. Samples were boiled in a boiling water bath for 10 min before being subjected to SDS-PAGE and immunoblotting analysis.

4.7.6 Immunoblotting

Samples for immunoblotting were prepared as described in Sections 3.7.8 and 4.7.5. Primary antibodies (and their working dilution factors by volume) used included anti-BUBR1 (Bethyl Laboratories A300-995A-M, 1 : 1000), anti-CDC20 (Santa Cruz Biotechnology sc-13162, 1 : 200), anti-MAD2 (Bethyl Laboratories A300-301A-M, 1 : 330), anti-GAPDH (Protein-tech 60004-1-Ig, 1 : 5000), anti-MAD1 (GeneTex GTX109519, 1 : 2000 in Figure 4.4E and PLA0092, 1 : 1000 in Figures 4.5C and 4.5E), anti-mNeonGreen (Cell Signaling Technology 53061S, 1 : 100), and anti-BUB3 (Sigma-Aldrich B7811, 1 : 500). Digital images were acquired using an Azure C600 or 600 imaging system (Azure Biosystems).

CHAPTER 5

Conclusion and Perspective

Through my thesis research, I systematically show that cooperative synergy manifests at multiple layers of the core SAC signaling pathway in human cells, which contributes to its sensitivity (effectively delaying the progression of mitosis in the presence of a small number of unattached or laterally attached kinetochores). The revelation of the critical role of cooperative synergy (combined with the competition for the limited pool of signaling proteins) not only expands our understanding of the SAC but may also inspire efforts to examine whether similar mechanisms apply to other signaling pathways that involve the localization of signaling components to signaling scaffolds (proteins and non-coding RNAs [187]).

Human KNL1 possesses 19 putative MELT motifs scattered throughout its middle region [42]. In Chapter 2, by employing different numbers of MELT motifs in the signaling scaffold in our engineered eSAC activator, we demonstrated the phenomenological synergy among the multiple MELT motifs within a single scaffold [1]. The most striking case was the eSAC activator with six MELT motifs in the signaling scaffold Figure 2.5E, wherein cells with a lower abundance of the eSAC activator may invoke a higher SAC signaling activity. This phenomenon was not apparent when the signaling scaffold incorporated two, three, or four MELT motifs (see Figures 2.5B to 2.5D), probably due to the heterogeneity in the sequences of the MELT motifs that determines their differential affinities to BUB1-BUB3 [1, 32]. We further proved that the variation in the distance between two MELT motifs (in the range of 135–311 residues) minimally affected the SAC signaling activity. In Section 2.6, we proposed a model reminiscent of the hook effect to explain our observations.

The MELT motifs phosphorylated by MPS1 sequentially recruit other SAC proteins like BUB1, BUBR1, and MAD1 [37]. Some of the crucial preconditions in our model proposed in Section 2.6 include (1) that the competition among a large number of phosphorylated MELT motifs effectively diminishes the limited pool of freely diffusive SAC proteins in the cytosol and (2) that the co-localization of multiple SAC proteins on the same KNL1 scaffold superlinearly boosts the SAC signaling activity. In Chapter 3, we demonstrated a negative

correlation between the number of signaling kinetochores in a prometaphase cell and the number of BUB1, BUBR1, and MAD1 proteins recruited per signaling kinetochore. This observation was not due to potential variation in the phosphorylation of KNL1 at signaling kinetochores. We further showed for the first time that recruitment of BUBR1 by BUB1 *per se* contributes to the activity of the kinetochore-based SAC signaling. Although we have not proved the aforementioned superlinearity in kinetochore-based SAC signaling, these pieces of experimental evidence nonetheless unveiled that the foundation of the phenomenological synergy observed in Chapter 2 was (at least partially) the competition among a large number of phosphorylated MELT motifs for the limited pool of downstream SAC proteins, which promote cooperative SAC signaling when they co-localize in close spatial proximity.

The formation of the CDC20-MAD2 subcomplex is considered the rate-limiting step in the assembly of the MCC, the effector molecule of the SAC. Recent studies implied that CDC20 binds to BUB1 and MAD1 cooperatively and that MAD2’s conformational switch and the formation of the CDC20-MAD2 dimer may be spatio-temporally coupled [27, 28]. We independently scrutinized whether and how MAD1 may scaffold such coupling using mutational studies. We discovered that the structural flexibility of MAD1 enabled by its loop region was critical to the SAC signaling activity, which supported the notion of such coupling. Based on our experimental data, we proposed a “knitting” model to explain the catalytic mechanism of MAD1 in promoting the formation of the CDC20-MAD2 dimer. First, MAD1 in its fold-back conformation physically positions the MIM of CDC20 and MAD2 closely, facilitating their association. Second, the cooperative interaction between the scaffold protein MAD1 in its fold-back conformation and CDC20-MAD2 favors the formation of the MAD1RWD-CDC20-MAD2-MAD1MIM complex. Third, the extended conformation breaks such avidity binding and promotes the release of CDC20-MAD2 into the cytosol. However, future studies are needed to fill in the gaps between our current experimental evidence and the “knitting” model.

It should be recognized that my thesis research has some inherent limitations. First, as addressed in Sections 1.3 and 2.7, the sensitivity and responsiveness of the SAC are two sides of the same coin. I only focused on the sensitivity of the SAC by activating the SAC in human cells via the eSAC activator or mitotic drugs. However, during normal mitosis, cells usually do not have to rely on the SAC and delay the progression of mitosis for several hours. Future studies should examine these analyses on the sensitivity of the SAC in a more physiological context, with full consideration of the responsiveness of the SAC in human cells [122].

Second, my studies revolved around the assembly of the MCC. However, even in the presence

of signaling kinetochores, there is a constant tug-of-war between the SAC signaling activity and the counter-acting SAC silencing activity. The silencing of the SAC is mainly mediated by (1) the dephosphorylation of the MELT motifs by phosphatases as well as the shedding of the corona (which together cease the assembly of the MCC) [17, 67], (2) the disassembly or degradation of existing MCCs [70, 71, 72, 73, 74], and (3) the attenuation of the affinity between the MCC and the APC/C [75]. Whether the regulations on the mechanisms that silence the SAC also contribute to the sensitivity of the SAC deserves a systematic evaluation [80, 188].

Finally, mammalian kinetochores usually bind to more than one microtubule in the metaphase and there are two spindle poles from which microtubules may emanate. Therefore, even end-on kinetochore-microtubule attachment could be erroneous. For example, both kinetochores on a duplicated chromosome may attach to microtubules emanating from the same spindle pole (syntelic attachment), and a single kinetochore may attach to microtubules emanating from both spindle poles (merotelic attachment). Cells deploy the error-correction mechanism to correct these erroneous attachment modes to ensure accurate chromosome segregation [118]. How the sensitivity of the SAC fits into the interplay between the SAC and the error-correction mechanism is a developing topic that may broaden our understanding of the SAC in the physiological context.

A more thorough understanding of the SAC may teach us how to prevent or induce its failure and inspire drug discovery to prevent or treat cancers. The revelation of how different molecules orchestrate to build a *de facto* logic gate from biochemical reactions in the case of the SAC may also spark innovations in biochemical circuit engineering.

BIBLIOGRAPHY

- [1] Chu Chen, Ian P Whitney, Anand Banerjee, Carlos Sacristan, Palak Sekhri, David M Kern, Adrienne Fontan, Geert JPL Kops, John J Tyson, Iain M Cheeseman, and Ajit P Joglekar. Ectopic activation of the spindle assembly checkpoint signaling cascade reveals its biochemical design. *Current Biology*, 29(1):104–119, 2019.
- [2] Anand Banerjee, Chu Chen, Lauren Humphrey, John J Tyson, and Ajit P Joglekar. BubR1 recruitment to the kinetochore via Bub1 enhances Spindle Assembly Checkpoint signaling. *bioRxiv*, 2021.
- [3] Chu Chen, Lauren Humphrey, Soubhagyalaxmi Jema, Frank Ferrari, and Ajit P Joglekar. Bub1 availability limits the Spindle Assembly Checkpoint signaling strength of human kinetochores. *bioRxiv*, 2022.
- [4] Bruce Alberts, Alexander Johnson, Julian Lewis, Martin Raff, Keith Roberts, and Peter Walter. *Molecular Biology of the Cell*. Garland Science, 4th edition, 2002.
- [5] Conly L Rieder, Richard W Cole, Alexey Khodjakov, and Greenfield Sluder. The checkpoint delaying anaphase in response to chromosome monoorientation is mediated by an inhibitory signal produced by unattached kinetochores. *The Journal of Cell Biology*, 130(4):941–948, 1995.
- [6] Philip Auckland and Andrew D McAinsh. Building an integrated model of chromosome congression. *Journal of Cell Science*, 128(18):3363–3374, 2015.
- [7] Conly L Rieder and ED Salmon. The vertebrate cell kinetochore and its roles during mitosis. *Trends in Cell Biology*, 8(8):310–318, 1998.
- [8] Kim Livezey Wendell, Leslie Wilson, and Mary Ann Jordan. Mitotic block in HeLa cells by vinblastine: ultrastructural changes in kinetochore-microtubule attachment and in centrosomes. *Journal of Cell Science*, 104(2):261–274, 1993.
- [9] Anatoly V Zaytsev, Lynsie JR Sundin, Keith F DeLuca, Ekaterina L Grishchuk, and Jennifer G DeLuca. Accurate phosphoregulation of kinetochore-microtubule affinity requires unconstrained molecular interactions. *Journal of Cell Biology*, 206(1):45–59, 2014.
- [10] Anatoly V Zaytsev, Jeanne E Mick, Evgeny Maslennikov, Boris Nikashin, Jennifer G DeLuca, and Ekaterina L Grishchuk. Multisite phosphorylation of the NDC80 com-

plex gradually tunes its microtubule-binding affinity. *Molecular Biology of the Cell*, 26(10):1829–1844, 2015.

- [11] Banafsheh Etemad and Geert JPL Kops. Attachment issues: kinetochore transformations and spindle checkpoint silencing. *Current Opinion in Cell Biology*, 39:101–108, 2016.
- [12] Alexander A Kukreja, Sisira Kavuri, and Ajit P Joglekar. Microtubule attachment and centromeric tension shape the protein architecture of the human kinetochore. *Current Biology*, 30(24):4869–4881, 2020.
- [13] Eugenio Marco, Jonas F Dorn, Pei-hsin Hsu, Khuloud Jaqaman, Peter K Sorger, and Gaudenz Danuser. *S. cerevisiae* chromosomes biorient via gradual resolution of syntely between S phase and anaphase. *Cell*, 154(5):1127–1139, 2013.
- [14] Geert JPL Kops and Reto Gassmann. Crowning the kinetochore: the fibrous corona in chromosome segregation. *Trends in Cell Biology*, 30(8):653–667, 2020.
- [15] Carlos Sacristan, Misbha Ud Din Ahmad, Jenny Keller, Job Fermie, Vincent Groenewold, Eelco Tromer, Alexander Fish, Roberto Melero, José María Carazo, Judith Klumperman, Andrea Musacchio, Anastassis Perrakis, and Geert JPL Kops. Dynamic kinetochore size regulation promotes microtubule capture and chromosome biorientation in mitosis. *Nature Cell Biology*, 20(7):800–810, 2018.
- [16] Tobias Raisch, Giuseppe Ciossani, Ennio d’Amico, Verena Cmentowski, Sara Carmignani, Stefano Maffini, Felipe Merino, Sabine Wohlgemuth, Ingrid R Vetter, Stefan Raunser, and Andrea Musacchio. Structure of the RZZ complex and molecular basis of Spindly-driven corona assembly at human kinetochores. *bioRxiv*, 2021.
- [17] BJ Howell, BF McEwen, JC Canman, DB Hoffman, EM Farrar, CL Rieder, and ED Salmon. Cytoplasmic dynein/dynactin drives kinetochore protein transport to the spindle poles and has a role in mitotic spindle checkpoint inactivation. *The Journal of Cell Biology*, 155(7):1159–1172, 2001.
- [18] Xuebiao Yao, Karen L Anderson, and Don W Cleveland. The microtubule-dependent motor centromere-associated protein E (CENP-E) is an integral component of kinetochore corona fibers that link centromeres to spindle microtubules. *The Journal of Cell Biology*, 139(2):435–447, 1997.
- [19] Roshan L Shrestha and Viji M Draviam. Lateral to end-on conversion of chromosome-microtubule attachment requires kinesins CENP-E and MCAK. *Current Biology*, 23(16):1514–1526, 2013.
- [20] Yuejia Huang, Lin Lin, Xing Liu, Sheng Ye, Phil Y Yao, Wenwen Wang, Fengrui Yang, Xinjiao Gao, Junying Li, Yin Zhang, Jiancun Zhang, Zhihong Yang, Xu Liu, Zhenye Yang, Jianye Zang, Maikun Teng, Zhiyong Wang, Ke Ruan, Xia Ding, Lin Li, Don W. Cleveland, Rongguang Zhang, and Xuebiao Yao. BubR1 phosphorylates CENP-E as a switch enabling the transition from lateral association to end-on capture of spindle microtubules. *Cell Research*, 29(7):562–578, 2019.

- [21] Philip Auckland, Emanuele Roscioli, Helena Louise Elvidge Coker, and Andrew D McAinsh. CENP-F stabilizes kinetochore-microtubule attachments and limits dynein stripping of corona cargoes. *Journal of Cell Biology*, 219(5), 2020.
- [22] Valentin Magidson, Raja Paul, Nachen Yang, Jeffrey G Ault, Christopher B O'Connell, Irina Tikhonenko, Bruce F McEwen, Alex Mogilner, and Alexey Khodjakov. Adaptive changes in the kinetochore architecture facilitate proper spindle assembly. *Nature Cell Biology*, 17(9):1134–1144, 2015.
- [23] Jonathan Kuhn and Sophie Dumont. Spindle assembly checkpoint satisfaction occurs via end-on but not lateral attachments under tension. *Journal of Cell Biology*, 216(6):1533–1542, 2017.
- [24] Pablo Lara-Gonzalez, Jonathon Pines, and Arshad Desai. Spindle assembly checkpoint activation and silencing at kinetochores. In *Seminars in Cell & Developmental Biology*, volume 117, pages 86–98, 2021.
- [25] Lindsey A Allan, Magda Camacho Reis, Giuseppe Ciossani, Pim J Huis in 't Veld, Sabine Wohlgemuth, Geert JPL Kops, Andrea Musacchio, and Adrian T Saurin. Cyclin B1 scaffolds MAD1 at the kinetochore corona to activate the mitotic checkpoint. *The EMBO Journal*, page e103180, 2020.
- [26] Virginia Silió, Andrew D McAinsh, and Jonathan B Millar. KNL1-Bubs and RZZ provide two separable pathways for checkpoint activation at human kinetochores. *Developmental Cell*, 35(5):600–613, 2015.
- [27] Valentina Piano, Amal Alex, Patricia Stege, Stefano Maffini, Gerardo A Stoppiello, Pim J Huis In 't Veld, Ingrid R Vetter, and Andrea Musacchio. CDC20 assists its catalytic incorporation in the mitotic checkpoint complex. *Science*, 371(6524):67–71, 2021.
- [28] Pablo Lara-Gonzalez, Taekyung Kim, Karen Oegema, Kevin Corbett, and Arshad Desai. A tripartite mechanism catalyzes Mad2-Cdc20 assembly at unattached kinetochores. *Science*, 371(6524):64–67, 2021.
- [29] Zhejian Ji, Haishan Gao, and Hongtao Yu. Kinetochore attachment sensed by competitive Mps1 and microtubule binding to Ndc80C. *Science*, 348(6240):1260–1264, 2015.
- [30] Yoshitaka Hiruma, Carlos Sacristan, Spyridon T Pachis, Athanassios Adamopoulos, Timo Kuijt, Marcellus Ubbink, Eleonore von Castelmur, Anastassis Perrakis, and Geert JPL Kops. Competition between MPS1 and microtubules at kinetochores regulates spindle checkpoint signaling. *Science*, 348(6240):1264–1267, 2015.
- [31] Mathijs Vleugel, Eelco Tromer, Manja Omerzu, Vincent Groenewold, Wilco Nijenhuis, Berend Snel, and Geert J.P.L. Kops. Arrayed BUB recruitment modules in the kinetochore scaffold KNL1 promote accurate chromosome segregation. *Journal of Cell Biology*, 203(6):943–955, 2013.

- [32] Mathijs Vleugel, Manja Omerzu, Vincent Groenewold, Michael A Hadders, Susanne MA Lens, and Geert JPL Kops. Sequential multisite phospho-regulation of KNL1-BUB3 interfaces at mitotic kinetochores. *Molecular Cell*, 57(5):824–835, 2015.
- [33] Katharina Overlack, Ivana Primorac, Mathijs Vleugel, Veronica Krenn, Stefano Maffini, Ingrid Hoffmann, Geert JPL Kops, and Andrea Musacchio. A molecular basis for the differential roles of Bub1 and BubR1 in the spindle assembly checkpoint. *eLife*, 4:e05269, 2015.
- [34] Gang Zhang, Blanca Lopez Mendez, Garry G Sedgwick, and Jakob Nilsson. Two functionally distinct kinetochore pools of BubR1 ensure accurate chromosome segregation. *Nature Communications*, 7(1):1–12, 2016.
- [35] Elyse S Fischer, Conny WH Yu, Dom Bellini, Stephen H McLaughlin, Christian M Orr, Armin Wagner, Stefan MV Freund, and David Barford. Molecular mechanism of Mad1 kinetochore targeting by phosphorylated Bub1. *EMBO Reports*, 22(7):e52242, 2021.
- [36] Alex C Faesen, Maria Thanasoula, Stefano Maffini, Claudia Breit, Franziska Müller, Suzan Van Gerwen, Tanja Bange, and Andrea Musacchio. Basis of catalytic assembly of the mitotic checkpoint complex. *Nature*, 542(7642):498–502, 2017.
- [37] Zhejian Ji, Haishan Gao, Luying Jia, Bing Li, and Hongtao Yu. A sequential multi-target Mps1 phosphorylation cascade promotes spindle checkpoint signaling. *eLife*, 6:e22513, 2017.
- [38] Rey-Huei Chen, D Michelle Brady, Dana Smith, Andrew W Murray, and Kevin G Hardwick. The spindle checkpoint of budding yeast depends on a tight complex between the Mad1 and Mad2 proteins. *Molecular Biology of the Cell*, 10(8):2607–2618, 1999.
- [39] John Jumper et al. Highly accurate protein structure prediction with AlphaFold. *Nature*, 596(7873):583–589, 2021.
- [40] Kathryn Tunyasuvunakool et al. Highly accurate protein structure prediction for the human proteome. *Nature*, 596(7873):590–596, 2021.
- [41] Lucia Sironi, Marina Mapelli, Stefan Knapp, Anna De Antoni, Kuan-Teh Jeang, and Andrea Musacchio. Crystal structure of the tetrameric Mad1-Mad2 core complex: implications of a ‘safety belt’ binding mechanism for the spindle checkpoint. *The EMBO Journal*, 21(10):2496–2506, 2002.
- [42] Eelco Tromer, Berend Snel, and Geert JPL Kops. Widespread recurrent patterns of rapid repeat evolution in the kinetochore scaffold KNL1. *Genome Biology and Evolution*, 7(8):2383–2393, 2015.
- [43] Nitobe London, Steven Ceto, Jeffrey A Ranish, and Sue Biggins. Phosphoregulation of Spc105 by Mps1 and PP1 regulates Bub1 localization to kinetochores. *Current Biology*, 22(10):900–906, 2012.

- [44] Lindsey A Shepperd, John C Meadows, Alicja M Sochaj, Theresa C Lancaster, Juan Zou, Graham J Buttrick, Juri Rappaport, Kevin G Hardwick, and Jonathan BA Millar. Phosphodependent recruitment of Bub1 and Bub3 to Spc7/KNL1 by Mph1 kinase maintains the spindle checkpoint. *Current Biology*, 22(10):891–899, 2012.
- [45] Yuya Yamagishi, Ching-Hui Yang, Yuji Tanno, and Yoshinori Watanabe. MPS1/Mph1 phosphorylates the kinetochore protein KNL1/Spc7 to recruit SAC components. *Nature Cell Biology*, 14(7):746–752, 2012.
- [46] William CH Chao, Kiran Kulkarni, Ziguang Zhang, Eric H Kong, and David Barford. Structure of the mitotic checkpoint complex. *Nature*, 484(7393):208–213, 2012.
- [47] Claudio Alfieri, Leifu Chang, Ziguang Zhang, Jing Yang, Sarah Maslen, Mark Skehel, and David Barford. Molecular basis of APC/C regulation by the spindle assembly checkpoint. *Nature*, 536(7617):431–436, 2016.
- [48] Masaya Yamaguchi, Ryan VanderLinden, Florian Weissmann, Renping Qiao, Prakash Dube, Nicholas G Brown, David Haselbach, Wei Zhang, Sachdev S Sidhu, Jan-Michael Peters, Holger Stark, and Brenda A Schulman. Cryo-EM of mitotic checkpoint complex-bound APC/C reveals reciprocal and conformational regulation of ubiquitin ligation. *Molecular Cell*, 63(4):593–607, 2016.
- [49] Paul Clute and Jonathon Pines. Temporal and spatial control of cyclin B1 destruction in metaphase. *Nature Cell Biology*, 1(2):82–87, 1999.
- [50] Donald C Chang, Naihan Xu, and Kathy Q Luo. Degradation of cyclin B is required for the onset of anaphase in mammalian cells. *Journal of Biological Chemistry*, 278(39):37865–37873, 2003.
- [51] Jun Yu, Pierre Raia, Chloe M Ghent, Tobias Raisch, Yashar Sadian, Simone Cavadini, Pramod M Sabale, David Barford, Stefan Raunser, David O Morgan, and Andreas Boland. Structural basis of human separase regulation by securin and CDK1-cyclin B1. *Nature*, 596(7870):138–142, 2021.
- [52] Giuseppe Ciossani, Katharina Overlack, Arsen Petrovic, Pim J Huis In't Veld, Carolin Koerner, Sabine Wohlgemuth, Stefano Maffini, and Andrea Musacchio. The kinetochore proteins CENP-E and CENP-F directly and specifically interact with distinct BUB mitotic checkpoint Ser/Thr kinases. *Journal of Biological Chemistry*, 293(26):10084–10101, 2018.
- [53] Haining Zhou, Tianning Wang, Tao Zheng, Junlin Teng, and Jianguo Chen. Cep57 is a Mis12-interacting kinetochore protein involved in kinetochore targeting of Mad1-Mad2. *Nature Communications*, 7(1):1–13, 2016.
- [54] Gang Zhang, Thomas Kruse, Claudia Guasch Boldú, Dimitriya H Garvanska, Fabian Coscia, Matthias Mann, Marin Barisic, and Jakob Nilsson. Efficient mitotic checkpoint signaling depends on integrated activities of Bub1 and the RZZ complex. *The EMBO Journal*, 38(7):e100977, 2019.

- [55] Roger Karess. Rod-Zw10-Zwilch: a key player in the spindle checkpoint. *Trends in Cell Biology*, 15(7):386–392, 2005.
- [56] Sang Hyun Lee, Harry Sterling, Alma Burlingame, and Frank McCormick. Tpr directly binds to Mad1 and Mad2 and is important for the Mad1-Mad2-mediated mitotic spindle checkpoint. *Genes & Development*, 22(21):2926–2931, 2008.
- [57] Veronica Rodriguez-Bravo, John Maciejowski, Jennifer Corona, Håkon Kirkeby Buch, Philippe Collin, Masato T Kanemaki, Jagesh V Shah, and Prasad V Jallepalli. Nuclear pores protect genome integrity by assembling a premitotic and Mad1-dependent anaphase inhibitor. *Cell*, 156(5):1017–1031, 2014.
- [58] Cordy L Rieder, Adriene Schultz, Richard Cole, and Greenfield Sluder. Anaphase onset in vertebrate somatic cells is controlled by a checkpoint that monitors sister kinetochore attachment to the spindle. *The Journal of Cell Biology*, 127(5):1301–1310, 1994.
- [59] Philippe Collin, Oxana Nashchekina, Rachael Walker, and Jonathon Pines. The spindle assembly checkpoint works like a rheostat rather than a toggle switch. *Nature Cell Biology*, 15(11):1378–1385, 2013.
- [60] Amalie E Dick and Daniel W Gerlich. Kinetic framework of spindle assembly checkpoint signalling. *Nature Cell Biology*, 15(11):1370–1377, 2013.
- [61] Susanne Hellmuth, Laura Gómez-H, Alberto M Pendás, and Olaf Stemmann. Securin-independent regulation of separase by checkpoint-induced shugoshin-MAD2. *Nature*, 580(7804):536–541, 2020.
- [62] Sang Hyun Lee, Frank McCormick, and Hideyuki Saya. Mad2 inhibits the mitotic kinesin MKlp2. *Journal of Cell Biology*, 191(6):1069–1077, 2010.
- [63] Sikai Liu, Xiao Yuan, Ping Gui, Ran Liu, Olanrewaju Durojaye, Donald L Hill, Chuanhai Fu, Xuebiao Yao, Zhen Dou, and Xing Liu. Mad2 promotes Cyclin B2 recruitment to the kinetochore for guiding accurate mitotic checkpoint. *EMBO Reports*, page e54171, 2022.
- [64] Lori B Koch, Kwaku N Opoku, Yi Deng, Adrienne Barber, Aimee J Littleton, Nitobe London, Sue Biggins, and Charles L Asbury. Autophosphorylation is sufficient to release Mps1 kinase from native kinetochores. *Proceedings of the National Academy of Sciences*, 116(35):17355–17360, 2019.
- [65] Junbin Qian, Maria Adelaida García-Gimeno, Monique Beullens, Maria Giulia Manzione, Gerd Van der Hoeven, Juan Carlos Igual, Miguel Heredia, Pascual Sanz, Lendert Gelens, and Mathieu Bollen. An attachment-independent biochemical timer of the spindle assembly checkpoint. *Molecular Cell*, 68(4):715–730, 2017.
- [66] Antonio Espert, Pelin Uluocak, Ricardo Nunes Bastos, Davinderpreet Mangat, Philipp Graab, and Ulrike Gruneberg. PP2A-B56 opposes Mps1 phosphorylation of Knl1

- and thereby promotes spindle assembly checkpoint silencing. *Journal of Cell Biology*, 206(7):833–842, 2014.
- [67] Wilco Nijenhuis, Giulia Vallardi, Antoinette Teixeira, Geert JPL Kops, and Adrian T Saurin. Negative feedback at kinetochores underlies a responsive spindle checkpoint signal. *Nature Cell Biology*, 16(12):1257–1264, 2014.
- [68] Junran Hou, Weiqian Zeng, Yeqing Zong, Zehua Chen, Chensi Miao, Baojun Wang, and Chunbo Lou. Engineering the ultrasensitive transcription factors by fusing a modular oligomerization domain. *ACS Synthetic Biology*, 7(5):1188–1194, 2018.
- [69] Manuel Razo-Mejia, Stephanie L Barnes, Nathan M Belliveau, Griffin Chure, Tal Einav, Mitchell Lewis, and Rob Phillips. Tuning transcriptional regulation through signaling: a predictive theory of allosteric induction. *Cell Systems*, 6(4):456–469, 2018.
- [70] Jakob Nilsson, Mona Yekezare, Jeremy Minshull, and Jonathon Pines. The APC/C maintains the spindle assembly checkpoint by targeting Cdc20 for destruction. *Nature Cell Biology*, 10(12):1411–1420, 2008.
- [71] Sharon Kaisari, Danielle Sitry-Shevah, Shirly Miniowitz-Shemtov, Adar Teichner, and Avram Hershko. Role of CCT chaperonin in the disassembly of mitotic checkpoint complexes. *Proceedings of the National Academy of Sciences*, 114(5):956–961, 2017.
- [72] Danielle Sitry-Shevah, Sharon Kaisari, Adar Teichner, Shirly Miniowitz-Shemtov, and Avram Hershko. Role of ubiquitylation of components of mitotic checkpoint complex in their dissociation from anaphase-promoting complex/cyclosome. *Proceedings of the National Academy of Sciences*, 115(8):1777–1782, 2018.
- [73] Sharon Kaisari, Shirly Miniowitz-Shemtov, Danielle Sitry-Shevah, Pnina Shomer, Guennadi Kozlov, Kalle Gehring, and Avram Hershko. Role of ubiquitin-protein ligase UBR5 in the disassembly of mitotic checkpoint complexes. *Proceedings of the National Academy of Sciences*, 119(9):e2121478119, 2022.
- [74] Claudio Alfieri, Leifu Chang, and David Barford. Mechanism for remodelling of the cell cycle checkpoint protein MAD2 by the ATPase TRIP13. *Nature*, 559(7713):274–278, 2018.
- [75] Stanislau Yatskevich, Jessie S Kroonen, Claudio Alfieri, Thomas Tischer, Anna C Howes, Linda Clijsters, Jing Yang, Ziguang Zhang, Kaige Yan, Alfred CO Vertegaal, and David Barford. Molecular mechanisms of APC/C release from spindle assembly checkpoint inhibition by APC/C SUMOylation. *Cell Reports*, 34(13):108929, 2021.
- [76] Banafsheh Etemad, Abel Vertesy, Timo EF Kuijt, Carlos Sacristan, Alexander van Oudenaarden, and Geert JPL Kops. Spindle checkpoint silencing at kinetochores with submaximal microtubule occupancy. *Journal of Cell Science*, 132(12):jcs231589, 2019.
- [77] Jonathan Kuhn and Sophie Dumont. Mammalian kinetochores count attached microtubules in a sensitive and switch-like manner. *Journal of Cell Biology*, 218(11):3583–3596, 2019.

- [78] James E Ferrell. Q&A: cooperativity. *Journal of Biology*, 8(6):1–6, 2009.
- [79] James E Ferrell. Tripping the switch fantastic: how a protein kinase cascade can convert graded inputs into switch-like outputs. *Trends in Biochemical Sciences*, 21(12):460–466, 1996.
- [80] James E Ferrell and Sang Hoon Ha. Ultrasensitivity part I: Michaelian responses and zero-order ultrasensitivity. *Trends in Biochemical Sciences*, 39(10):496–503, 2014.
- [81] James E Ferrell and Sang Hoon Ha. Ultrasensitivity part II: multisite phosphorylation, stoichiometric inhibitors, and positive feedback. *Trends in Biochemical Sciences*, 39(11):556–569, 2014.
- [82] James E Ferrell and Sang Hoon Ha. Ultrasensitivity part III: cascades, bistable switches, and oscillators. *Trends in Biochemical Sciences*, 39(12):612–618, 2014.
- [83] Daniel E Koshland Jr, George Némethy, and David Filmer. Comparison of experimental binding data and theoretical models in proteins containing subunits. *Biochemistry*, 5(1):365–385, 1966.
- [84] Jacque Monod, Jeffries Wyman, and Jean-Pierre Changeux. On the nature of allosteric transitions: a plausible model. *Journal of Molecular Biology*, 12(1):88–118, 1965.
- [85] Donald M Crothers and Henry Metzger. The influence of polyvalency on the binding properties of antibodies. *Immunochemistry*, 9(3):341–357, 1972.
- [86] Allen P Minton. The influence of macromolecular crowding and macromolecular confinement on biochemical reactions in physiological media. *Journal of Biological Chemistry*, 276(14):10577–10580, 2001.
- [87] Priyanka Singh, Marion E Pesenti, Stefano Maffini, Sara Carmignani, Marius Hedtfeld, Arsen Petrovic, Anupallavi Srinivasamani, Tanja Bange, and Andrea Musacchio. BUB1 and CENP-U, primed by CDK1, are the main PLK1 kinetochore receptors in mitosis. *Molecular Cell*, 81(1):67–87, 2021.
- [88] Sanne Hindriksen, Susanne Lens, and Michael A Hadders. The ins and outs of Aurora B inner centromere localization. *Frontiers in Cell and Developmental Biology*, 5:112, 2017.
- [89] Michael A Lampson and Tarun M Kapoor. The human mitotic checkpoint protein BubR1 regulates chromosome-spindle attachments. *Nature Cell Biology*, 7(1):93–98, 2005.
- [90] Saskia JE Suijkerbuijk, Mathijs Vleugel, Antoinette Teixeira, and Geert JPL Kops. Integration of kinase and phosphatase activities by BUBR1 ensures formation of stable kinetochore-microtubule attachments. *Developmental Cell*, 23(4):745–755, 2012.

- [91] Thomas Kruse, Gang Zhang, Marie Sofie Yoo Larsen, Tiziana Lischetti, Werner Streicher, Tine Kragh Nielsen, Sara Petersen Bjørn, and Jakob Nilsson. Direct binding between BubR1 and B56-PP2A phosphatase complexes regulate mitotic progression. *Journal of Cell Science*, 126(5):1086–1092, 2013.
- [92] Peng Xu, Elizabeth A Raetz, Mayumi Kitagawa, David M Virshup, and Sang Hyun Lee. BUBR1 recruits PP2A via the B56 family of targeting subunits to promote chromosome congression. *Biology Open*, 2(5):479–486, 2013.
- [93] Stephen S Taylor, Edward Ha, and Frank McKeon. The human homologue of Bub3 is required for kinetochore localization of Bub1 and a Mad3/Bub1-related protein kinase. *The Journal of Cell Biology*, 142(1):1–11, 1998.
- [94] Stephanie Heinrich, Eva-Maria Geissen, Julia Kamenz, Susanne Trautmann, Christian Widmer, Philipp Drewe, Michael Knop, Nicole Radde, Jan Hasenauer, and Silke Hauf. Determinants of robustness in spindle assembly checkpoint signalling. *Nature Cell Biology*, 15(11):1328–1339, 2013.
- [95] Chunying Yang, Jianwei Hao, Dejuan Kong, Xiaoli Cui, Wei Zhang, Haibo Wang, Xiaojing Guo, Shumei Ma, Xiaodong Liu, Peiyu Pu, and Bo Xu. ATM-mediated Mad1 Serine 214 phosphorylation regulates Mad1 dimerization and the spindle assembly checkpoint. *Carcinogenesis*, 35(9):2007–2013, 2014.
- [96] Sean D Ryan, Eric MC Britigan, Lauren M Zasadil, Kristen Witte, Anjon Audhya, Avtar Roopra, and Beth A Weaver. Up-regulation of the mitotic checkpoint component Mad1 causes chromosomal instability and resistance to microtubule poisons. *Proceedings of the National Academy of Sciences*, 109(33):E2205–E2214, 2012.
- [97] Jonne A Raaijmakers, Roy GHP van Heesbeen, Vincent A Blomen, Louise ME Janssen, Ferdy van Diemen, Thijn R Brummelkamp, and René H Medema. BUB1 is essential for the viability of human cells in which the spindle assembly checkpoint is compromised. *Cell Reports*, 22(6):1424–1438, 2018.
- [98] Jose-Antonio Rodriguez-Rodriguez, Clare Lewis, Kara L McKinley, Vitali Sikirzhytski, Jennifer Corona, John Maciejowski, Alexey Khodjakov, Iain M Cheeseman, and Prasad V Jallepalli. Distinct roles of RZZ and Bub1-KNL1 in mitotic checkpoint signaling and kinetochore expansion. *Current Biology*, 28(21):3422–3429, 2018.
- [99] Steven Lin, Brett T Staahl, Ravi K Alla, and Jennifer A Doudna. Enhanced homology-directed human genome engineering by controlled timing of CRISPR/Cas9 delivery. *eLife*, 3:e04766, 2014.
- [100] Kenneth W Wood et al. Antitumor activity of an allosteric inhibitor of centromere-associated protein-E. *Proceedings of the National Academy of Sciences*, 107(13):5839–5844, 2010.
- [101] Mary Ann Jordan, Douglas Thrower, and Leslie Wilson. Effects of vinblastine, podophyllotoxin and nocodazole on mitotic spindles. Implications for the role of microtubule dynamics in mitosis. *Journal of Cell Science*, 102(3):401–416, 1992.

- [102] Cayetana Vázquez-Diez, Lia Mara Gomes Paim, and Greg FitzHarris. Cell-size-independent spindle checkpoint failure underlies chromosome segregation error in mouse embryos. *Current Biology*, 29(5):865–873, 2019.
- [103] Tommaso Cavazza, Yuko Takeda, Antonio Z Politi, Magomet Aushev, Patrick Aldag, Clara Baker, Meenakshi Choudhary, Jonas Bucevičius, Gražvydas Lukinavičius, Kay Elder, Martyn Blayney, Andrea Lucas-Hahn, Heiner Niemann, Mary Herbert, and Melina Schuh. Parental genome unification is highly error-prone in mammalian embryos. *Cell*, 184(11):2860–2877, 2021.
- [104] Kelsey E Brooks, Brittany L Daughtry, Brett Davis, Melissa Y Yan, Suzanne S Fei, Selma Shepherd, Lucia Carbone, and Shawn L Chavez. Molecular contribution to embryonic aneuploidy and karyotypic complexity in initial cleavage divisions of mammalian development. *Development*, 2022.
- [105] Kevin G Hardwick, Eric Weiss, Francis C Luca, Mark Winey, and Andrew W Murray. Activation of the budding yeast spindle assembly checkpoint without mitotic spindle disruption. *Science*, 273(5277):953–956, 1996.
- [106] Edward R Ballister, Michelle Riegman, and Michael A Lampson. Recruitment of Mad1 to metaphase kinetochores is sufficient to reactivate the mitotic checkpoint. *Journal of Cell Biology*, 204(6):901–908, 2014.
- [107] Pavithra Aravamudhan, Alan A Goldfarb, and Ajit P Joglekar. The kinetochore encodes a mechanical switch to disrupt spindle assembly checkpoint signalling. *Nature Cell Biology*, 17(7):868–879, 2015.
- [108] Ivan Yuan, Ioanna Leontiou, Priya Amin, Karen M May, Sadhbh Soper Ní Chafraidh, Eliška Zlámalová, and Kevin G Hardwick. Generation of a spindle checkpoint arrest from synthetic signaling assemblies. *Current Biology*, 27(1):137–143, 2017.
- [109] Laura A Banaszynski, Corey W Liu, and Thomas J Wandless. Characterization of the FKBP·Rapamycin·FRB ternary complex. *Journal of the American Chemical Society*, 127(13):4715–4721, 2005.
- [110] Piyush Khandelia, Karen Yap, and Eugene V. Makeyev. Streamlined platform for short hairpin RNA interference and transgenesis in cultured mammalian cells. *Proceedings of the National Academy of Sciences*, 108(31):12799–12804, 2011.
- [111] Tomomi Kiyomitsu, Chikashi Obuse, and Mitsuhiro Yanagida. Human Blinkin/AF15q14 is required for chromosome alignment and the mitotic checkpoint through direct interaction with Bub1 and BubR1. *Developmental Cell*, 13(5):663–676, 2007.
- [112] Emanuela Screpanti, Anna De Antoni, Gregory M Alushin, Arsen Petrovic, Tiziana Melis, Eva Nogales, and Andrea Musacchio. Direct binding of Cenp-C to the Mis12 complex joins the inner and outer kinetochore. *Current Biology*, 21(5):391–398, 2011.

- [113] Arsen Petrovic, Shyamal Mosalaganti, Jenny Keller, Marta Mattiuzzo, Katharina Overlack, Veronica Krenn, Anna De Antoni, Sabine Wohlgemuth, Valentina Cecatiello, Sebastiano Pasqualato, Stefan Raunser, and Andrea Musacchio. Modular assembly of RWD domains on the Mis12 complex underlies outer kinetochore organization. *Molecular Cell*, 53(4):591–605, 2014.
- [114] Arsen Petrovic, Jenny Keller, Yahui Liu, Katharina Overlack, Juliane John, Yoana N Dimitrova, Simon Jenni, Suzan Van Gerwen, Patricia Stege, Sabine Wohlgemuth, Pascaleine Rombaut, Franz Herzog, Stephen C Harrison, Ingrid R Vetter, and Andrea Musacchio. Structure of the MIS12 complex and molecular basis of its interaction with CENP-C at human kinetochores. *Cell*, 167(4):1028–1040, 2016.
- [115] Daniel P Maskell, Xiao-Wen Hu, and Martin R Singleton. Molecular architecture and assembly of the yeast kinetochore MIND complex. *Journal of Cell Biology*, 190(5):823–834, 2010.
- [116] Nathan C. Shaner, Gerard G. Lambert, Andrew Chammas, Yuhui Ni, Paula J. Cranfill, Michelle A. Baird, Brittney R. Sell, John R. Allen, Richard N. Day, Maria Israelsson, Michael W. Davidson, and Jiwu Wang. A bright monomeric green fluorescent protein derived from *Branchiostoma lanceolatum*. *Nature Methods*, 10(5):407–409, 2013.
- [117] Stephen D Liberles, Steven T Diver, David J Austin, and Stuart L Schreiber. Inducible gene expression and protein translocation using nontoxic ligands identified by a mammalian three-hybrid screen. *Proceedings of the National Academy of Sciences*, 94(15):7825–7830, 1997.
- [118] Juraj Gregan, Silvia Polakova, Lijuan Zhang, Iva M Tolić-Nørrelykke, and Daniela Cimini. Merotelic kinetochore attachment: causes and effects. *Trends in Cell Biology*, 21(6):374–381, 2011.
- [119] Tatsuro Otaki. Artifact halo reduction in phase contrast microscopy using apodization. *Optical Review*, 7(2):119–122, 2000.
- [120] Gina V Caldas and Jennifer G DeLuca. KNL1: bringing order to the kinetochore. *Chromosoma*, 123(3):169–181, 2014.
- [121] Richard A McPherson and Matthew R Pincus. *Henry's Clinical Diagnosis and Management by Laboratory Methods*. Elsevier, 24th edition, 2021.
- [122] Babhrubahan Roy, Simon JY Han, Adrienne Nicole Fontan, and Ajit P Joglekar. The copy-number and varied strengths of MELT motifs in Spc105 balance the strength and responsiveness of the spindle assembly checkpoint. *eLife*, 9:e55096, 2020.
- [123] David M Kern, Taekyung Kim, Mike Rigney, Neil Hattersley, Arshad Desai, and Iain M Cheeseman. The outer kinetochore protein KNL-1 contains a defined oligomerization domain in nematodes. *Molecular Biology of the Cell*, 26(2):229–237, 2015.

- [124] Marija Buljan, Guilhem Chalancon, A Keith Dunker, Alex Bateman, S Balaji, Monika Fuxreiter, and M Madan Babu. Alternative splicing of intrinsically disordered regions and rewiring of protein interactions. *Current Opinion in Structural Biology*, 23(3):443–450, 2013.
- [125] Mohan T Bolisetty and Karen L Beemon. Splicing of internal large exons is defined by novel cis-acting sequence elements. *Nucleic Acids Research*, 40(18):9244–9254, 2012.
- [126] Kim D Pruitt et al. The consensus coding sequence (CCDS) project: identifying a common protein-coding gene set for the human and mouse genomes. *Genome Research*, 19(7):1316–1323, 2009.
- [127] Robin M Ricke, Karthik B Jeganathan, and Jan M van Deursen. Bub1 overexpression induces aneuploidy and tumor formation through Aurora B kinase hyperactivation. *Journal of Cell Biology*, 193(6):1049–1064, 2011.
- [128] Yin Cai, M. Julius Hossain, Jean-Karim Hériché, Antonio Z. Politi1, Nike Walther, Birgit Koch, Malte Wachsmuth, Bianca Nijmeijer1, Moritz Kueblbeck, Marina Martinic-Kavur, Rene Ladurner, Stephanie Alexander, Jan-Michael Peters, and Jan Ellenberg. Experimental and computational framework for a dynamic protein atlas of human cell division. *Nature*, 561(7723):411–415, 2018.
- [129] Wei Qi and Hongtao Yu. KEN-box-dependent degradation of the Bub1 spindle checkpoint kinase by the anaphase-promoting complex/cyclosome. *Journal of Biological Chemistry*, 282(6):3672–3679, 2007.
- [130] Karen Man-Fong Sze, Yick-Pang Ching, Dong-Yan Jin, and Irene Oi-Lin Ng. Role of a novel splice variant of mitotic arrest deficient 1 (MAD1), MAD1 β , in mitotic checkpoint control in liver cancer. *Cancer Research*, 68(22):9194–9201, 2008.
- [131] Stephen S Taylor, Deema Hussein, Yunmei Wang, Sarah Elderkin, and Christopher J Morrow. Kinetochore localisation and phosphorylation of the mitotic checkpoint components Bub1 and BubR1 are differentially regulated by spindle events in human cells. *Journal of Cell Science*, 114(24):4385–4395, 2001.
- [132] Elsa Logarinho, Tatiana Resende, Cláudia Torres, and Hassan Bousbaa. The human spindle assembly checkpoint protein Bub3 is required for the establishment of efficient kinetochore-microtubule attachments. *Molecular Biology of the Cell*, 19(4):1798–1813, 2008.
- [133] Pavithra Aravamudhan, Renjie Chen, Babhrubahan Roy, Janice Sim, and Ajit P Joglekar. Dual mechanisms regulate the recruitment of spindle assembly checkpoint proteins to the budding yeast kinetochore. *Molecular Biology of the Cell*, 27(22):3405–3417, 2016.
- [134] Geert JPL Kops, Yumi Kim, Beth AA Weaver, Yinghui Mao, Ian McLeod, John R Yates III, Mitsuo Tagaya, and Don W Cleveland. ZW10 links mitotic checkpoint signaling to the structural kinetochore. *The Journal of Cell Biology*, 169(1):49–60, 2005.

- [135] Timo EF Kuijt, Maaike LA Lambers, Sonja Weterings, Bas Ponsioen, Ana CF Bolhaqueiro, Debbie HM Staijen, and Geert JPL Kops. A biosensor for the mitotic kinase MPS1 reveals spatiotemporal activity dynamics and regulation. *Current Biology*, 30(19):3862–3870, 2020.
- [136] Jonathan D Violin, Jin Zhang, Roger Y Tsien, and Alexandra C Newton. A genetically encoded fluorescent reporter reveals oscillatory phosphorylation by protein kinase C. *The Journal of Cell Biology*, 161(5):899–909, 2003.
- [137] Mathijs Vleugel, Tim A Hoek, Eelco Tromer, Tale Sliedrecht, Vincent Groenewold, Manja Omerzu, and Geert JPL Kops. Dissecting the roles of human BUB1 in the spindle assembly checkpoint. *Journal of Cell Science*, 128(16):2975–2982, 2015.
- [138] Xinru Wang, Rakhi Bajaj, Mathieu Bollen, Wolfgang Peti, and Rebecca Page. Expanding the PP2A interactome by defining a B56-specific SLIM. *Structure*, 24(12):2174–2181, 2016.
- [139] Jiao Wang, Zhizhi Wang, Tingting Yu, Huan Yang, David M Virshup, Geert JPL Kops, Sang Hyun Lee, Weihong Zhou, Xin Li, Wenqing Xu, and Zihe Rao. Crystal structure of a PP2A B56-BubR1 complex and its implications for PP2A substrate recruitment and localization. *Protein & Cell*, 7(7):516–526, 2016.
- [140] Kazuhiko SK Uchida, Kentaro Takagaki, Kazuki Kumada, Youko Hirayama, Tetsuo Noda, and Toru Hirota. Kinetochore stretching inactivates the spindle assembly checkpoint. *Journal of Cell Biology*, 184(3):383–390, 2009.
- [141] Sabine Elowe, Stefan Hümmel, Andreas Uldschmid, Xiuling Li, and Erich A Nigg. Tension-sensitive Plk1 phosphorylation on BubR1 regulates the stability of kinetochore-microtubule interactions. *Genes & Development*, 21(17):2205–2219, 2007.
- [142] Feng Li, Hyeung Kim, Zhejian Ji, Tianpeng Zhang, Bohong Chen, Yuanlong Ge, Yang Hu, Xuyang Feng, Xin Han, Huimin Xu, Youwei Zhang, Hongtao Yu, Dan Liu, Wenbin Ma, and Zhou Songyang. The BUB3-BUB1 complex promotes telomere DNA replication. *Molecular Cell*, 70(3):395–407, 2018.
- [143] Eunhee Choi, Xiangli Zhang, Chao Xing, and Hongtao Yu. Mitotic checkpoint regulators control insulin signaling and metabolic homeostasis. *Cell*, 166(3):567–581, 2016.
- [144] Eunhee Choi, Sotaro Kikuchi, Haishan Gao, Karolina Brodzik, Ibrahim Nassour, Adam Yopp, Amit G Singal, Hao Zhu, and Hongtao Yu. Mitotic regulators and the SHP2-MAPK pathway promote IR endocytosis and feedback regulation of insulin signaling. *Nature Communications*, 10(1):1–17, 2019.
- [145] Chunying Yang, Haibo Wang, Yiran Xu, Kathryn L Brinkman, Hiromichi Ishiyama, Stephen TC Wong, and Bo Xu. The kinetochore protein Bub1 participates in the DNA damage response. *DNA Repair*, 11(2):185–191, 2012.

- [146] Emily A Foley, Maria Maldonado, and Tarun M Kapoor. Formation of stable attachments between kinetochores and microtubules depends on the B56-PP2A phosphatase. *Nature Cell Biology*, 13(10):1265–1271, 2011.
- [147] Ajit Joglekar, Renjie Chen, and Joshua Lawrimore. A sensitized emission based calibration of FRET efficiency for probing the architecture of macromolecular machines. *Cellular and Molecular Bioengineering*, 6(4):369–382, 2013.
- [148] Hoi Tang Ma and Randy Yat Choi Poon. TRIP13 regulates both the activation and inactivation of the spindle-assembly checkpoint. *Cell Reports*, 14(5):1086–1099, 2016.
- [149] Hoi Tang Ma and Randy YC Poon. TRIP13 functions in the establishment of the spindle assembly checkpoint by replenishing O-MAD2. *Cell Reports*, 22(6):1439–1450, 2018.
- [150] Dong Hyun Kim, Joo Seok Han, Peter Ly, Qiaozhen Ye, Moira A McMahon, Kyungjae Myung, Kevin D Corbett, and Don W Cleveland. TRIP13 and APC15 drive mitotic exit by turnover of interphase-and unattached kinetochore-produced MCC. *Nature Communications*, 9(1):1–11, 2018.
- [151] Elyse S Fischer, Conny WH Yu, Johannes F Hevler, Stephen H McLaughlin, Sarah L Maslen, Albert JR Heck, Stefan MV Freund, and David Barford. Juxtaposition of Bub1 and Cdc20 on phosphorylated Mad1 during catalytic mitotic checkpoint complex assembly. *bioRxiv*, 2022.
- [152] Wei Tian, Bing Li, Ross Warrington, Diana R Tomchick, Hongtao Yu, and Xuelian Luo. Structural analysis of human Cdc20 supports multisite degron recognition by APC/C. *Proceedings of the National Academy of Sciences*, 109(45):18419–18424, 2012.
- [153] Mayuko Hara, Engin Özkan, Hongbin Sun, Hongtao Yu, and Xuelian Luo. Structure of an intermediate conformer of the spindle checkpoint protein Mad2. *Proceedings of the National Academy of Sciences*, 112(36):11252–11257, 2015.
- [154] Xuelian Luo, Zhanyun Tang, Guohong Xia, Katja Wassmann, Tomohiro Matsumoto, Josep Rizo, and Hongtao Yu. The Mad2 spindle checkpoint protein has two distinct natively folded states. *Nature Structural & Molecular Biology*, 11(4):338–345, 2004.
- [155] Anna De Antoni, Chad G Pearson, Daniela Cimini, Julie C Canman, Valeria Sala, Luigi Nezi, Marina Mapelli, Lucia Sironi, Mario Faretta, Edward D Salmon, and Andrea Musacchio. The Mad1/Mad2 complex as a template for Mad2 activation in the spindle assembly checkpoint. *Current Biology*, 15(3):214–225, 2005.
- [156] Soonjoung Kim, Hongbin Sun, Diana R Tomchick, Hongtao Yu, and Xuelian Luo. Structure of human Mad1 C-terminal domain reveals its involvement in kinetochore targeting. *Proceedings of the National Academy of Sciences*, 109(17):6549–6554, 2012.
- [157] Andrei Lupas, Marc Van Dyke, and Jeff Stock. Predicting coiled coils from protein sequences. *Science*, 252(5009):1162–1164, 1991.

- [158] Jan Ludwiczak, Aleksander Winski, Krzysztof Szczepaniak, Vikram Alva, and Stanisław Dunin-Horkawicz. DeepCoil-a fast and accurate prediction of coiled-coil domains in protein sequences. *Bioinformatics*, 35(16):2790–2795, 2019.
- [159] Mauro Delorenzi and Terry Speed. An HMM model for coiled-coil domains and a comparison with PSSM-based predictions. *Bioinformatics*, 18(4):617–625, 2002.
- [160] David T Jones. Protein secondary structure prediction based on position-specific scoring matrices. *Journal of Molecular Biology*, 292(2):195–202, 1999.
- [161] Daniel WA Buchan and David T Jones. The PSIPRED protein analysis workbench: 20 years on. *Nucleic Acids Research*, 47(W1):W402–W407, 2019.
- [162] Thomas Kruse, Marie Sofie Yoo Larsen, Garry G Sedgwick, Jón Otti Sigurdsson, Werner Streicher, Jesper V Olsen, and Jakob Nilsson. A direct role of Mad1 in the spindle assembly checkpoint beyond Mad2 kinetochore recruitment. *EMBO Reports*, 15(3):282–290, 2014.
- [163] Stephanie Heinrich, Katharina Sewart, Hanna Windecker, Maria Langegger, Nadine Schmidt, Nicole Hustedt, and Silke Hauf. Mad1 contribution to spindle assembly checkpoint signalling goes beyond presenting Mad2 at kinetochores. *EMBO Reports*, 15(3):291–298, 2014.
- [164] Lisa J Lapidus, Peter J Steinbach, William A Eaton, Attila Szabo, and James Hofrichter. Effects of chain stiffness on the dynamics of loop formation in polypeptides. Appendix: testing a 1-dimensional diffusion model for peptide dynamics. *The Journal of Physical Chemistry B*, 106(44):11628–11640, 2002.
- [165] Huan-Xiang Zhou. Polymer models of protein stability, folding, and interactions. *Biochemistry*, 43(8):2141–2154, 2004.
- [166] Barbara Di Fiore, Norman E Davey, Anja Hagting, Daisuke Izawa, Jörg Mansfeld, Toby J Gibson, and Jonathon Pines. The ABBA motif binds APC/C activators and is shared by APC/C substrates and regulators. *Developmental Cell*, 32(3):358–372, 2015.
- [167] Wenbin Ji, Yibo Luo, Ejaz Ahmad, and Song-Tao Liu. Direct interactions of mitotic arrest deficient 1 (MAD1) domains with each other and MAD2 conformers are required for mitotic checkpoint signaling. *Journal of Biological Chemistry*, 293(2):484–496, 2018.
- [168] Miltot Mirdita, Konstantin Schütze, Yoshitaka Moriwaki, Lim Heo, Sergey Ovchinnikov, and Martin Steinegger. ColabFold-Making protein folding accessible to all. *bioRxiv*, 2021.
- [169] Daphne S Bindels, Lindsay Haarbosch, Laura Van Weeren, Marten Postma, Katrin E Wiese, Marieke Mastop, Sylvain Aumonier, Guillaume Gotthard, Antoine Royant, Mark A Hink, and Theodorus W J Gadella Jr. mScarlet: a bright monomeric red fluorescent protein for cellular imaging. *Nature Methods*, 14(1):53, 2017.

- [170] Marina Mapelli, Lucia Massimiliano, Stefano Santaguida, and Andrea Musacchio. The Mad2 conformational dimer: structure and implications for the spindle assembly checkpoint. *Cell*, 131(4):730–743, 2007.
- [171] Wolfgang Becker. Fluorescence lifetime imaging-techniques and applications. *Journal of Microscopy*, 247(2):119–136, 2012.
- [172] Tatiana Alfonso-Pérez, Daniel Hayward, James Holder, Ulrike Gruneberg, and Francis A Barr. MAD1-dependent recruitment of CDK1-CCNB1 to kinetochores promotes spindle checkpoint signaling. *Journal of Cell Biology*, 218(4):1108–1117, 2019.
- [173] Clifford R Robinson and Robert T Sauer. Optimizing the stability of single-chain proteins by linker length and composition mutagenesis. *Proceedings of the National Academy of Sciences*, 95(11):5929–5934, 1998.
- [174] GN Ramachandran and Alok K Mitra. An explanation for the rare occurrence of *cis* peptide units in proteins and polypeptides. *Journal of Molecular Biology*, 107(1):85–92, 1976.
- [175] Maojun Yang, Bing Li, Chyong-Jy Liu, Diana R Tomchick, Mischa Machius, Josep Rizo, Hongtao Yu, and Xuelian Luo. Insights into Mad2 regulation in the spindle checkpoint revealed by the crystal structure of the symmetric Mad2 dimer. *PLoS Biology*, 6(3):e50, 2008.
- [176] Nina Schweizer, Cristina Ferrás, David M Kern, Elsa Logarinho, Iain M Cheeseman, and Helder Maiato. Spindle assembly checkpoint robustness requires Tpr-mediated regulation of Mad1/Mad2 proteostasis. *Journal of Cell Biology*, 203(6):883–893, 2013.
- [177] Qiangfeng Cliff Zhang, Donald Petrey, José Ignacio Garzón, Lei Deng, and Barry Honig. PrePPI: a structure-informed database of protein-protein interactions. *Nucleic Acids Research*, 41(D1):D828–D833, 2012.
- [178] Huaiyu Mi, Anushya Muruganujan, John T Casagrande, and Paul D Thomas. Large-scale gene function analysis with the PANTHER classification system. *Nature Protocols*, 8(8):1551–1566, 2013.
- [179] Marco Simonetta, Romilde Manzoni, Roberto Mosca, Marina Mapelli, Lucia Massimiliano, Martin Vink, Bela Novak, Andrea Musacchio, and Andrea Ciliberto. The influence of catalysis on Mad2 activation dynamics. *PLoS Biology*, 7(1):e1000010, 2009.
- [180] Robert L Grossman, Allison P Heath, Vincent Ferretti, Harold E Varmus, Douglas R Lowy, Warren A Kibbe, and Louis M Staudt. Toward a shared vision for cancer genomic data. *New England Journal of Medicine*, 375(12):1109–1112, 2016.
- [181] Michael Orth, Bernd Mayer, Kinga Rehm, Ulli Rothweiler, Doris Heidmann, Tad A Holak, and Olaf Stemmann. Shugoshin is a Mad1/Cdc20-like interactor of Mad2. *The EMBO Journal*, 30(14):2868–2880, 2011.

- [182] Yajie Gu, Arshad Desai, and Kevin D Corbett. Evolutionary dynamics and molecular mechanisms of HORMA domain protein signaling. *Annual Review of Biochemistry*, 91, 2021.
- [183] Sri Rama Koti Ainavarapu, Jasna Brujić, Hector H Huang, Arun P Wiita, Hui Lu, Lewyn Li, Kirstin A Walther, Mariano Carrion-Vazquez, Hongbin Li, and Julio M Fernandez. Contour length and refolding rate of a small protein controlled by engineered disulfide bonds. *Biophysical Journal*, 92(1):225–233, 2007.
- [184] Jia Li, Jian-Zhi Gao, Jing-Li Du, Zhong-Xi Huang, and Li-Xin Wei. Increased CDC20 expression is associated with development and progression of hepatocellular carcinoma. *International Journal of Oncology*, 45(4):1547–1555, 2014.
- [185] Mariusz Szabelski, Rafal Luchowski, Zygmunt Gryczynski, Peter Kapusta, Uwe Ortmann, and Ignacy Gryczynski. Evaluation of instrument response functions for lifetime imaging detectors using quenched Rose Bengal solutions. *Chemical Physics Letters*, 471(1-3):153–159, 2009.
- [186] Bhim Prasad Kafle. *Chemical Analysis and Material Characterization by Spectrophotometry*. Elsevier, 2020.
- [187] Kevin C Wang and Howard Y Chang. Molecular mechanisms of long noncoding RNAs. *Molecular Cell*, 43(6):904–914, 2011.
- [188] Albert Goldbeter and Daniel E Koshland. An amplified sensitivity arising from covalent modification in biological systems. *Proceedings of the National Academy of Sciences*, 78(11):6840–6844, 1981.